Study on Cobalt-Chromium-based Alloys for Ultra-High-Temperature
Applications
Optimising Composition for Improved Oxidation Resistance and
Mechanical Properties

超高温で用いられる Co-Cr 基合金に関する研究
耐酸化特性と機械的特性向上の為の組成最適化

February, 2024

Louis Etienne Victor MOREAU
モロー　ルイ・エティエンヌ・ヴィクトル

Study on Cobalt-Chromium-based Alloys for Ultra-High-Temperature
Applications
Optimising Composition for Improved Oxidation Resistance and
Mechanical Properties

超高温で用いられる Co-Cr 基合金に関する研究
耐酸化特性と機械的特性向上の為の組成最適化

February, 2024

Waseda University Graduate School of Advanced Science and
Engineering

Department of Nanoscience and Nanoengineering, Research on Physical
Chemistry of Surfaces and Interfaces

Louis Etienne Victor MOREAU
モロー　ルイ・エティエンヌ・ヴィクトル

TABLE OF CONTENTS

Introduction

The development of glass fibers, closely aligned with the progress of industrialization, has been a significant technological advancement since the early 20th century [1]. These fibers, known for their strength, flexibility, heat, and chemical resistance [2-11], have become indispensable in various industries, including insulation, aerospace, telecommunications, and automotive [6,12-18]. Saint-Gobain, a pioneer in glass manufacturing, has played a pivotal role in this evolution. Their continuous improvements in manufacturing processes [19, 20], development of new glass compositions [21], and advancements in fiber spinning processes [22], particularly in creating finer and more uniform fibers [23, 24], have significantly influenced the glass fiber industry. Their international expansion and commitment to sustainable production have further solidified their leadership position in the sector [25].

In the glass industry, deploying materials capable of withstanding temperatures frequently exceeding 1300°C is crucial [26], particularly for components such as spinners, stirrers, or fusion electrodes. These elevated thermal conditions present formidable challenges, not only in terms of resistance to molten glass corrosion [27, 28] but also against hot temperature oxidation [29-31] and in maintaining robust mechanical properties under such demanding operational conditions. Ceramic materials, though resistant to glass corrosion and oxidation at temperatures above 1200 °C, are generally ruled out due to their inadequate mechanical performance at high temperatures, especially for rotating parts [1, 32]. Super alloys based on nickel or cobalt, once favored for their excellent high-temperature properties [33-37], are no longer viable at these extreme temperatures due to their proximity to their limitation temperatures [2, 3]. The complexity of this challenge is particularly pronounced for spinner discs, essential components in glass fiber production. Subjected to an extremely harsh environment, these discs must withstand both molten glass and thermal degradation from the

heat of gas burners. The mechanical strain is compounded by rapid rotation, necessitating exceptional creep resistance [38].

In this thesis, we explore the development of new Co-Cr based alloys designed for ultra-high-temperature applications, with a particular focus on improving oxidation resistance and mechanical properties, essential for the demanding application of glass spinner discs. This research begins with the study of the Co-Cr-Ta alloy system, drawing inspiration from the remarkable resilience of Co-based superalloys in aviation and aerospace sectors [39-41] and by already existing alloy with outstanding properties in glass industry's processes [42], such as the TaTiC4 alloy developed by Michon et al. [43] The aim of this work is to bridge the gap between the current limitations of Co-Cr alloys and the requirements of high-temperature environments, such as those encountered in glass manufacturing. Through a comprehensive approach involving experimental analysis, predictive modeling, and innovative material design, this research aims not only to address the specific needs of the glass industry but also to contribute broadly to the field of high-temperature material science.

This thesis consists of 6 chapters:

Chapter 1 serves as an introduction and sets the background for this research. It delves into a comprehensive exploration of TaTiC4's composition and offers a detailed understanding of the glass fiber manufacturing process. The challenges associated with glass spinners are thoroughly discussed to provide insight into the need for alloy improvement. The chapter also examines various oxide layers and explores approaches for utilizing and enhancing the Cr_2O_3 layer. This chapter succinctly outlines the current material and its limitations, emphasizing the need for alloy enhancement. It introduces avenues for research, focusing on specific oxide layer utilization and improvement.

In a second time, this chapter outlines the methodology for alloy formation, characterization, and testing, detailing the machinery used. Additionally, it highlights the application of predictive tools like CALPHAD and machine learning, emphasizing their significance in enhancing research precision and efficiency.

Chapter 2 is dedicated to investigating the formation and microstructural evolution of Co-Cr-Ta ternary alloys as a function of their composition and how this influences oxidation resistance at 1200 °C. Initial results serve as a foundational database for the development of the optimal Co-Cr-Ta composition, capable of withstanding 20 hours of oxidation in air at 1200 °C. Advanced machine learning methods are employed in this pursuit. This chapter delves into the formation and microstructural changes in Co-Cr-Ta alloys concerning their composition and their influence on oxidation resistance at 1200°C. These initial findings lay the foundation for creating an optimal alloy that can withstand 20 hours of oxidation at this temperature, aided by advanced machine learning techniques.

In Chapter 3, the focus is on the critical role of forming the complex oxide $CrTaO_4$ to enhance oxidation resistance. The chapter explores the composition field to form $CrTaO_4$. The formation of $CrTaO_4$ at temperatures ranging from 900 °C to 1200 °C for various durations is thoroughly examined. Additionally, cyclic oxidation tests at 1200 °C, oxidation tests at 1300 °C, and corrosion testing in glass environments are conducted to confirm the significant performance improvement of Co-Cr-Ta alloys resulting from $CrTaO_4$ formation. In summary, the vital aspect of $CrTaO_4$ formation for enhancing Co-Cr-Ta alloys' oxidation resistance was highlighted.

Chapter 4 provides a detailed examination of the impact of the Cr/Ta atomic ratio on the formation of $CrTaO_4$. The study extends to a theoretical and thermodynamic analysis of the $CrTaO_4$ oxide layer formation. Subsequently, the chapter outlines the initial efforts to optimise the composition of the Co-Cr-Ta ternary alloy system. This optimisation successfully yielded a

Co-Cr-Ta sample with only two phases in its microstructure, forming a stable and continuous $CrTaO_4$ protective oxide layer at 1200 °C for 20 h in an air environment.

Chapter 5 provides insights into the mechanical behavior of Co-Cr-Ta alloys under high-temperature conditions. While Vickers hardness tests at elevated temperatures yielded results consistent with the base material, tensile tests conducted at 900 °C and 1200 °C unveiled shortcomings in the mechanical properties of these alloys, particularly at high temperatures. These findings underscore the challenges that need to be addressed in optimizing the alloy's performance in such demanding environments. In this chapter also, the addition of carbon into the ternary alloys responsible for $CrTaO_4$ formation is investigated as a response to the previously identified challenges. With a coherent heat treatment, presence of carbides in the alloys were observed. Subsequent mechanical tests have been conducted to assess the consequential impact on mechanical properties, revealing notable improvements in contrast to the alloy formulations outlined in Chapter 3. Moreover, to affirm the sustained high-temperature oxidation resistance of the alloys, a new series of oxidation tests at 1200 °C has been undertaken. In summary, the addition of carbon to ternary alloys, forming $CrTaO_4$, enhances mechanical properties. New oxidation tests confirm sustained high-temperature resistance.

In Chapter 6, the author delves into strategies aimed at augmenting the mechanical characteristics of Co-Cr-Ta samples. One approach involves the addition of rhenium (Re) in concentrations spanning from 0 to 15 at.%. Re, which is recognized for its elevated melting point and thereby advantageous mechanical properties at high temperatures. The findings reveal the inherent challenges in achieving substantial enhancements regarding the mechanical attributes of Co-based samples. Additionally, a significant decline in oxidation resistance is observed, which is attributed to the formation of volatile Re oxides. This chapter also initiates the pursuit of developing high entropy alloys to further elevate the potential of Co-Cr-Ta alloys for ultra-high-temperature applications. Although the inclusion of Re exhibits potential for

elevated-temperature applications, it comes at the cost of reduced oxidation resistance due to volatile Re oxide formation. The author also introduces alternative approaches, including the development of high entropy alloys as a novel alloy type, with the goal of surpassing existing Co-based alloys.

Finally, a conclusion synthesizes the results of this thesis research, highlighting the significant positive impact of $CrTaO_4$ formation on oxidation resistance at 1200°C. Additionally, it discusses optimizing the composition of Co-Cr-Ta to guarantee the formation of this protective oxide layer. This conclusion also covers the role of carbon addition in enhancing mechanical properties at high temperatures.

This thesis aims to bridge the gap in knowledge and application between the current limitations of Co-Cr-Ta alloys and the requirements of high-temperature environments such as those in glass manufacturing. Through a comprehensive approach involving experimental analysis, predictive modeling, and innovative material design, this research aims to not only address the specific needs of the glass industry but also to contribute broadly to the field of high-temperature material science.

This study embarks on a vital exploration of Cobalt-Chromium-based alloys, targeting the improvement of their oxidation resistance and mechanical properties for ultra-high-temperature applications. The findings and developments from this research have the potential to significantly advance the performance and longevity of materials in demanding industrial applications.

Chapter 1: Background and methods

1.1. Glass fiber processing

The evolution of glass fibers, intrinsically linked to the advancements in industrialization, represents a significant technological leap since the early 20th century. These fibers, characterized by their exceptional strength [44,45], flexibility, and resistance to heat [46, 47] and chemicals, have carved out a vital role across various sectors including insulation, aerospace, telecommunications, and automotive. The pioneering efforts of Saint-Gobain in glass manufacturing have been instrumental in this journey [48]. Through the refinement of manufacturing processes, the development of new glass compositions, and the innovation in fiber spinning technologies, they have played a pivotal role in shaping the modern glass fiber industry.

1.1.1. History of the development of glass fibers by Saint-Gobain

The issue of cold has always been central to human survival. Protecting oneself from the cold through various means, such as clothing and shelters, has been a principal solution experimented by the human species [49]. When it came to building, the thickness of construction materials was initially thought to be the most effective solution, until the insulating power of hollow materials, like bricks, was discovered, leading to the creation of dedicated insulating materials [50]. Insulating fibers, including glass wool, fall into this category.

Specifically, glass wool consists of a disordered entanglement of very fine glass fibers forming a felt/mattress, trapping air (which represents more than 95% of the product's volume). Because of this structure, glass wool becomes an excellent thermal insulator. It is also rot-proof and non-combustible. Additionally, it is a material that is not attacked by rodents and is relatively stable over time [51-53].

6

In France, the post-war period marked the beginning of a favorable era for insulation materials. The country was devastated. Factories and destroyed buildings needed to be rebuilt. These two domains provided significant outlets for a good quality thermal insulator. This growth continued to achieve a 30% increase per year in the 1950s [25]. The company Saint-Gobain recorded a record profit in 1951 of 1385 million compared to 585 million francs in 1950. The development of construction stimulated activity; fiberglass sales increased by 50%. Demand exploded: "Rural exodus, urbanization, and economic growth combined to cause a boom in housing construction," as read in Saint-Gobain and Glass Wool regarding the history of glass wool [32, 51]. This boom was also due to the "development of the idea of insulation", reflected in the standards of "housing construction" and responding to a "concern for calorie economy". This calorie economy resulted from a "constant increase in the price of fluids" in a context where the quality of the feel of glass wool had greatly improved. The 1950s in France marked a transformative era for the fiberglass industry, largely influenced by the post-war reconstruction needs and evolving consumer behaviors. The industry's growth was significantly propelled by effective marketing strategies, notably the "campaign of silence," which focused on promoting fiberglass for its acoustic insulation properties. This campaign, alongside others, played a pivotal role in shifting public perception of fiberglass from a mere construction material to a necessary component for modern living, emphasizing its thermal and sound insulation capabilities. A crucial aspect of this era was the industry's response to the needs and concerns of users. The development of the TEL process is a prime example, showcasing the industry's commitment to improving product quality and user experience. This process not only made fiberglass more user-friendly by eliminating the discomfort of prickliness but also signified a shift in the industry's approach towards product development - prioritizing ergonomic design and user safety [54]. The introduction of bakelite in the production process,

despite initial setbacks in altering the texture of the product, reflected the industry's ongoing efforts to enhance the usability of fiberglass.

The adoption of fiberglass in various industries, including the booming household appliance sector, is also noteworthy. Companies like Frigidaire, responding to the increased demand for refrigerators, turned to fiberglass for insulation, indicating the material's versatility and effectiveness. This trend was a testament to the changing lifestyle and consumption patterns of French households, where the possession of such appliances became increasingly common.

Moreover, the fiberglass industry's growth was closely linked to the broader economic and societal shifts of the time. The post-war reconstruction phase required efficient and effective insulation materials for rebuilding factories and housing, which fiberglass provided. Additionally, the industry's marketing strategies capitalized on the growing awareness of energy efficiency and cost savings, appealing to the contemporary consumer's desire for economical and practical solutions.

1.1.2. Development of the TEL process for industrialization of glass fibers

The development of the TEL (Tournette-Étirage de la Laine) process in fiberglass production is an epic journey marked by three distinct phases, each characterized by a major conceptual evolution [54].

- **1941-1945: The LET Era** – This period saw the birth of the LET (name of the glass fiber process invented in 1941 by the Laboratoire d'Essais Thermiques) process, a creative synthesis of German centrifugation (Gossler and Hager methods) and American blowing techniques (Owens process). Ivan Peyches, driving this innovation, preferred the centrifugation approach for its compatibility with recycled glass, crucial during resource-scarce times. The LET process featured a "tournette" (a high-speed, heat-

resistant rotating plate) instead of a quickly wearing grooved refractory disk. This tournette was a novel addition, made of Nicral (Nickel/Chrome/Aluminum), requiring the use of soft glass to preserve the plate's integrity. The tournette's design, which included a saucer-like shape with holes for injecting soft glass beads, was a result of Peyches' aerodynamic studies aimed at optimizing the centrifugation of glass.

- **1945-1952: The Transition to TEL** – Post-World War II, the LET evolved into TEL (Tournette-Étirage de la Laine) with a major redesign. The TEL process involved glass being fed from above, simplifying the collection process. This phase saw significant work on glass composition, burner design, and the tournette itself, with exhaustive experimental research on its shape, material, and hole distribution.

- **1952-1957: The Supertel Phase** – The name "Supertel" was coined in 1952, marking the start of intense research efforts under Marcel Lévecque's supervision to apply Pierre Heymes' fibrage principle to the TEL machine. Supertel was an enhancement of the rotary process, inspired by Heymes' analogy drawn from V1 and V2 missile technology. The team addressed various challenges such as ensuring uniform fiber diameter and improving the fiber spinning process.

Throughout these phases, the TEL process underwent continuous reconception. In addition, there were numerous challenges, such as maintaining the tournette's structural integrity at high temperatures and ensuring efficient fiber drawing. Ivan Peyches' and his team's commitment to understanding the underlying physics and mechanics of fiber production was crucial, leading to over 700 patents.

1.1.3. Challenges of the TEL processes for the materials

Here we describe the TEL process for the fabrication of molten glass. First this process has to stay at temperatures around 1200 °C to allow the glass to stay in its liquid phase and

ensure the melting of all its components. Then, the molten glass is fed onto a rapidly rotating plate called "spinner" as visible in Fig. 1.1.
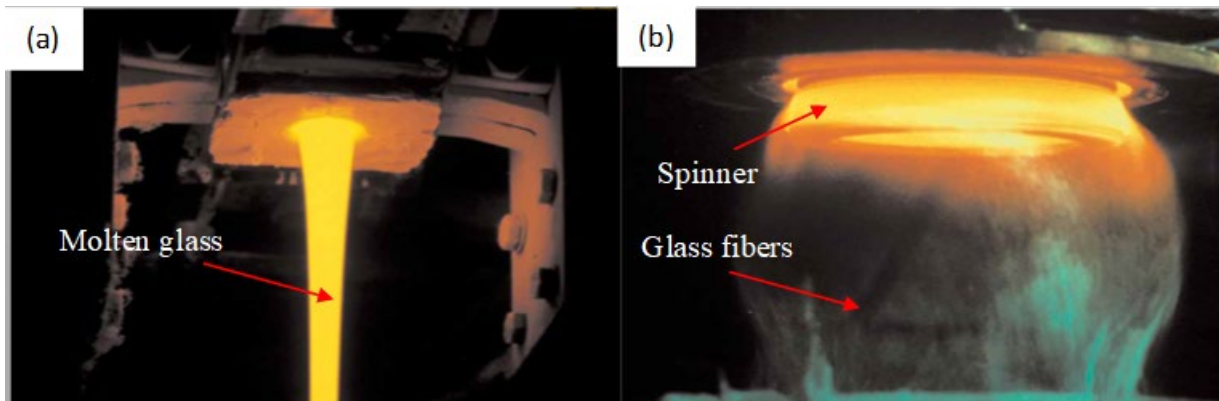
Figure 1.1. (a) Molten glass and (b) spinner in use [48].
Figure 1.1 is adapted from the figure in SAINT-GOBAIN
et la laine de verre : Histoire d'une réussite internationale.
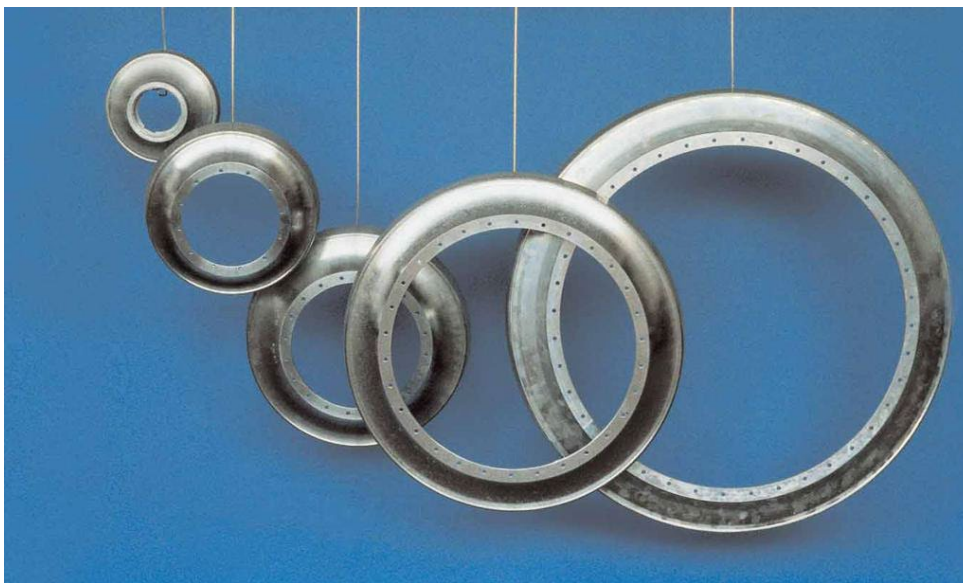
Figure 1.2. Glass fiber spinners of various dimensions [48].
Figure 1.2 is adapted from the figure in SAINT-GOBAIN et la
laine de verre : Histoire d'une réussite internationale.

The spinner is a cylindric metallic piece made of refractory alloy to ensure good properties throughout the process. The side surface of the cylinder is covered of holes of a diameter corresponding to the size of the fibers targeted. Spinners of various dimensions are visible in Fig. 1.2. With the super high speed of rotation of the spinner, the molten glass is projected on the sides of the spinners by centrifugal effect. The molten glass cross through the
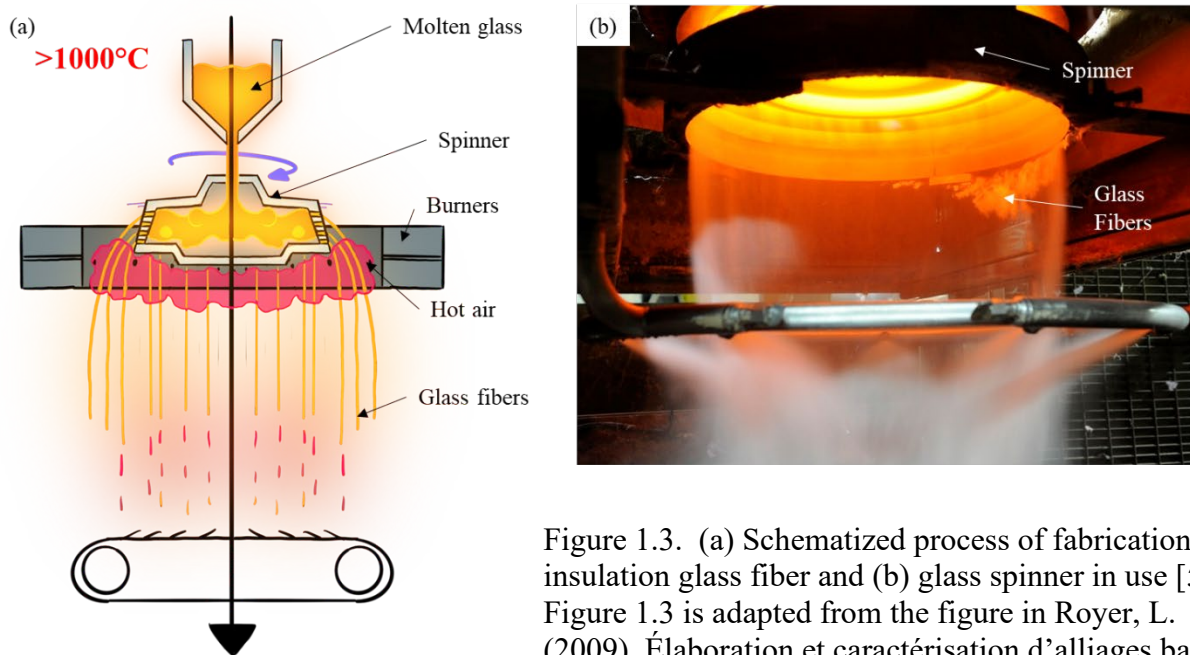
Figure 1.3. (a) Schematized process of fabrication of insulation glass fiber and (b) glass spinner in use [55]. Figure 1.3 is adapted from the figure in Royer, L. (2009). Élaboration et caractérisation d'alliages base chrome pour applications à très haute température. Université Henri Poincaré, Nancy I.

holes to form the glass fibers. On the outside of the spinner, burners are situated to stop the splashing of the newly formed fibers but also ensure its elongation as schematized in Fig. 1.3(a).

The spinners play a central role in this process and its durability of these spinners is severely tested. Under the effect of intense heat and rapid rotation, deformations appear, the diameters of the holes widen, and finally cracks form, thus compromising the efficiency and lifespan of these essential components.

1.1.4. Limits and improvement of the TEL process

With the burners and the blowing crown, the spinner is the most important part of the TEL process. It largely determines the process's capacity and the quality of the fiber. Therefore, the spinner benefits from the majority of the development effort.

During the fabrication process of glass fibers, several critical factors need to be considered, particularly concerning the glass spinner. Firstly, achieving sufficient centrifugal force to expel the molten glass from the spinner's interior through its holes requires an extremely

high-speed rotation of the plate (>1200 rounds per minute). Moreover, the diameter of the spinner, which varies depending on the fiber's intended application and typically ranges between 200 and 800 nm, holds significant importance. Larger spinner diameters result in increased internal stresses, which can reach up to 50 MPa due to the high material density and size, leading to creep deformation.

Secondly, the operating temperatures exceed 1050 °C and can reach as high as 1200 °C to meet CO_2 emission reduction and efficiency objectives as well as keeping the glass in its molten state. These elevated temperatures present a major challenge for the chosen alloy since they are very close to the melting point of current superalloys. Furthermore, as an industrial process, glass fiber manufacturing can lead to sudden thermal fluctuations. For instance, a shortage of glass supply can occur, as the molten glass serves as the primary source of heat required to maintain the plate's temperature. Additionally, an emergency stop may result in a rapid return to ambient temperature.

Thirdly, the glass composition, depending on its application, along with the molten glass itself in contact with the spinner, can cause severe corrosion of the metal. Moreover, the hot gases used to stretch the fibers have the potential to oxidize the plate.

All these conditions will damage the spinners, as shown in Fig. 1.4(a). The pink contours show the resulting profile after deformation. The diameter of the holes will increase with continued use and increasing up to +0.5mm in diameter. Some holes can then end up joining and causing cracks as shown in Fig. 1.4(b). Also, the temperature difference between the top and the bottom of the plate causes a curvature as seen in Fig. 1.4(a). After a short time of use, the spinners must be replaced to maintain a quality of the fibers produced corresponding to the specifications.

Given these challenges, it becomes crucial to improve the materials used in the construction of the spinners or even consider replacing them with novel alloy systems. Such

advancements are necessary to ensure the efficiency and reliability of the glass fiber manufacturing process [56].

Cobalt-based superalloys have played a critical role in advancing various high-temperature applications, especially in industries where performance under extreme conditions
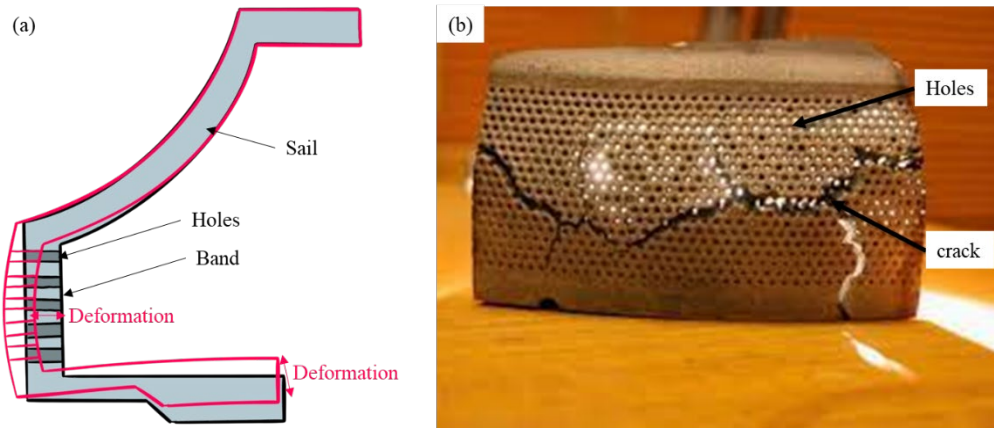
Figure 1.4. (a) Cut view of a spinner before (black) and after (pink) use and (b) cracks in a glass spinner after use.

is non-negotiable [57]. This chapter delves into the history, applications, and specific use of these alloys in the glass industry, with a focus on the TATIC4 alloy developed by Michon et al.

1.2. Materials

1.2.1. Development of alloys for spinners application

The spinner tool, essential for fiberizing glass, endures extreme conditions: thermal stress from temperature fluctuations and gradients, mechanical forces like centrifugal pressure and erosion, and chemical challenges from oxidation and corrosion. It's crucial to select materials for the spinner that can withstand these conditions over a significant production period while maintaining cost-effectiveness.

Advanced materials like nickel-based or cobalt-based superalloys, reinforced with carbide precipitations, are typically used [37-41]. These alloys are chosen for their unique combination of ductility, creep resistance, and resistance to oxidation and corrosion. For

instance, a cobalt-based alloy revealed in WO-A-99/16919 demonstrates improved high-temperature mechanical properties and oxidation resistance, essential for handling molten glass at temperatures around 1080 °C.

Other developments include alloys capable of enduring even higher temperatures, around 1100 °C and above [37], offering a balance between mechanical strength and oxidation resistance. These alloys, enriched with tantalum carbide precipitates, excel in high-temperature applications and resist oxidation effectively.

Recent advancements, like those described in WO 2005/052208 [58], showcase alloys with enhanced high-temperature strength and longevity in oxidizing environments. These are stabilized by nickel, contain chromium, and are fortified by titanium and tantalum carbides. These innovations are especially useful in industrial settings for processing new glass types, like basaltic compositions, which have higher melting points than traditional glass used in glass wool production.However, for the economic viability of producing basaltic glass fibers, the spinner's material must be robust enough to withstand high fiberizing temperatures. The goal is to create alloys with even greater high-temperature mechanical strength, enabling them to function at temperatures up to 1200 °C or higher, thus extending their lifespan under fiberizing conditions.

Innovations have led to cobalt-based alloys also comprising chromium and carbon, with a significantly lower nickel content than previous alloys, yet demonstrating superior performance. These alloys, with their unique microstructures and carbide precipitations, offer improved spinner lifetimes at high temperatures.

The ideal alloy composition balances various elements - chromium for strength and corrosion resistance, minimal nickel, and titanium and tantalum for carbide formation. This delicate mix ensures the alloy's durability, machinability, and cost-effectiveness.

Overall, these advancements in alloy composition and manufacturing processes represent significant strides in the industrial production of glass fibers, particularly for high-temperature applications. The development of these innovative materials not only enhances the performance and lifespan of the fiberizing tools but also contributes to the economic feasibility of producing advanced glass fiber materials.

1.2.2. Presentation of the reference material: TATIC4

This section describes the composition and properties of the alloy currently utilized as materials for spinners. Since October 2003, the production of Ultimate products commenced at the Isover factory in Lübz, Germany, reaching over 10,000 tons in 2006. This achievement was made possible through the successive use of BCo84 alloys and subsequently, alloys developed by Michon named TaTiC4 [43]. Behind this nomenclature lies a cobalt-based superalloy reinforced with intergranular and intragranular tantalum-titanium mixed carbides, the latter being achieved through heat treatment [36].

Furthermore, the composition of this alloy has a high chromium content, contributing to the intrinsic mechanical strength of the matrix. Chromium is partly in solid solution and, in certain cases, in the form of carbides, primarily $Cr_{23}C_6$ in fine dispersion within the grains, enhancing the material against intragranular creep. Chromium can also exist in the form of carbides such as Cr_7C_3 or $Cr_{23}C_6$ at grain boundaries, preventing grain-to-grain slip and contributing to the intergranular strengthening of the alloy. Additionally, chromium enhances corrosion resistance by forming a protective layer of chromium oxide on the surface exposed to an oxidizing environment, requiring a minimum amount for the formation and maintenance of this protective layer [59-65].

The alloy TaTiC4 enables the fiberization of glass or a similar fused mineral composition with a liquidus temperature (Tliq) of around 1130 °C or higher, notably between

15

1130 and 1200 °C, and specifically 1170 °C or higher. Generally, the fiberization of these fused

mineral compositions can be carried out within a temperature range between Tliq and Tlog2.5,

where Tlog2.5 is the temperature at which the fused composition exhibits a viscosity of 102.5

poise (dPa.s), typically around 1200 °C or higher, for instance, from 1240 to 1250 °C or higher.

The alloys must have a higher melting temperature
than the application temperatures. For instance, the
melting temperature of TaTiC4, measured by DTA,
is around 1330 °C, slightly exceeding the intended
applications but remaining close to the maximum
limit of the glass fiberization temperature range
mentioned above.
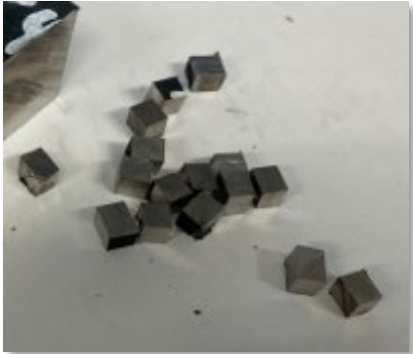
Figure 1.5. TaTiC4 used for comparison with the future developed alloys.

Although this alloy exhibits superior high-temperature properties compared to other

current cobalt-based alloy used for fiberization at 1050 °C, the average lifespan of a plate

remains relatively limited, around several hundred operating hours. Therefore, to develop alloys

surpassing the capabilities of TaTiC4 alloys, Saint-Gobain outlined an initial set of desired

conditions ahead of this research, presented in Table 1.1.

Table 1.1. Requirement for the development of new alloys for glass fibers spinners.

		Mechanical			Corrosion	
	Operating T	Creep rate	Creep failure	Kp oxidation g2.cm-4.s-1	Corrosion in THA or E Glass	
unit	oC	µm/h in 3pt FLX	h in 3pt FLX	1	Ohm.cm2	Additional target criteria
criterion	=	<	>	<	>	
THA	1200 (TBC)	10um/h @31MPa	-	200E-12	50	passive after oxidation at T in THA?
E GLASS	1300 max 1250 nominal	-	100h @7MPa	800E-12	300	Electrical conductivity for Joule Heating (vs design consideration)

To gain insights into the desired properties for future developed alloys, the same tests

will be conducted on the TaTiC4 alloy to compare values regarding oxidation in air, corrosion

in molten glass, and tensile strength at high temperatures. A block of TaTiC4 treated by Saint-

Gobain in their laboratory has been manufactured and sent to NIMS in Tsukuba for the purposes of this research.

1.2.3. Strategy to develop enhanced materials for spinner application

To advance the development of alloys surpassing the capabilities of TaTiC4, the strategy employed in this study is as follows. Rather than commencing with the pre-existing superalloy and streamlining the alloy composition optimisation process, a gradual approach will be adopted. This entails the systematic exploration of ternary alloys prior to the introduction of supplementary elements. This methodical approach aims to mitigate the inherent complexity associated with seeking optimal compositions, strategically limiting the number of phases within an alloy already comprised of numerous elements, each serving a specific purpose in influencing overall properties. The deliberate selection of ternary alloys will facilitate an in-depth study of the mechanical, thermal, and chemical properties of each element combination, thereby establishing a robust foundation for more comprehensive analyses. Advanced analytical techniques, such as scanning electron microscopy (SEM) and X-ray diffraction (XRD), will be employed to characterize the microstructure and determine the phases present in each ternary alloy.

Once optimal ternary compositions are established, the strategy will progress towards the sequential introduction of additional elements, allowing for a controlled expansion of alloy complexity. This iterative process of composition optimisation at each stage will ensure a thorough understanding of the interactions between elements, thereby facilitating the development of alloys surpassing the performance of TaTiC4.

To implement this gradual approach, commencing with the design of ternary alloys, we draw inspiration from TaTiC4. Cobalt has been chosen as the foundational element, with a

substantial chromium content prioritized to confer excellent mechanical properties and remarkable resistance to corrosion and high-temperature oxidation. Complementing this composition, the deliberate choice of a third refractory element, such as tantalum (Ta) or titanium (Ti) for example, is motivated by the necessity to guarantee optimal performance at elevated temperatures.

To guide the selection and optimisation of compositions, predictive methods, particularly the CALPHAD model, will be employed. CALPHAD will enable precise modeling of phase diagrams, providing a comprehensive understanding of alloy behavior under varied thermal conditions [66-70]. This predictive approach will facilitate the exploration of numerous potential compositions, judiciously balancing mechanical, thermal, and chemical properties. An example of CALPHAD prediction is presented in Fig. 1.6 :

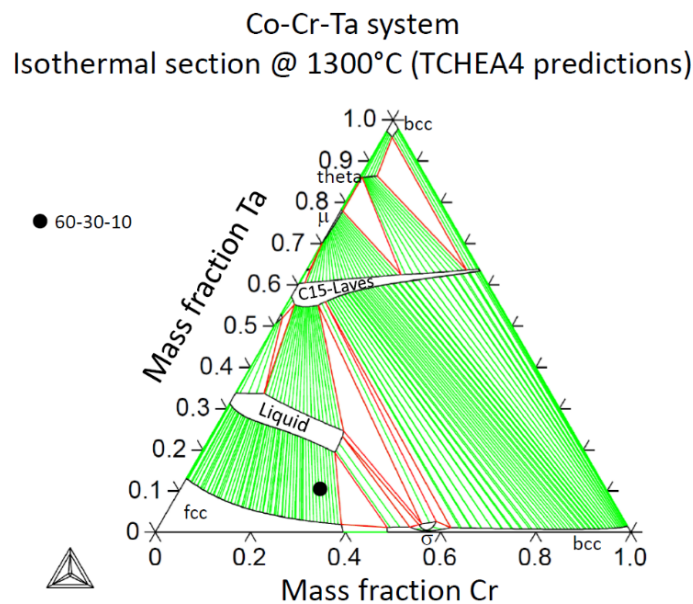Figure 1.6. Example of prediction of CoCrTa phase composition at 1300 °C.

CALPHAD, based on the Calculation of Phase Diagrams, stands as an indispensable tool in metallurgy and alloy design. Grounded in the thermodynamics of phases, it aims to calculate phase diagrams, offering crucial insights into the phases present in alloys at different temperatures. CALPHAD leverages experimental thermodynamic data to construct

mathematical models describing the free energy of constituent phases in a multi-component system. By applying these models, CALPHAD can predict phase equilibria, phase transitions, and thermodynamic conditions at different temperatures and compositions. This systematic approach enables a virtual and comprehensive exploration of possible element combinations in an alloy, facilitating the search for optimal compositions. In the specific context of the ternary alloys envisaged to surpass TaTiC4, the utilization of CALPHAD provides the opportunity to predict stable and metastable phases at different temperatures. This encompasses determining phase coexistence zones and equilibria between phases, critical elements for comprehending alloy behavior in varied thermal conditions. By integrating these predictions with experimental results, we can refine and optimise alloy compositions systematically, ensuring a scientific and systematic approach in the development of advanced materials for glass fiber reinforcement and molten mineral compositions. The iteration between CALPHAD predictions and experimental results constitutes a crucial step in the optimisation process. Considering kinetic parameters of phase reactions, this strategy aims to continuously refine compositions to achieve an optimal balance [69, 70]. Collaborations with industrial partners and metallurgy experts will enhance the effectiveness of this approach, paving the way for innovative alloys surpassing the performance of TaTiC4 and opening new avenues in the field of glass fiber reinforcement and molten mineral compositions.

Following a series of comprehensive tests on the chosen alloy family, an innovative approach involving the application of machine learning methods, specifically Bayesian optimisation, is considered to optimise the composition of a new alloy while targeting specific properties [71-73]. This promising methodology seeks to automate and expedite the optimisation process, leveraging information generated by CALPHAD to predict the phases present in the newly envisioned compositions. Bayesian optimisation stands out for its efficiency in exploring parameter space, considering results from previous iterations to guide

the search towards promising regions. By incorporating defined metrics for targeted mechanical, thermal, or chemical properties, this approach will determine the optimal composition of the alloy. Once the optimised composition is identified through Bayesian optimisation, CALPHAD will be employed to predict the phases that will be present in this newly predicted composition. This synergistic combination of machine learning methods and thermodynamic modeling will provide an in-depth understanding of the properties of the newly designed alloy, enabling more targeted experimental validation by identifying conditions conducive to achieving the desired performances.

The judicious use of Bayesian optimisation and CALPHAD in this final phase of the alloy development process represents an innovative approach, combining the predictive power of machine learning with the precision of thermodynamic modeling. This convergence opens new perspectives for the creation of advanced and tailored materials.

1.2.4. The choice of a ternary alloy system

In the preceding paragraph, the objective is set to develop a cobalt-based ternary alloy with a high chromium content and a third refractory element. Initially, empirical choices were made regarding composition ratios before comparing different alloy families. Considering Co as the alloy base, the initial decision was to have a ratio of over 50% by weight of the total alloy. Additionally, based on the patent for glass fiber drawing plates filed by Saint-Gobain, a maximum of 30% by total weight was established for chromium content. Finally, a choice of a maximum of 10% by total weight of the alloy for the refractory element was set.

This preliminary study led to the establishment of a preliminary list of candidates, including:

Molybdenum: Recognized for its advantageous properties at high temperatures, it provides increased resistance to corrosion, especially in severe conditions [74-76]. Its ability

to form protective oxides and corrosion-resistant compounds contributes to preserving the structural integrity of alloys exposed to hostile environments. The structural stability of molybdenum at high temperatures makes it an optimal choice for applications requiring mechanical resistance at extreme temperatures, such as those reaching 1200 °C. The incorporation of molybdenum can significantly improve the mechanical properties of the alloy, including tensile strength, hardness, and high-temperature creep resistance. These improvements are crucial for ensuring structural integrity and mechanical performance in demanding environments. Furthermore, molybdenum can be synergistically combined with other alloying elements, such as chrome and nickel, to form alloys resistant to corrosion and high temperatures, opening up prospects for specific applications.

Tantalum: Maintaining its structural stability at high temperatures, it proves to be a suitable choice for applications requiring mechanical resistance at extreme temperatures, such as 1200 °C. Its exceptional resistance to oxidation and deformation at high temperatures provides significant advantages. Additionally, its corrosion resistance, even in aggressive environments, is notable. The formation of protective oxides on the surface helps prevent corrosion and maintain structural integrity under corrosive conditions at high temperatures [77-79]. As a refractory element, tantalum has the ability to form carbides and nitrides at high temperatures, reinforcing the alloy's metal matrix. These compounds significantly enhance the mechanical properties of the alloy, including tensile strength and creep resistance. The addition of tantalum can also improve tensile strength, hardness, and creep resistance of the alloy at high temperatures. These improvements are crucial for applications requiring robust mechanical properties in severe thermal conditions. Tantalum can be judiciously combined with other alloying elements, such as chrome, nickel, and molybdenum, to form alloys resistant to corrosion and high temperatures, allowing synergy between these elements for optimal properties. Furthermore, tantalum contributes to reducing grain migration at high temperatures,

providing crucial microstructural stability to maintain the alloy's structural integrity in extreme thermal conditions. Additionally, tantalum is used in TaTiC4 developed by Saint-Gobain for carbide formation.

Tungsten: Maintaining its structural stability at extremely high temperatures, tungsten is a suitable choice for applications requiring mechanical resistance in rigorous thermal conditions, notably at 1200 °C [76, 80-81]. Its ability to form carbides at high temperatures contributes to strengthening the alloy's metal matrix, improving tensile strength, hardness, and creep resistance at elevated temperatures. Besides its exceptional resistance to oxidation at high temperatures, tungsten forms a protective layer on the alloy's surface, preventing corrosion and degradation resulting from exposure to oxidizing atmospheres. Tungsten can be associated with other alloying elements, such as chrome and nickel, to form alloys resistant to corrosion and high temperatures, benefiting from synergy between these elements to achieve optimal mechanical properties and corrosion resistance. Moreover, the addition of tungsten contributes to reducing grain growth at high temperatures, enhancing the alloy's microstructural stability—an essential aspect for maintaining consistent mechanical properties in extreme thermal conditions. The incorporation of tungsten can significantly improve the mechanical properties of the alloy, meeting the requirements for high performance at elevated temperatures.

Titanium: Titanium, also maintaining its structural stability at high temperatures, proves to be a relevant choice for applications requiring mechanical resistance at extreme temperatures, such as 1200 °C [82, 83]. Its low coefficient of thermal expansion helps minimize thermal stresses and deformations of the alloy at high temperatures, promoting dimensional stability. By forming carbides and nitrides at high temperatures, titanium strengthens the alloy's metal matrix, significantly improving mechanical resistance, including tensile strength, creep resistance, and toughness. The addition of titanium can considerably enhance the mechanical properties of the alloy, meeting high-performance requirements at elevated temperatures.

Titanium can be synergistically associated with other alloying elements, such as chrome, nickel, and molybdenum, to form alloys resistant to corrosion and high temperatures. This synergy between elements enables achieving optimal mechanical properties and corrosion resistance. The ease of titanium fabrication is also a valuable advantage, simplifying the alloy production process. Additionally, titanium is also used in TaTiC4 developed by Saint-Gobain for carbide formation.

To distinguish the choice of the refractory element in the composition of CoCr-X ternary alloys, the alloys Co-Cr-Mo, Co-Cr-Ta, Co-Cr-Ti, and Co-Cr-W were developed by arc-melting under argon atmosphere. Since the Co-Cr-Ti alloy presented complete brittleness at room temperature, this composition was excluded for the selection of a ternary alloy. Subsequently, an initial prediction of the remaining compositions to understand the phases and behavior at 1200 °C was made using CALPHAD, and the results are presented in Table 1.2.

Table 1.2. Summary of results of CoCr-X ternary alloys
predicted by CALPHAD using TCHEA4 database.

Alloy composition (at%)	Assessment in TCHEA4 (database for CALPHAD)	Phases at 1200° C	Melting point (°C)	Hardness at room temperature
59.9Co-34Cr-6.1Mo	Partially	Mainly FCC + minor amount of sigma	1525 °C	442Hv
61.7Co-35.5Cr-3.35Ta	Partially	Mainly FCC + addition of C15 Laves phases	1365 °C	327Hv
61.7Co-35Cr-3.3W	Fully	Mainly FCC + minor addition of secondary phases	1406 °C	332Hv

From this table, we can see that all three alloys are promising, each with a reduced number of phases. Regarding phases, the presence of the sigma phase in the CoCrMo alloy may pose a problem as this phase is known to increase the brittleness of alloys. However, it is noteworthy that this alloy has a very high melting temperature of 1525 °C. Concerning the other
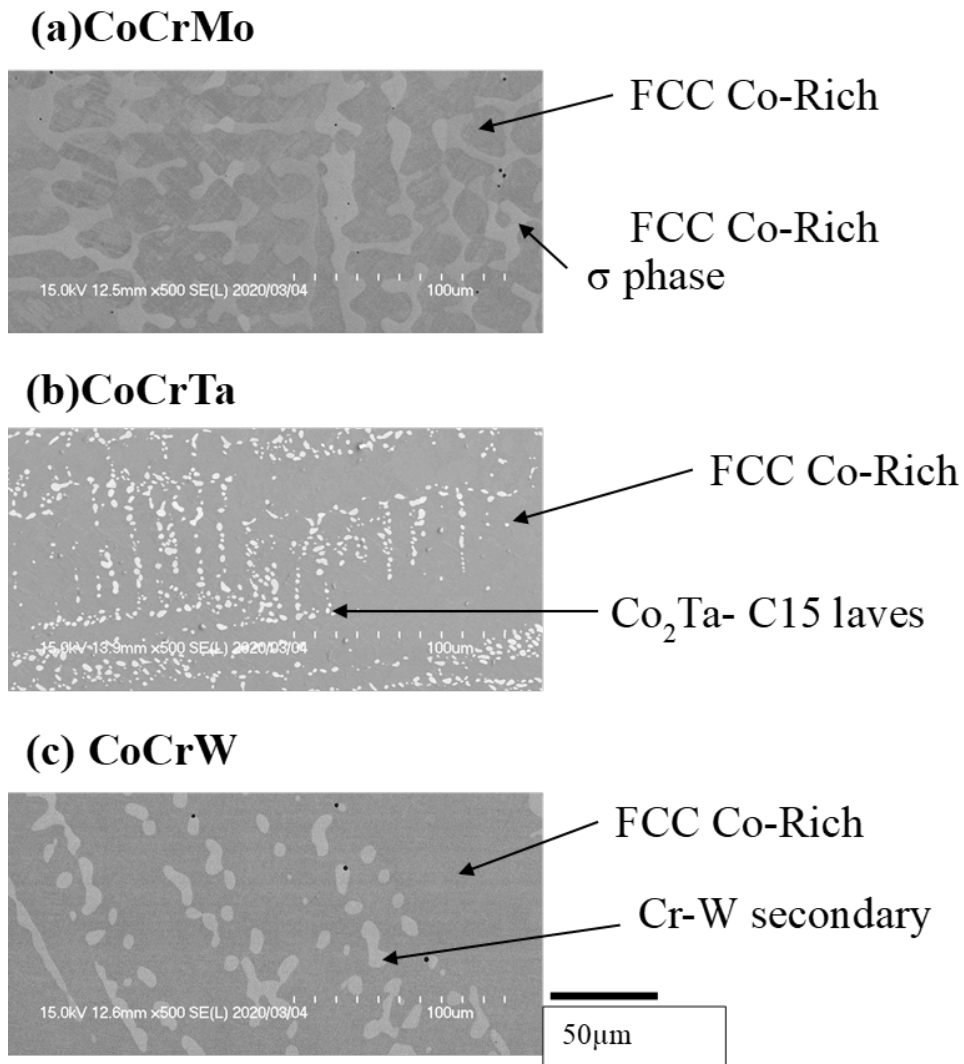
Figure 1.7. The microstructure of (a) CoCrMo, (b) CoCrTa, and (c) CoCrW.

alloys, CoCrTa also shows promise despite a melting temperature of 1365 °C, which is very close to TaTiC4 and glass fiber drawing applications. Ultimately, to ensure the accuracy of these predictions, an initial microstructural analysis was performed and presented in Fig. 1.7.

This figure distinctly illustrates the existence of Co-rich FCC phases as the primary component in the matrix for all the three compositions. Furthermore, consistent with CALPHAD predictions, CoCrMo reveals the presence of the sigma phase, CoCrTa exhibits the C15 Laves phase, and CoCrW showcases Co-W phases. These findings underscore the effectiveness and strategic advantages associated with leveraging predictive tools like CALPHAD in the alloy development process for high-temperature applications.

Subsequently, to distinguish between the three compositions, an oxidation resistance test at 1200 °C was conducted to assess their behavior. For this purpose, three specimens of each of the three ternary alloys, CoCr-X, were cut and placed on an alumina plate, which was then placed in a furnace heated to 1200 °C and left for 20 h. At the end of this period, the samples were removed, air-cooled, and subsequently examined, as depicted in Fig. 1.8:
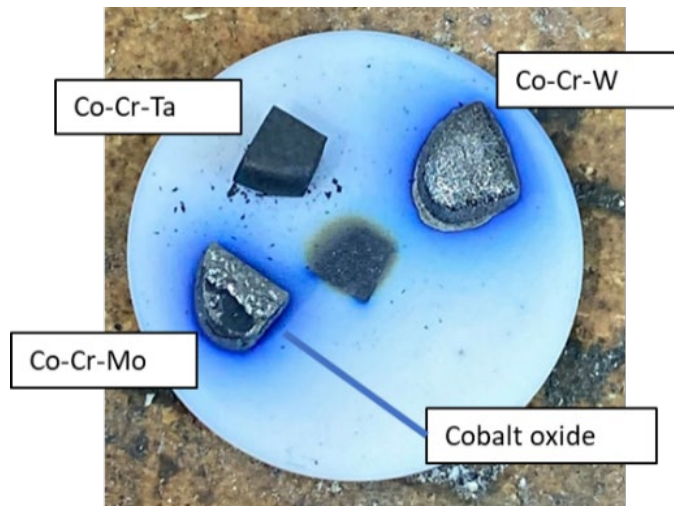
Figure 1.8. Appearance of CoCr-X alloys after oxidation test for 20 h at 1200 °C in air.

The samples exhibit distinct behaviors. Firstly, CoCrTa appears not to have formed a thick protective oxide layer like CoCrMo or CoCrW. Additionally, the observed oxide layer on these two compositions is highly fragile and easily detaches. Moreover, this alloy exhibits the absence of the blue halo, which is present around the other two alloys. This blue halo could indicate the diffusion of Co from the alloy.

The change in mass after oxidation has also been examined and is presented in Fig. 1. 9. This figure clearly depicts the significant mass gain in the Co-Cr-Mo and Co-Cr-W samples, which may correspond to the formation of a thick and brittle oxide layer on the specimens. Negative mass gain is evident in one of the Co-Cr-W samples, indicating complete detachment of the oxide layer. These findings favor Co-Cr-Ta as the preferred choice for robust oxidation resistance at 1200°C.
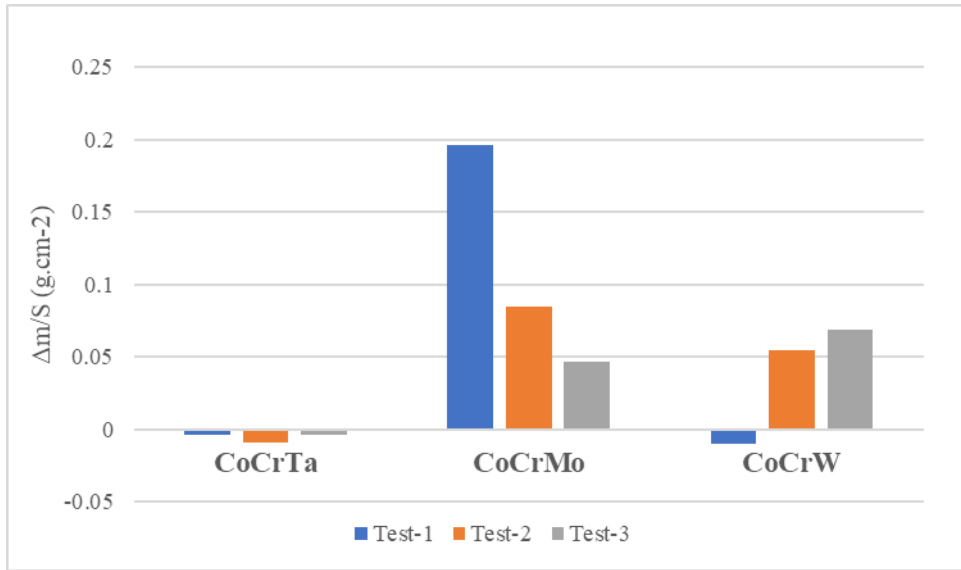
Figure 1.9. Mass change of CoCr-X alloys after oxidation test at 1200 °C for 20 h in air. The test was carried out three times for each alloy under the same conditions.

A characterization through SEM observation was also conducted for these samples and is presented in Fig. 1.10. These images reveal severe oxidation in the Co-Cr-Mo and Co-Cr-W alloys with the absence of the secondary phases observed before the test. In contrast, Co-Cr-Ta demonstrates more favorable results, exhibiting the presence of C15 Laves phases indicative of
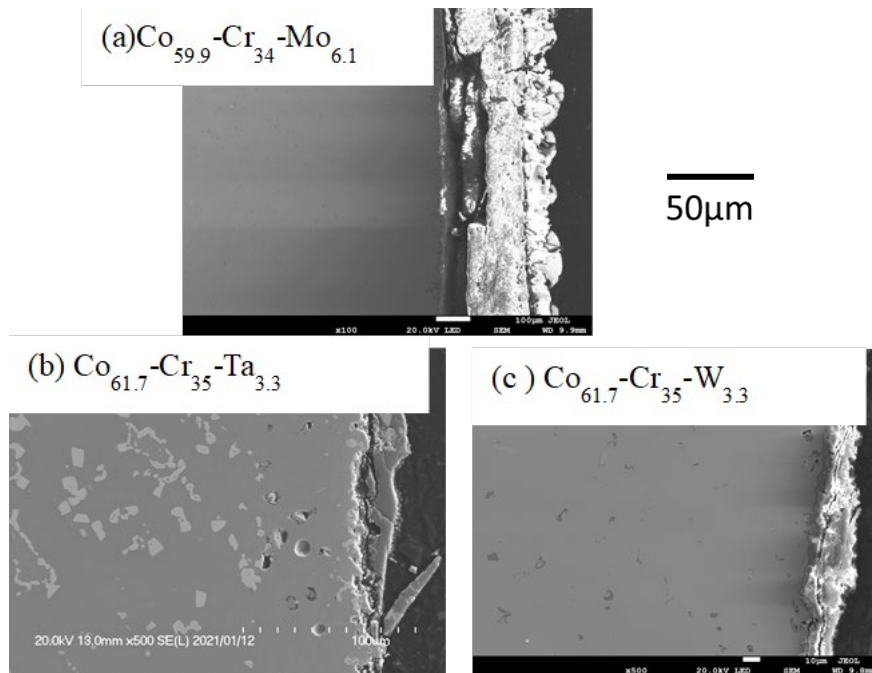
Figure 1.10. Microstructure of CoCr-X alloys after oxidation test for 20 h at 1200 °C in air.

improved high-temperature stability. Despite the formation of pores, the smaller amount of oxide layer in Fig. 1.10 and the significantly less mass gain in Fig. 1.9 make this composition the most promising candidate for this study. In conclusion, after a comprehensive exploration of various cobalt-based ternary alloys and evaluation for their potential in high-temperature applications, our study points conclusively to Co-Cr-Ta as the optimal choice. This family of alloys, characterized by its unique composition and performance attributes, emerged as the most promising candidate, showcasing enhanced stability, resistance to oxidation, and favorable mechanical properties at elevated temperatures. The decision to select Co-Cr-Ta is underpinned by a meticulous examination of empirical choices, predictive modeling using CALPHAD, and experimental results, reinforcing its superiority among the considered compositions. The coherent progression from alloy development to testing and characterization has provided valuable insights into the behavior of each alloy, ultimately guiding us towards a judicious choice for this study. The remarkable attributes of the CoCrTa alloy position it as the focal point for further investigations and applications in high-temperature environments, marking a significant milestone in the pursuit of advanced materials with superior thermal and mechanical characteristics.

1.3. Sample preparation

1.3.1. Synthesis and preparation of samples

The compositions of the Co-Cr-Ta alloys produced in this work are listed in Table 1.3. As one of the key elements for high temperature applications, Co was selected as the main component. Then, 20~40 at.% of Cr and 3~10 at.% of Ta were added to study the changes in microstructure and the resulting oxidation kinetics. The alloys were prepared by the arc melting method. The mixture of more than 99.9% pure starting elements was placed in a water-cooled copper mold and then arc-melted to form approximately 15 g of alloy buttons. In order to

homogenize the microstructure, each alloy button was then sealed in a quartz ampoule under argon and heat treated at 1200 °C for 24 h in box furnaces (SANSYO, MSFT-1520).

Table 1.3. Composition of CoCrTa alloys.

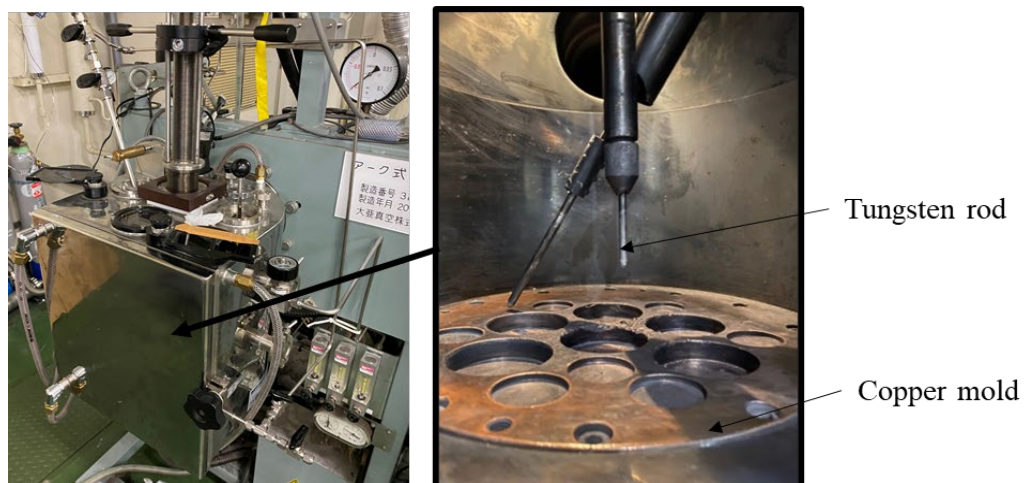| Alloy	Co (at.%)	Cr (at.%)	Ta (at.%)
CoCrTa-1	70.5	20	9.5
CoCrTa-2	67.3	25.4	7.3
CoCrTa-3	64.4	30.4	5.2
CoCrTa-4	61.7	35	3.35
CoCrTa-5	58.6	36.2	5.2
CoCrTa-6	55.2	37.6	7.2
CoCrTa-7	51.6	39	9.4

1.3.2. Fusion by arc melting method

Figure 1.11. Arc melting furnace used at NIMS.

The Arc Melting method, employed for synthesizing alloys in this study, involves using a consumable tungsten electrode within an argon-filled enclosure. The fusion support consists of copper and is cooled using pressurized water. The process begins by achieving a vacuum pressure of 2×10^{-5} Pa through a pump, followed by the introduction of argon into the chamber to prevent oxidation during the melting process. A 20 kV electric arc is then ignited on a titanium button, weighing approximately 15 g, which captures any residual oxygen upon melting.

While this device allows the production of semi-spherical samples weighing 15 g, it lacks control over solidification conditions. Consequently, the resulting elaborations exhibit various issues such as grain orientation, uneven distribution of elements, and numerous defects.

1.3.3. Heat treatment of samples

After being produced using arc melting, the samples are cut and sealed in quartz ampoules filled with argon gas to prevent oxidation. To achieve a more uniform microstructure for the alloys, a heat treatment temperature close to the estimated melting temperature for this alloy family is selected. In this study, a heat treatment of 24 hours at 1200 °C was applied for the Co-Cr-Ta family of alloys.

Figure 1.12. Samples sealed in quartz ampoule with argon gas.

1.3.4. Cutting of samples

After the completion of the heat treatment, the samples are cut according to their intended applications. For simple shapes required for XRD or SEM characterization, traditional cutting devices are used. However, for more complex shapes like small cylinders needed for DTA and TGA applications, the samples are cut using electric discharge machining (EDM). EDM is an electrothermal process where a thin, single-strand metal wire (typically copper) with

Figure 1.13. EDM wire cutting machine used at
NIMS.

de-ionized water is employed to conduct electricity, enabling the wire to cut through metal via heat generated by electrical sparks while preventing oxidation. Due to the inherent capabilities of this process, Wire EDM can easily machine complex and precise components from hard conductive materials. To achieve the desired geometry, the EDM tool is guided along the pre-programmed path inside the machine's software. In this study, the technique is performed using SODICK AG360L.

1.3.5. Sample mounting for polishing

The mounting of parts for polishing varies depending on the intended application. For scanning electron microscope (SEM) analysis, the samples are initially coated with a conductive POLYFAST powder, and then heated to 180 °C, causing the powder to melt and form Ø25 mm cylinders upon cooling to room temperature (as shown in Fig. 1.14(b)). However, for X-ray diffraction (XRD) analysis, where the presence of the C-rich POLYFAST powder would interfere with the results, the samples cannot be mounted using this method.
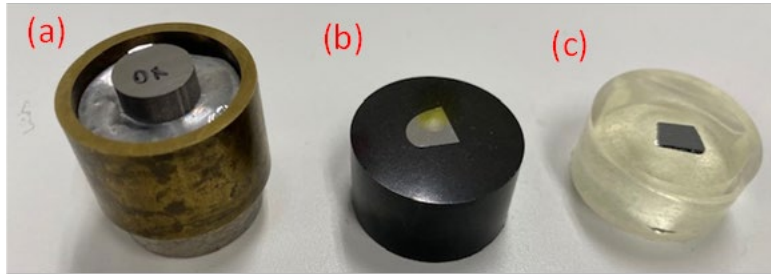
Figure 1.14. Three mounting methods: (a) wax, (b) POLYFAST conductive powder, and (c) epoxy resin.

To enable polishing for XRD analysis, a Ø21 mm metal cylinder is heated to around 300 °C so that a point of wax on its top melts. The sample is then placed on the wax and left to cool, firmly securing the sample to the cylinder. To ensure a perfectly flat polishing surface, a protective brass ring of Ø25 mm is placed around this assembly (as shown in Fig. 1.14 (a)).

After the polishing process is completed, the entire assembly is heated again to melt the wax, allowing the sample to be carefully removed. Subsequently, the part is immersed in acetone and placed in an ultrasonic bath to remove any residual wax.

Regarding samples immersed in molten glass, using the POLYFAST conductive powder is not feasible as the pressure during its solidification to form the Ø25 mm cylinder could damage the delicate glass layer attached to the metal. In such cases, the samples are mounted using epoxy-type resin, as illustrated in Fig. 1.14(c), to preserve the fragile glass-metal interface.

1.3.6. Polishing of materials

Mounted on an automatic polishing machine, the alloy undergoes a meticulous polishing process tailored for characterization. The initial grinding phase involves the application of 15 N force for 1 minute and 30 seconds, utilizing an abrasive with a particle size of 340/420. Subsequently, the polishing stage employs a 15 N force for 5 minutes, transitioning through multiple abrasive steps: 9µm with an ultrapad, followed by 4 minutes with 3µm, and concluding

with 3 minutes using 1μm poly-crystalline abrasive. The final finishing stage entails a 15 N force for 4 minutes, employing a chemomet abrasive with a particle size of 0.05 μm, followed by a 2-minute treatment with Mastermet colloidal silica polishing suspension and an additional 2 minutes without it. This precisely orchestrated polishing sequence aims to achieve a finely polished surface, crucial for the accurate characterization of the alloy's properties.

1.4. Structural characterization

1.4.1. X-ray diffraction pattern (XRD)

Phase identification was carried out by the X-ray diffraction method (XRD) (MINIFLEX, Rigaku). In the XRD analysis, the Cr Kα X-ray target ($\lambda = 2.2909$ Å) was used to reduce the fluorescent X-ray of Co. The intensity was measured every 0.02° in the 2θ range from 30 to 140° with a scan speed of 7°. After screening the possible phases using the Smartlab Studio II software, they were confirmed by comparing the interplanar distance (dhkl) calculated from the diffraction patterns with those from the International Centre for Diffraction Data (ICDD) cards of the highest quality [6]. From the set of d values, the crystal structure and the lattice parameter a (Å) of a specific phase were identified using codes such as $d_{hkl} = \frac{a}{\sqrt{h^2+k^2+l^2}}$ for a cubic phase, $d_{hkl} = \frac{a}{\sqrt{h^2+k^2+\frac{a^2}{c^2}l^2}}$ for a tetragonal phase, and $d_{hkl} = \frac{a}{\sqrt{4/3(h^2+hk+k^2)+\frac{a^2}{c^2}l^2}}$ for a hexagonal phase for a given (hkl) crystal orientation.

1.4.2 Scanning electron microscopy with energy dispersive X-ray spectroscopy (SEM-EDS)

Microstructure observation and local chemical analysis were conducted by scanning electron microscopy (SEM) and energy dispersive X-ray spectroscopy (EDS), respectively. For this purpose, a scanning electron microscope equipped with energy dispersive spectroscopy (JSM–7200F, JEOL) was used. Samples for SEM–EDS were first mounted in conductive resin

(Polyfast) and then polished using emery paper up to 400 grit (38 µm), followed by the Metadi supreme Polycrystalline Diamond suspension up to 1 µm, and finally finished with a Chemomet cloth and Mastermet colloidal silica polishing suspension etching (up to 0.5 µm). The microstructure was observed mainly in the backscattering electron mode (BSE). The chemical analysis by EDS was carried out at an accelerating voltage of 20 kV. The composition of the phases observed in a BSE image was determined by averaging at least twenty point–analysis measurements. The mole fraction (%) of each phase was estimated from the measured element concentrations of each phase by solving the following simultaneous equations:

$$\sum_i Vf_i = 1, \tag{2.1}$$

$$\sum_i Vf_i C_{j,i} = C_{j,N}, \tag{2.2}$$

where Vf_i is the mole fraction of the ith phase, $C_{i,j}$ is the composition of the jth element in the ith phase, $C_{j,N}$ is the nominal composition of the jth element, respectively.

Elemental mapping of each constituent was also carried out to analyze the distribution of the element.

1.5. Differential thermal analysis (DTA)

Differential thermal analysis is used in this thesis to determine possible phase changes as well as solidus and liquidus temperatures of alloys during temperature rise. It is carried out with a SETARAM SETSYS- 24 machine. First, the first temperature rise is carried out at a rate of 20 °C per minute up to 1700 ° C.

Figure 1.15. Differential thermal analysis machine SETARAM SETSYS-24 used at NIMS.

Successively, cooling is done in a similar way to room temperature. The operation is repeated twice.

1.6. Oxidation tests

1.6.1. Thermogravimetric test at 1200 °C for 100 h

A thermogravimetric test involves monitoring the mass variation of a sample over time at a selected temperature. For this purpose, a SETARAM TAG24-18S thermobalance connected to a computer is used. The device's oven is capable of heating up to 1600 °C, allowing precise temperature control for the sample. Additionally, a microbalance is integrated into the machine to track the sample's mass evolution concerning temperature and time. Temperature measurement is performed using a thermocouple positioned near the sample.

To conduct the test, the samples are placed in alumina crucibles, suspended from the machine's beam by platinum wires. Another empty crucible, also suspended with a platinum wire, serves as a reference to measure weight variations and to account for platinum evaporation effects at temperatures above 1000 °C. By using this reference, the experiment can accurately detect changes in the sample's mass due to the growth of oxides formed during the tests, assuming these oxides remain solid and adhere to the sample's surface.

The tested samples are cylindrical, with, approximately, 1 mm in diameter, 10 mm in length, and a weight of around 200 mg. To prevent preferential oxidation on edges or corners, the sample's edges are polished using SiC paper. The sample is then placed in

Figure 1.16. SETARAM TAG24-18S.

one of the alumina crucibles at room temperature, while the second crucible is kept under vacuum throughout the experiment, as previously described.

The experiment involves heating the sample at a rate of 10 °C/min until it reaches 1200 °C, where it is held for 100 h at this temperature. Subsequently, the sample is cooled back to room temperature. To monitor the oxidation evolution precisely throughout the experiment, the initial mass gain is recorded, and subsequently, new mass gains are recorded every 30 seconds. This meticulous recording of mass gain provides accurate tracking of the oxidation progression during the entire experiment.

1.6.2. Isothermal oxidation test at 1200 °C for 20 h in air

In order to characterise the microstructural changes of the alloys by the oxidation test, some larger samples of 5 x 5 x 1 mm were oxidised in a muffle furnace maintained at 1200 °C in air for 20 hours. Each sample, placed in an Al_2O_3 crucible, was placed on a ceramic plate, then the plate was automatically pushed into the furnace heated to the target temperature. After 20 hours of oxidation, the samples were slid out of the furnace and air cooled to room temperature. The mass changes of the samples with the crucible were measured by the electric balance, so that the total mass changes including the spalled oxides were considered.

Alternatively, the samples were placed on Al_2O_3 ceramic plate directly and then put into a muffle furnace. In this case, the sample mass change was measured without the spalled oxides.

1.6.3. Cyclic oxidation test at 1200 °C in air

When it comes to the industrial application, the materials are not in a continuous use until their properties dropped to a critical aspect; they undergo thermal shock due to, for example, production stoppage or maintenance requirements. These events return the material temperature to ambient temperature, at not controlled speeds, thereby generating high thermal stresses due to a large difference in expansion coefficient between the alloy and its oxide. It is

therefore necessary to supplement the data obtained for alloys after isothermal oxidation with cyclic oxidation tests.

Specimens of similar geometry and dimensions to those of the isothermal oxidation tests are used. The experimental protocol consists of 20 cycles of high temperature holds for one hour followed by air quenching for 10 minutes and weighing. For this test, the alloys are set on an alumina plate. A box furnace, set the targeted temperature at 1200 °C, moves forward to the sample position and backward to the position away from the samples, letting them heat up and cool down repeatedly. The mass change of each sample with the number of cycles was recorded to evaluate their oxidation resistance.

1.7. Mechanical tests

1.7.1. Tensile test

Figure 1.17. Bulk (3.5 kg) of CoCrTa after cutting cylinders for tensile tests via EDM.

A 7 kg ingot of the chosen composition was forged using an induction furnace and then cut in half with an electric saw. The halves were further segmented into several 10 mm-diameter cylinders using electrical discharge machining (EDM). Subsequently, these cylinders were placed under argon gas and underwent a 24-hour heat treatment at 1200 °C. Finally, the treated

cylinders were sent to the company responsible for shaping the samples and conducting the tests.

For each composition tested, two specimens are tested at room temperature, and two specimens are tested in-situ at 1200 °C. The sample is securely fastened into a tensile testing machine, ensuring that the force is uniformly applied across the entire cross-sectional area of the specimen. The testing machine gradually applies a tensile force to the specimen. The force is typically applied steadily and continuously, although some variations may occur depending on the type of test. Throughout the test, the machine measures and records the applied force and the deformation experienced by the specimen. These data are utilized to generate a stress-strain curve, illustrating how the material responds to stress. Furthermore, these tests allow us to determine elongation, 0.2% proof stress, ultimate tensile strength, and the fracture location of the specimens. These tests were conducted by a company outside of NIMS to ensure certified and normalized results.

1.7.2. Micro hardness Vickers

The microhardness measurements at room temperature were performed using a Buehler MicroMet 5104 micro hardness tester. This type of test involves optically measuring the diagonals of the mark left by a square-based diamond pyramid indenter with an apex angle of 136 °. The strength applied by the diamond tip can vary within a range of 98 mN to 9.807 N. Here, 5 measurements at each load were performed for 10 seconds per indentation.

1.7.3. High temperature micro Vickers

In a similar manner than the microhardness test, an in-situ hardness test at different temperatures was performed. Specimens with dimensions of 5x5x10 mm were cut using Electrical Discharge Machining (EDM) and securely affixed within the testing apparatus. Throughout the test, the sample holder underwent controlled movement beneath the indenter,

where three 10-second indentations were made. Subsequently, the sample holder returned to its original position, allowing for microscopic observation of the indents and the calculation of Vickers hardness. This procedure was repeated at intervals of 200 °C up to 600 °C and at intervals of 100 °C beyond that temperature. Conducting this measurement at high temperatures poses challenges, as the brilliance of the sample can hinder observation. Moreover, beyond 1000 °C, there is a risk of the protective glass undergoing combustion, potentially obstructing the measurement entirely. Despite these challenges, this test provides valuable insights into the compositions' in-situ behavior at diverse temperature ranges.

Chapter 2: Microstructure of the Co-Cr-Ta alloy system [84]

2.1. Preparation of Co-Cr-Ta samples

In this study, we fabricated Co-Cr-Ta alloys with compositions detailed in Table 2.1. Cobalt was selected as the primary element due to its significance in high-temperature applications. We then incorporated chromium (20–40 at%) and tantalum (3–10 at%) to investigate their effects on the microstructure and oxidation behavior. The alloys were synthesized using the arc-melting method. Over 99.9% pure source elements were arc-melted to produce approximately 15 g alloy buttons. These buttons were subsequently heat treated at 1200 °C for 24 h in a sealed quartz ampoule under argon atmosphere, followed by air cooling, to achieve a homogeneous microstructure.

Table 2.1. Composition of CoCrTa alloys [84]. Table 2.1 is adapted from the table in the journal of alloys and compounds , vol. 936, year 2023, 167968, by Moreau Louis Etienne, Gorsse Stéphane, Lambard Guillaume, Murakami Hideyuki.

Alloy	Co (at.%)	Cr (at.%)	Ta (at.%)
CoCrTa-1	70.5	20	9.5
CoCrTa-2	67.3	25.4	7.3
CoCrTa-3	64.4	30.4	5.2
CoCrTa-4	61.7	35	3.35
CoCrTa-5	58.6	36.2	5.2
CoCrTa-6	55.2	37.6	7.2
CoCrTa-7	51.6	39	9.4

2.2. Microstructure

The X-ray diffraction patterns of the cast Co-Cr-Ta alloys annealed at 1200 °C for 24 hours are shown in Figure 2.1. All alloys have two face centred cubic (FCC) phases and one hexagonal close packed (HCP) phase. In addition, the CoCrTa-5, -6 and -7 alloys contained a tetragonal phase.
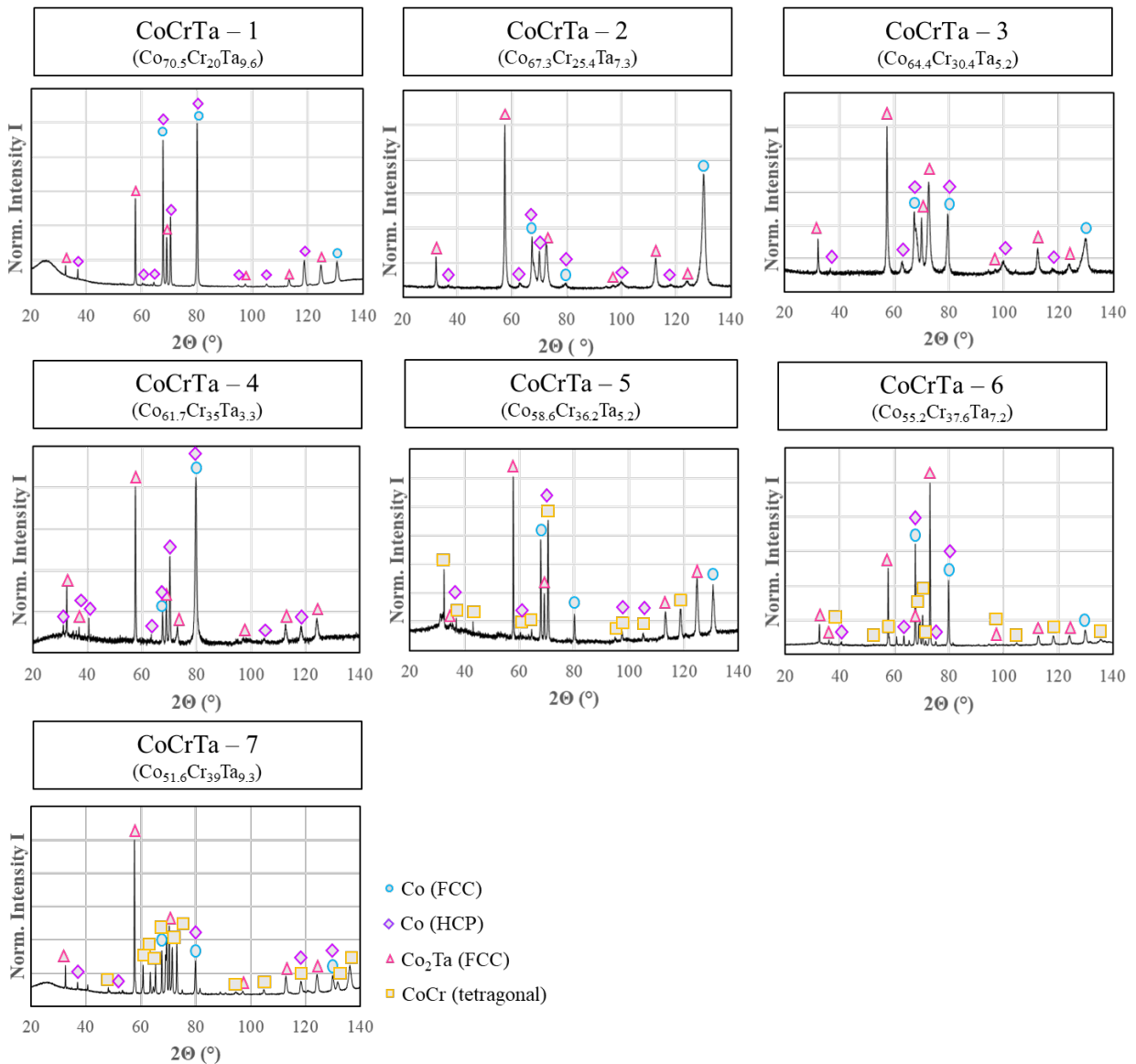

Figure 2.1. X-ray diffraction patterns of the CoCrTa alloys prepared by casting followed by annealing at 1200 °C for 24 h [84]. Figure 2.1 is adapted from the figure in the journal of alloys and compounds, vol. 936, year 2023, 167968, by Moreau Louis Etienne, Gorsse Stéphane, Lambard Guillaume, Murakami Hideyuki.
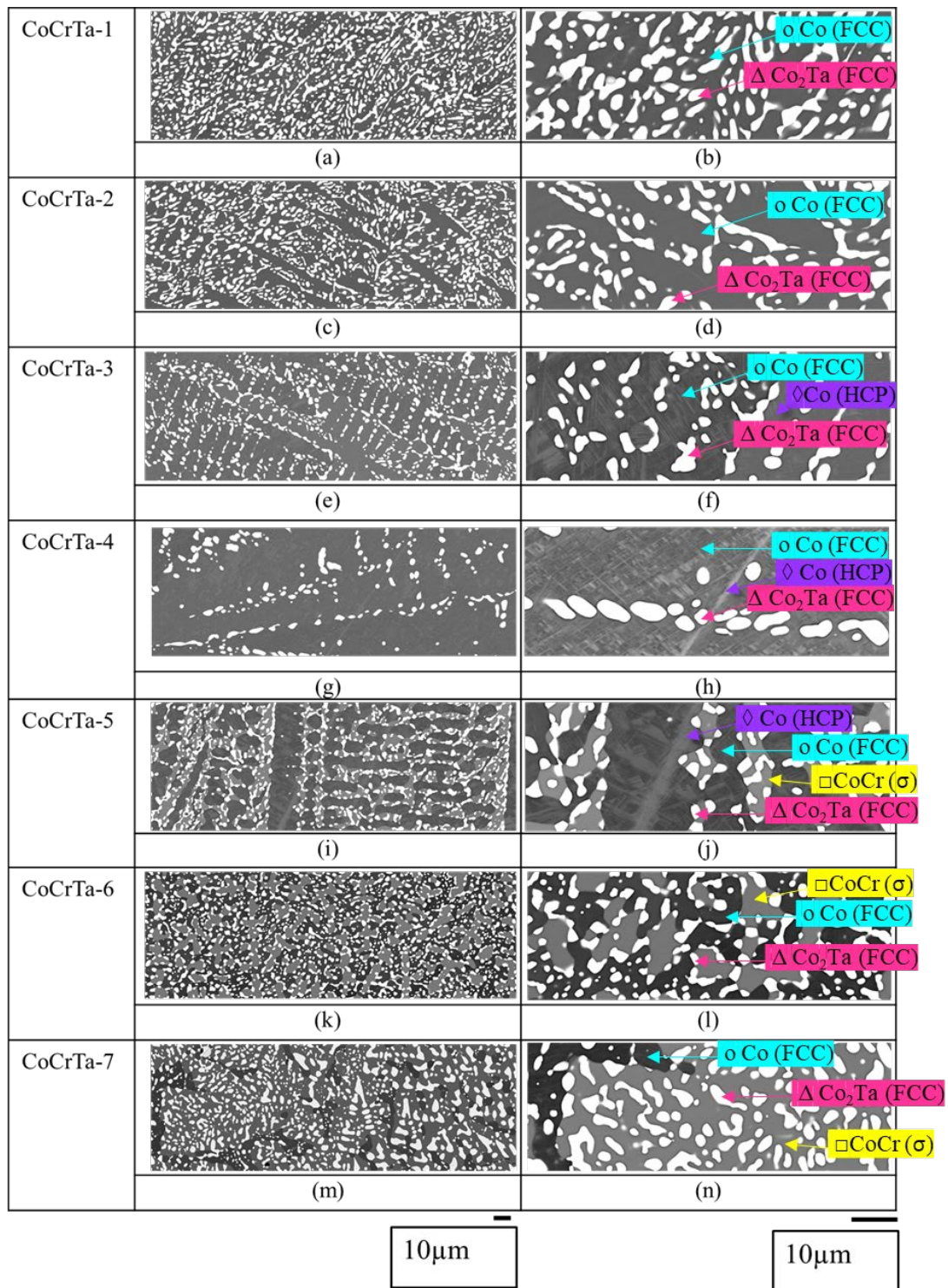
Figure 2.2. BSE images of CoCrTa alloys prepared by casting followed by annealing at 1200 °C for 24 h: (a), (c), (e), (g), (i), (k), and (m) low magnification images showing the dendritic microstructure, and (b), (d), (f), (h), (j), (l), and (n) higher-magnification images showing details of the Ta-rich phase [84]. Figure 2.2 is adapted from the figure in the journal of alloys and compounds, vol. 936, year 2023, 167968, by Moreau Louis Etienne, Gorsse Stéphane, Lambard Guillaume, Murakami Hideyuki.

Table 2.2. Composition (at.%) of the phases observed in the CoCrTa alloys prepared by casting followed by annealing at 1200 °C for 24 h, in comparison with the equilibrium compositions at 1200 °C predicted using TCHEA4. The predicted phases and their equilibrium compositions are given in parentheses [84]. Table 2.2 is adapted from the table in the journal of alloys and compounds, vol. 936, year 2023, 167968, by Moreau Louis Etienne, Gorsse Stéphane, Lambard Guillaume, Murakami Hideyuki.

Phases	Phase fraction(%)	Co	Cr	Ta
CoCrTa-1		**70.5**	**20**	**9.5**
Darker region (FCC+HCP)	60 (69)	74 (72)	24 (27)	2 (1)
Brighter region (C15 Laves)	40 (31)	67 (67)	12 (5)	21 (28)
CoCrTa-2		**67.3**	**25.4**	**7.3**
Darker region (FCC+HCP)	73 (76)	68 (68)	30 (31)	2 (1)
Brighter region (C15 Laves)	27 (24)	63 (66)	16 (6)	21 (28)
CoCrTa-3		**64.4**	**30.4**	**5.2**
Darker region (FCC+HCP)	82 (84)	65 (64)	33 (35)	2 (1)
Brighter region (C15 Laves)	18 (16)	60 (65)	19 (7)	21 (28)
CoCrTa-4		**61.7**	**35**	**3.35**
Darker region (FCC+HCP)	92 (90)	62 (61)	37 (38)	1 (1)
Brighter region (C15 Laves)	8 (10)	57 (64)	23 (8)	20 (28)
CoCrTa-5		**58.6**	**36.2**	**5.2**
Dark dendrites (FCC+HCP)	73 (75)	60 (59)	39 (40)	1 (1)
Brighter region (C15 Laves)	19 (17)	56 (63)	23 (9)	21 (28)
Gray region (s)	8 (8)	49 (44)	48 (56)	3 (0)
CoCrTa-6		**55.2**	**37.6**	**7.2**
Darker region (FCC+HCP)	39 (43)	60 (59)	38 (40)	2 (1)
Brighter region (C15 Laves)	28 (25)	56 (63)	23 (9)	21 (28)
Gray region (s)	33 (32)	49 (44)	48 (56)	3 (0)
CoCrTa-7		**51.6**	**39**	**9.4**
Darker region (FCC+HCP)	1 (9)	53 (59)	39 (40)	8 (1)
Brighter region (C15 Laves)	36 (33)	49 (63)	29 (9)	22 (28)
Gray region (s)	63 (58)	44 (44)	53 (56)	3 (0)

To examine the microstructure, observation by SEM and analysis by EDS were carried out. Figure 2.2 shows BSE images of the cast alloys They exhibit dendritic microstructures after casting and annealing at 1200 °C. Basically, the microstructure of CoCrTa alloys (CoCrTa-1 to -7) consists of a Co-rich phase (darker region) and a Co_2Ta phase (brighter region). In addition, CoCrTa-5, 6, and 7 show a CoCr sigma phase (gray region), which is consistent with X-ray diffraction patterns shown in Fig. 2.1. The Co-rich phase is composed of a mixture of a FCC phase and a HCP phase for CoCrTa-3 to -5), while it is a FCC phase aolone for CoCrTa-1, 2, 6, and 7. Each phase observed in Fig. 2.2 was analyzed using EDS and the results are tabulated in Table 2.2. Here, the composition of the phases in the BSE image was determined by averaging at least twenty point–analysis measurements within a phase. The mole fraction (%) of each phase was estimated from the measured element concentrations of each phase by solving the equations (2.1) and (2.2), as described in Section 1.2.2. These experimentally obtained data are compared with the phases and their equilibrium compositions (in the parentheses) predicted by TCHEA4 in the next section.

2.3. Use of CALPHAD

The equilibrium phase diagrams for the Co-Cr-Ta alloys in Figure 2.3 have been calculated using the CALPHAD method. The Thermocalc software with the TCHEA4 thermodynamic database was used. As shown in Figure 2.3(a), CoCrTa-1 to -4 are predicted in the Co-rich FCC + FCC C15 Laves phase field at 1200 °C. The C15 Laves phase has a composition close to the Co2(Cr,Ta) stoichiometry. As the alloy composition is shifted towards the Cr and Co rich direction along the composition line from CoCrTa-1 to -4, the proportion of the Co-rich FCC phase increases. This trend is in good agreement with Table 2.2. As the Cr content continues to increase, CoCrTa-5, 6 and 7 fall into the ternary phase field where the Co-rich FCC, (Co, Ta)-rich C15 Laves phase equilibrates with the (Co, Cr)-rich σ phase. As the alloy composition moves along the 5-7 composition line towards the Ta- and Cr-rich regions,

the fraction of the Co-rich FCC phase decreases and the fractions of the C15 Laves and σ phases increase, while the compositions of the equilibrium phases remain the same. This phenomenon is also observed in Table 2.2.

Consequently, the predicted equilibrium phase fractions and compositions corroborate experimental results (Table 2.2) and facilitate the identification of the phases observed by BSE (Fig. 2.2) and detected by XRD (Fig. 2.1). However, the presence of a Co-rich HCP phase is not predicted from the phase diagram at 1200 °C (Fig. 2.3(a)). In CoCrTa-4 to -7 (Figures 2.2(f),
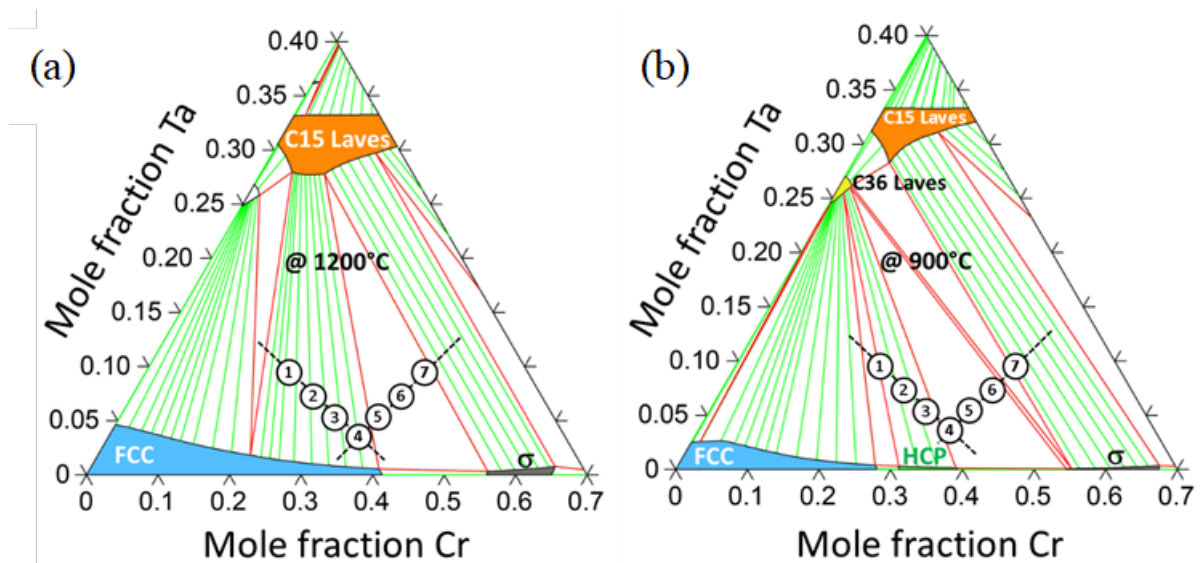

Figure 2.3. Isothermal section of the ternary Co-Cr-Ta phase diagram calculated at (a) 1200 °C and (b) 900 °C using TCHEA4. The prepared alloys are shown by numbers surrounded by circles [84]. Figure 2.3 is adapted from the figure in the journal of alloys and compounds, vol. 936, year 2023, 167968, by Moreau Louis Etienne, Gorsse Stéphane, Lambard Guillaume, Murakami Hideyuki.

(h) and (j)), the Co-rich phase exhibited a band-like structure with a specific direction, indicating the FCC→HCP martensitic transformation commonly observed in martensitically transformed duplex Co-based alloys[85]. Figure 2.3(b) shows the calculated isothermal ternary phase diagram for the Co-Cr-Ta system at 900°C, supporting the hypothesis that the martensitic transformation of the Co-rich phase will occur during cooling.

2.4. Summary

In summary, the microstructure and phase constitution of a series of Co-Cr-Ta alloys (Cr:20 to 39 at%, Ta:5.2 to 9.5 at%) have been investigated and the results compared with the CALPHAD predictions. The following conclusions can be drawn.

- All the alloys investigated have a Co-rich solid solutioned phase (a mixture of FCC and HCP phases) and a Co_2Ta-based C15 Laves phase. With increasing Cr-content, an additional Cr-rich σ phase precipitates.

- The phase constitutions experimentally obtained are in good agreement with those predicted by a CALPHAD method, demonstrating its accuracy in forecasting alloy behavior.

Chapter 3: Oxidation behavior of Co-Cr-Ta alloys

3.1. Oxidation for 20 h at 1200 °C in air

3.1.1. Microstructure after oxidation

Samples of dimensions 5 mm x 5 mm x 1 mm were oxidised at 1200°C in air for 20 hours using a muffle furnace. The samples were placed in Al_2O_3 crucibles, which were then positioned on a ceramic plate and inserted into the furnace that had been preheated to the desired temperature. Following the oxidation process, the samples were taken out of the furnace and allowed to cool to room temperature in air. The change in mass of the samples was measured by weighing the sample with the crucible. This ensures that the total mass change includes the spalled oxides.

Cross-sectional images of the surface oxide layers after 20 hours of exposure in air at 1200°C are presented in Figure 3.1. The compositions of the oxides were determined using EDS measurements, and the results are summarised in Table 3.1. The cast alloys exhibit a similar oxide formation, consisting of an inner oxide layer rich in Ta and Cr (oxide 1), identified as $CrTaO_4$, and an outer oxide layer (oxide 2), identified as Cr_2O_3. However, CoCrTa-1, -2, and -5 alloys form a third oxide layer (oxide 3) that is rich in Co on top of oxide 2. It is important to note that these alloys also contain a higher amount of Co in both the oxide 1 and 2 layers, as shown in Table 3.1. Additionally, CoCrTa-1 shows that the formation of $CrTaO_4$ is limited to the creation of Cr and Ta-rich particles on the surface, while a thick and fragile Cr_2O_3 oxide layer is formed. The presence of numerous pores within the alloy suggests inadequate oxidation resistance. The pore count is similar to that of CoCrTa-5. CoCrTa-1, -2 and -5 also exhibit the creation of a dispersed $CrTaO_4$ oxide layer. Conversely, CoCrTa-3, -4, -6 and -7 generate a

continuous CrTaO$_4$ layer, with thickness increasing as the amount of Cr and Ta increases. It is worth noting that the formation of a continuous CrTaO$_4$ layer reduces the number of pores in the alloy.

Among all the alloys tested, CoCrTa-6 and -7 have the most continuous CrTaO$_4$ oxide layer, which confirms their superior oxidation resistance.

Figure 3.1. BSE image of Co-Cr-Ta samples after oxidation for 20 h at 1200 °C in air (see Table 4.1 for the composition of areas 1, 2, and 3) [84]. Figure 3.1 is adapted from the figure in the journal of alloys and compounds, vol. 936, year 2023, 167968, by Moreau Louis Etienne, Gorsse Stéphane, Lambard Guillaume, Murakami Hideyuki.
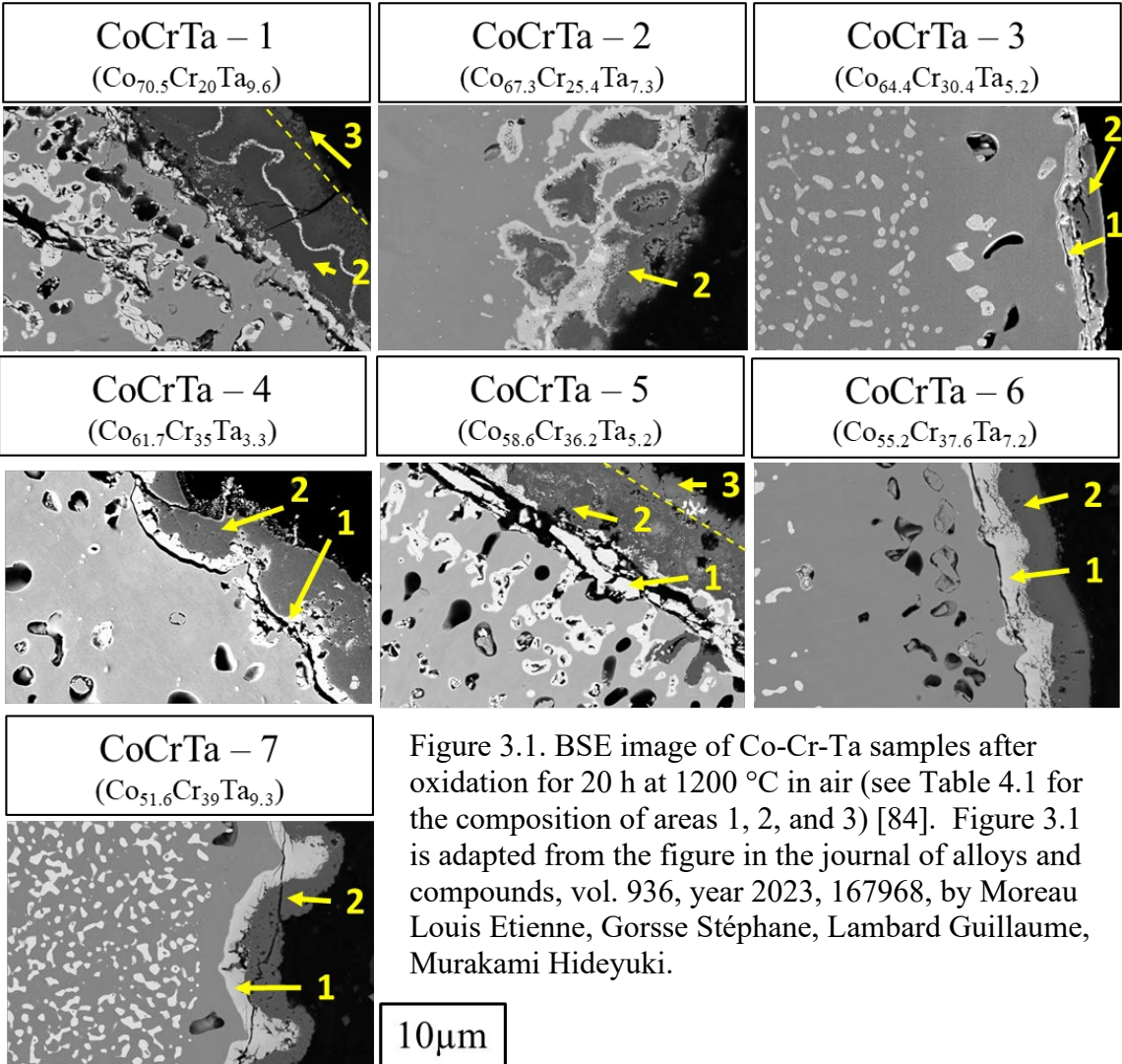
Table 3.1. Composition (at.%) of the oxides observed in the Co-Cr-Ta alloys after oxidation at 1200 °C for 20 h [84]. Table 3.1 is adapted from the table in the journal of alloys and compounds, vol. 936, year 2023, 167968, by Moreau Louis Etienne, Gorsse Stéphane, Lambard Guillaume, Murakami Hideyuki.

EDS analysis :	Oxide 1 (CrTaO$_4$)				Oxide 2 (Cr$_2$O$_3$)				Oxide 3			
Alloys	Co (at%)	Cr (at%)	Ta (at%)	O(at%)	Co (at%)	Cr (at%)	Ta (at%)	O(at%)	Co (at%)	Cr (at%)	Ta (at%)	O(at%)
CoCrTa-1					1	48	0.4	51	49	14	11	26
CoCrTa-2	7	17	25	51	2	46	1	52	19	29	2	50
CoCrTa-3	3	19	28	50	0.2	48	0.8	51	13	13	22	53
CoCrTa-4	2	22	21	55	0.3	48	0.1	51				
CoCrTa-5	3	26	18	53	0.3	46	1	53	14	32	1	53
CoCrTa-6	1	23	23	53	0.1	46	0.1	54				
CoCrTa-7	1	22	24	53	0.2	48	0.1	52				

3.1.2. Optimisation of Co-Cr-Ta compositions with the help of machine learning method

After the oxidation test at 1200 °C for 20 h by TGA, the mass gain of the above Co-Cr-Ta alloys was measured, and the results were presented in Fig. 3.2(b). Figures 3.2(a) shed the light on the comparative oxidation kinetics of the Co-Cr-Ta alloys. The correlation matrix shows that the mass gain is positively correlated with the Ta content in the alloy and the fraction of the C15 Laves phase. Conversely, there is a strong negative correlation between the mass gain and the Cr content in the alloy, the Cr content in the FCC phase, and the solidus temperature. However, it is important to take in consideration the relatively low number of samples composing our database so far. For example, mass gain after 20 h of oxidation for CoCrTa-1 is measured of 0. 0225 g.cm^{-2} for a volume fraction of 40% of C15 laves phases. On the other hand, mass gain after 20 h of oxidation for CoCrTa-5, -6 and -7 is measured of 0. 005 g.cm^{-2} for a volume fraction of 19%, 28% and 36% of C15 laves phase, respectively. The mass gains of these alloys are almost 5 times lower than that of CoCrTa-1, which will impact noticeably the Pearson correlation. Future addition of compositions in the database will improve greatly the precision of the Pearson correlation parameter. Based on the Pearson's map, the mass gain after oxidation test for 20 h at 1200 °C was plotted as a function of the Cr content in Fig. 3.2(b).
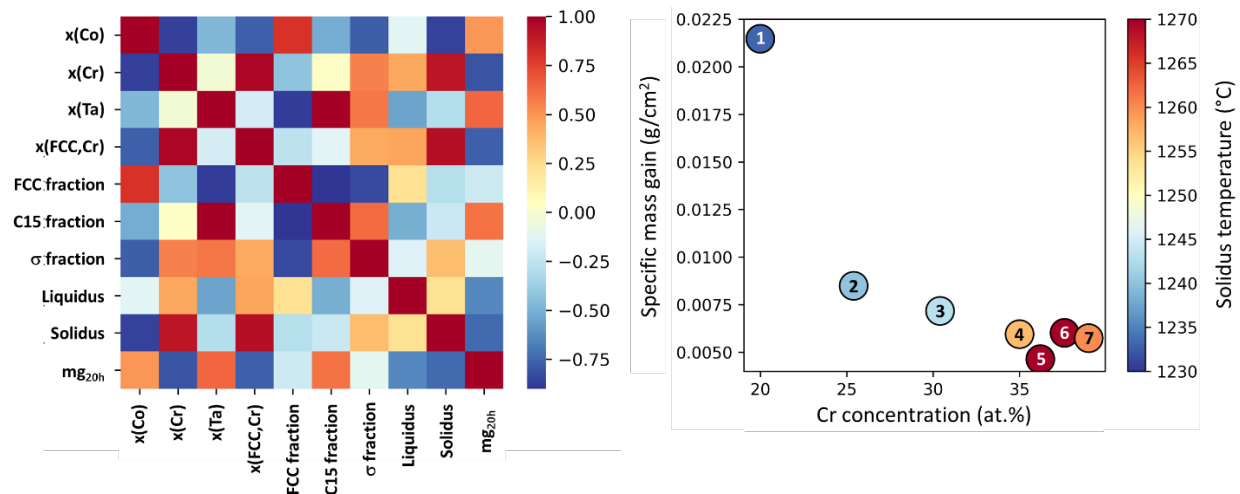
Figure 3.2. (a) Heat map of Pearson linear correlation coefficient matrix among alloy composition, present phases, liquidus and solidus temperature of the alloys, and the mass gain after oxidation test for 20 h at 1200 °C by TGA. The colour bar indicates the degree of correlation between a pair of features and (b) specific mass gain after oxidation at 1200 °C for 20 h by TGA as a function of Cr concentration and solidus temperature for Co-Cr-Ta alloys (corresponding alloy number is shown inside each circle) [84]. Figure 3.2 is adapted from the figure in the journal of alloys and compounds, vol. 936, year 2023, 167968, by Moreau Louis Etienne, Gorsse Stéphane, Lambard Guillaume, Murakami Hideyuki.

Additionally, the solidus temperature of each alloy in the figure is indicated by the colour chart.

This figure clearly highlights the importance of Cr content and the melting temperature of the alloy affecting the oxidation resistance.

Based on the observation described above, there are two ways to design Co-Cr-Ta alloys with improved oxidation resistance: exploring the Cr-rich regions with higher melting temperatures. Figure 3.3 illustrates the liquidus surface for the Co-Cr-Ta ternary system calculated using the Calphad method. The figure displays the distribution of primary fields over the composition space and the isotherms of the melting temperature drawn every 20°C. The alloys under study are situated on distinct liquidus surfaces that converge to create a ternary eutectic valley. The melting temperatures increase along the composition line 1-4, then decrease from CoCrTa-4 to CoCrTa-5 and remain almost constant from CoCrTa-5 to CoCrTa-7. The ternary phase diagram highlights the existence of a deep ternary eutectic valley. To optimize the oxidation resistance at 1200°C, it is practical to move away from the valley towards the Co-Cr binary region when designing the composition of Co-Cr-Ta alloys.
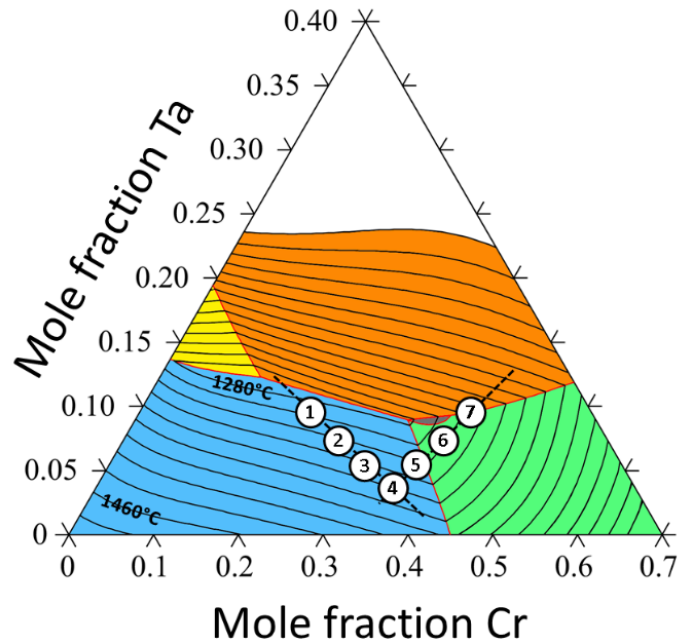
Figure 3.3. Calculated liquidus surface of the Co-Cr-Ta ternary system showing the projection of the monovariant lines and the isothermal surface every 20 °C. The prepared alloys are shown by numbers surrounded by circles [84]. Figure 3.3 is adapted from the figure in the journal of alloys and compounds, vol. 936, year 2023, 167968, by Moreau Louis Etienne, Gorsse Stéphane, Lambard Guillaume, Murakami Hideyuki.

Through this study, it was confirmed that the increased content of Cr in the alloys drastically improves the oxidation resistance as well as the solidus temperatures, as shown in Fig. 3.2(b). However, the observation of the samples after oxidation, presented in Fig. 3.1, showed that the simultaneous increase of Cr and Ta also helps the formation of a protective $CrTaO_4$ oxide layer, leading to a reduced number of pores.

Lo et al. reported good oxidation resistance of alloys up to 1000°C and 1100°C for 200 hours due to the formation of $CrTaO_4$ [86]. Gorr et al. demonstrated the potential of $CrTaO_4$ for improving the oxidation resistance of refractory high entropy alloys at temperatures ranging from 1200°C to 1500°C [87. 88]. The present study confirmed the beneficial effect of $CrTaO_4$ as an oxidation resistant layer up to 1200 °C. It is necessary to understand the impact of Cr and Ta contents on the formation of $CrTaO_4$ and the stability of Cr_2O_3 at higher temperatures

3.1.3. Prediction of Co – Cr – Ta compositions via data-driven design

To improve the oxidation resistance of a Co-Cr-Ta composition, a data-driven strategy was employed by coupling machine learning with Bayesian optimization. Eight random forest models[89] were trained using a leave-one-out cross-validation procedure [90] to predict the mass gain (g.cm^{-2}) after 20 h of oxidation at 1200 °C, called here "mg$_{20h}$", s referred to as ' mg$_{20h}$ ', based solely on the compositional ratios $\{\alpha, \beta, \gamma\}$ of Co$_\alpha$Cr$_\beta$Ta$_\gamma$. A mg$_{20h}$ of an alloy with composition Co$_\alpha$Cr$_\beta$Ta$_\gamma$ is predicted by averaging the predictions from 8 distinct RF models. These models form the interpolative surrogate model S1, which approximates the objective function mg$_{20h}$ = F(α, β, γ). S1 enables quick prediction of mg$_{20h}$ for a new composition $\{\alpha,\beta,\gamma\}$ within the bounds of the compositions, which were already assessed and presented in the former sections. To avoid inherent unintended compositional biases that may occur during the preparation of the initial dataset, S1 relaxes the pre-initialization step of the following Bayesian optimization. A synthetic dataset is created by randomly sampling S1 from $\{\alpha, \beta, \gamma\}$. To achieve this, a synthetic dataset is created by randomly sampling S1 from $\{\alpha,\beta,\gamma\}$. In this study, n$_{rand}$was fixed at 1000 random samples of $\{\{\alpha, \beta, \gamma\},\ mg_{20h}\}$, representing the square root of the million possible compositions at 1wt% resolution within the selected range of compositions for investigation. Next, a Gaussian process regressor is used as a surrogate model (S2) to approximate the objective function (F) on the entire domain of possible compositions $\{\alpha, \beta, \gamma\}$. This is achieved by defining a prior over functions that can fit the synthetic dataset and extrapolate beyond the pre-existing domain of knowledge. S2 can propose novel compositions likely to maximize mg$_{20h}$ by maximizing the expected improvement (EI) [91]., which is chosen as the acquisition function. The acquisition function enables a balance between exploiting and exploring the composition space by suggesting samples that have the potential to match the global maxima in mg$_{20h}$, based on the expected value and uncertainty predicted from S2. The

The RF models were trained and Bayesian optimization was performed using the Python packages Scikit-learn [92] and GPyOpt [93], respectively. The methods used were *RandomForestRegressor* and *BayesianOptimization* with standard input parameters, without any further fine-tuning. A list of proposals was generated, and the top 5 were selected for experimental feedback. The schematic representation of this method is shown in Fig. 3.4.
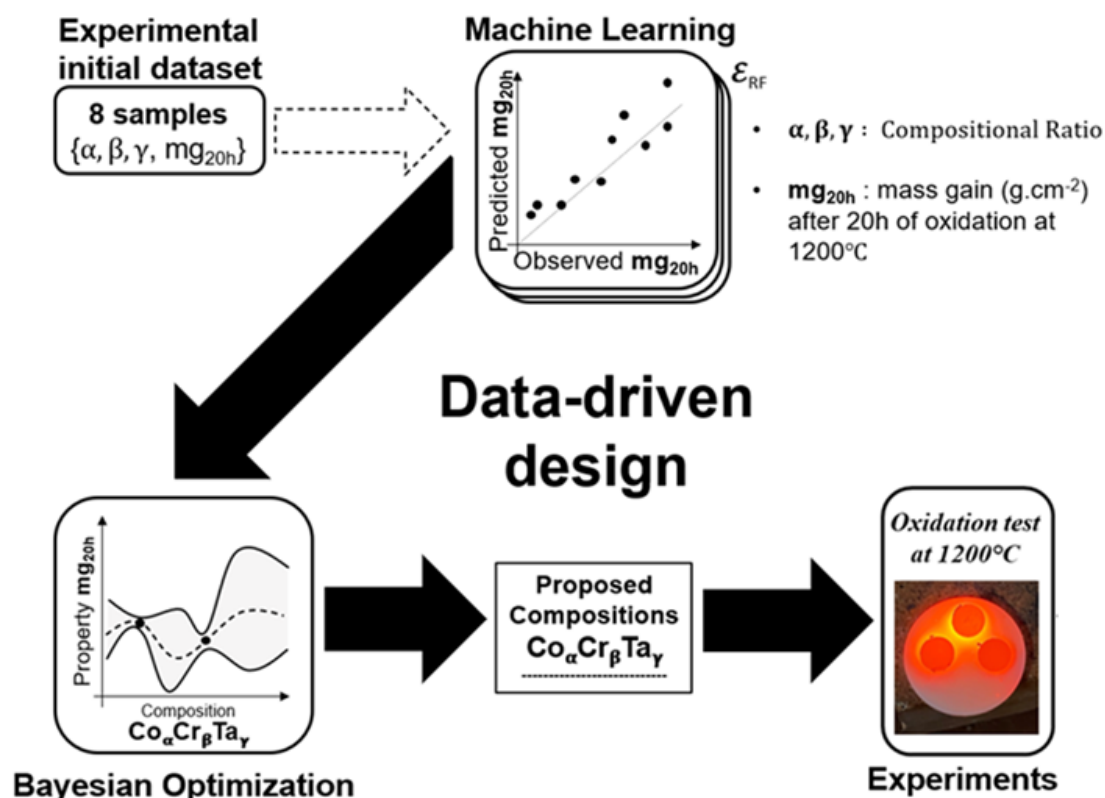

Figure 3.4. Data driven strategy using Bayesian optimization for the prediction of Co-Cr-Ta composition with good oxidation resistance at 1200 °C [84]. Figure 3.4 is adapted from the figure in the journal of alloys and compounds, vol. 936, year 2023, 167968, by Moreau Louis Etienne, Gorsse Stéphane, Lambard Guillaume, Murakami Hideyuki.

Then two of them were characterized to survey the precision of the data-driven method, of which the compositions are listed in Table 3.2. The estimated specific mass gain after 20 h of exposure predicted by the machine learning are presented in Fig. 3.5(a) by the dotted line. It can be noticed that the predicted compositions in the figure contain important amount of Cr, corresponding to the previous results (Fig. 3.2(b)) and showing an important role of Cr content

in specific mass change. However, the Ta content proposed is lower than any of the Co – Cr –

Ta compositions tested earlier.

Table 3.2. Predicted compositions of Co-Cr-Ta using machine learning and Bayesian optimisation method [84]. Table 3.2 is adapted from the table in the journal of alloys and compounds, vol. 936, year 2023, 167968, by Moreau Louis Etienne, Gorsse Stéphane, Lambard Guillaume, Murakami Hideyuki.

Alloy	Co (at.%)	Cr (at.%)	Ta (at.%)
CoCrTa-8	65.3	33.7	1
CoCrTa-9	63.6	35	1.4

To examine the microstructure of oxidized CoCrTa-8 and -9 predicted by the machine

learning, an oxidation test at 1200 °C for 20 h in air was carried-out for these alloys and the

measured mass change is shown in Fig. 3.5(b). It should be noted that the mass change measured

after the oxidation test (Fig. 3.5(b)) does not take in consideration spalled oxides, unlike that

from the TGA (Fig. 3.2(b) and Fig. 3.5(a)), but it is still observed in Fig. 3.5(b) that CoCrTa-8

and -9 have the lowest mass change of all tested composition, going with the target chosen for

the machine learning predictions. The microstructure of these samples after oxidation are

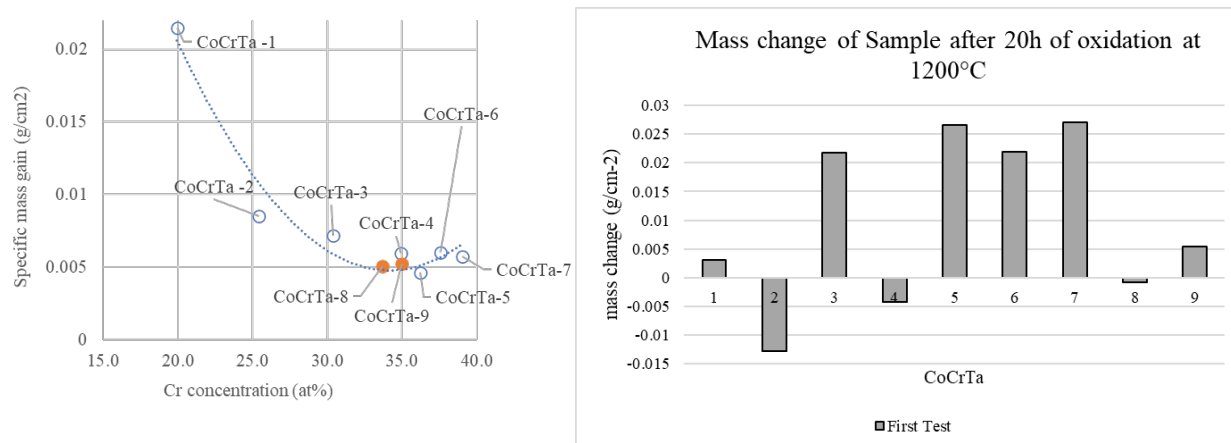characterized using BSE and EDS and are visible in Fig. 3.6. Like previous results, formation

Figure 3.5. (a) Estimated specific mass gain of predicted composition after oxidation for 20 h at 1200 °C as a function of Cr and (b) measured mass change after oxidation test for 20 h at 1200 °C in air.
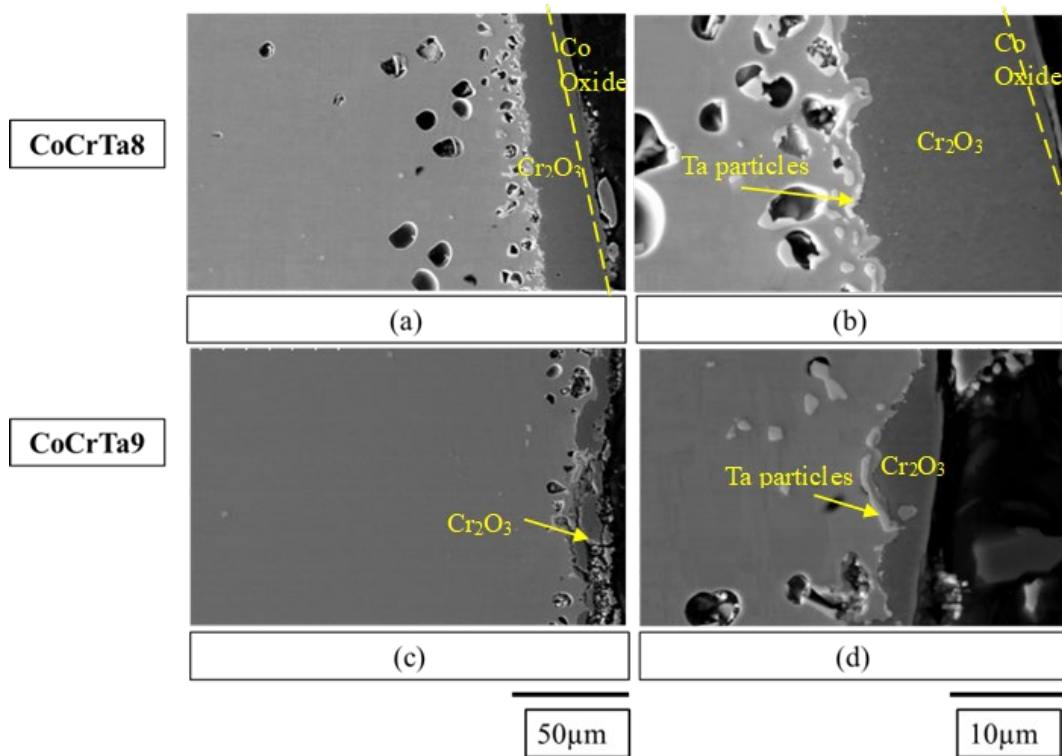
Figure 3.6. BSE images of predicted Co-Cr-Ta alloys after oxidation for 20 h at 1200 °C in air [84]. Figure 3.6 is adapted from the figure in the journal of alloys and compounds, vol. 936, year 2023, 167968, by Moreau Louis Etienne, Gorsse Stéphane, Lambard Guillaume, Murakami Hideyuki.

of external Cr_2O_3 was observed but is shattered for CoCrTa-9 in Fig. 3.6(c), and Co rich oxide was detected on the top. In these alloys (Figs. 3.6(b) and (d)), only Ta and Cr rich particles form at the interface metal/oxide, instead of the formation of a continuous $CrTaO_4$ layer. The main difference between these two samples is the presence of numerous pores in CoCrTa-8 adjacent to the interface metal/oxide, and even larger pores present deeper in the alloy. The development of CoCrTa-8 and 9 in this study indicates the effectiveness of the data-driven algorithm for alloy design, as demonstrated in Fig. 3.5. However, when evaluating the oxidation resistance of materials, it is important to consider not only mass change but also microstructural stability. This includes factors such as void formation in the substrate, adherence, and uniformity of oxides formed on the surface, as shown in Figure 3.6. Further improvements in computer-aided material design are needed.

3.2. Oxidation for 100 h at 1200 °C by TGA

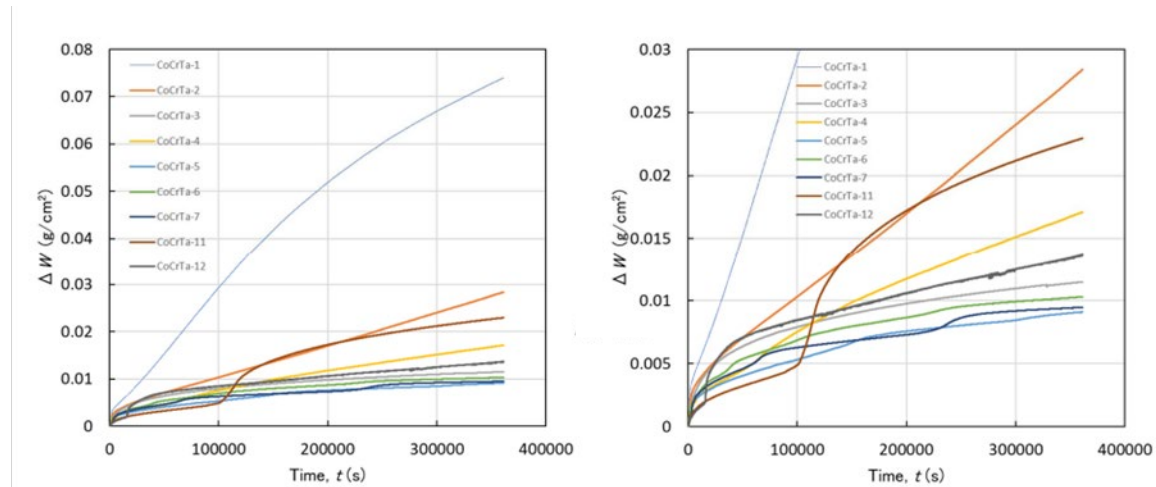## 3.2.1. Mass change and microstructure after oxidation

Figure 3.7 (a) Mass gain and (b) parabolic rate constant of Co-Cr-Ta alloys as a function of oxidation time at 1200 °C.

Figure 3.7 represents the oxidation kinetics of Co-Cr-Ta alloys, plotting the mass change and parabolic rate constant (Kp) against oxidation time. The parabolic rate constant is determined using the formula $(\Delta m/ S)^2 = Kp\ t$, where Δm is the mass change, S is the surface area, and t is the time. The graph illustrates variations in the alloys' resistance to oxidation, showing a higher rate of mass gain for certain alloys, indicative of less resistance to high-temperature oxidation.

Figure 3.8 shows the BSE image of various Co-Cr-Ta alloys after oxidation for 100 h at 1200 °C by TGA. Each alloy exhibits unique characteristics in terms of oxidation:

- **CoCrTa-1:** Shows extensive internal oxidation.

- **CoCrTa-2:** Exhibits significant internal oxidation like CoCrTa-2.

- **CoCrTa-3:** Reveals isolated formations of $CrTaO_4$, indicating a less effective protective layer.

- **CoCrTa-4**: Displays a less developed $CrTaO_4$ inclusion pattern, raising concerns about its long-term resistance.

- **CoCrTa-5:** Exhibits a clear presence of $CrTaO_4$, suggesting a better protective capability.

- **CoCrTa-6:** Features a robust oxide layer with well-defined $CrTaO_4$ regions, indicative of superior oxidation resistance.

- **CoCrTa-7:** Features a robust oxide layer with well-defined $CrTaO_4$ regions, indicative of superior oxidation resistance like CoCrTa-6.

Consequently, the observations from Figs. 3.7 and 3.8 clearly demonstrate a correlation between the formation of $CrTaO_4$ and the oxidation resistance of Co-Cr-Ta alloys. Alloys with a pronounced formation of $CrTaO_4$, as seen in Fig. 3.8, exhibited a slower rate of oxidation in Fig. 3.7. This suggests that the presence of $CrTaO_4$ enhances the alloys' ability to withstand high-temperature environments, making it a key factor in their improved oxidation resistance.
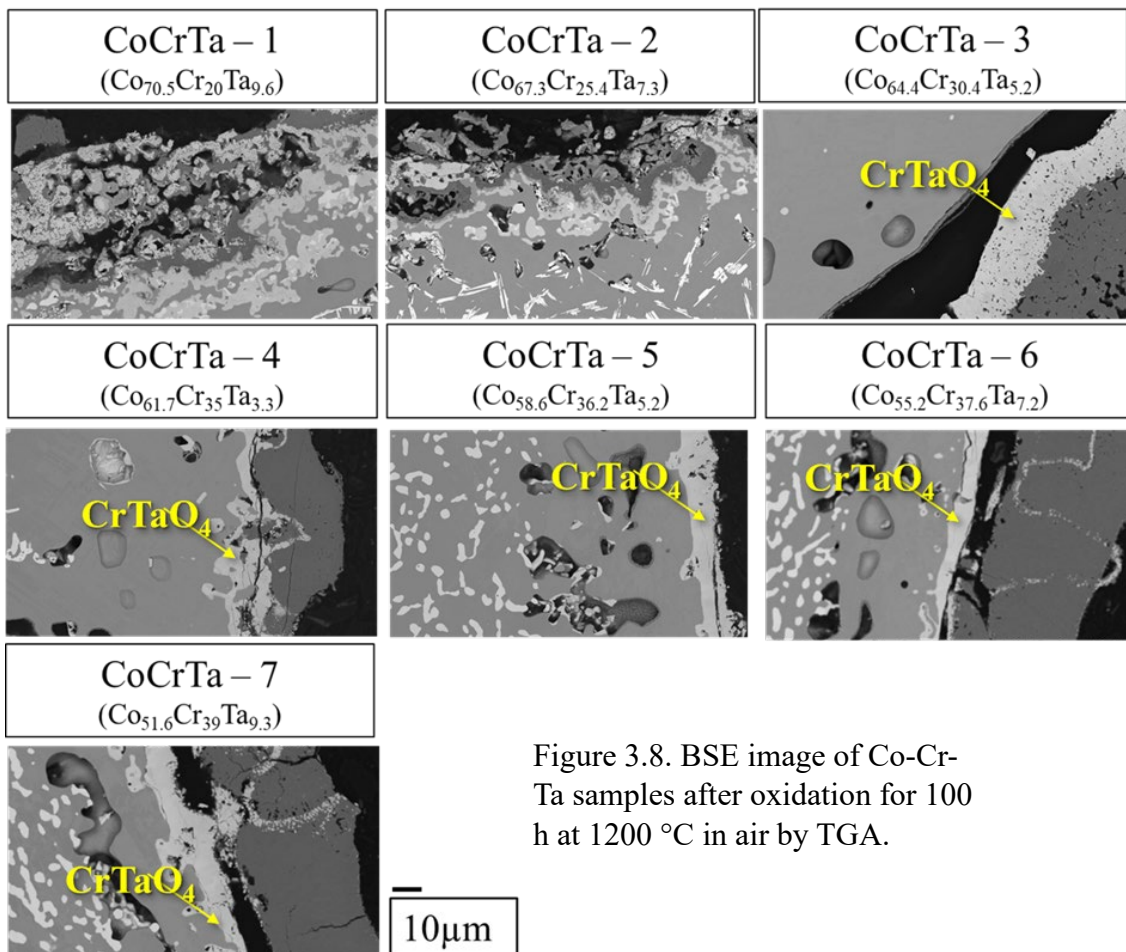

Figure 3.8. BSE image of Co-Cr-Ta samples after oxidation for 100 h at 1200 °C in air by TGA.

3.2.2. Beneficial effect of CrTaO₄ formation on oxidation resistance

Figure 3.9 delineates the oxidative response of two CoCrTa alloy compositions: CoCrTa-1 and -7, after thermal exposure at 1200 °C in air for 20 and 100 h. The micrographs provide the following stark visual contrasts between the oxidation behaviors of the two alloys.

- **CoCrTa-1:**
  - **After 20 hours:** The microstructure reveals significant porosity. This onset of porosity suggests a poor oxidation resistance, with the formation of non-protective sufficient oxides that in turn detach from the substrate, indicative of spallation. The presence of internal oxidation is also noted, suggesting the penetration of oxygen into the substrate, which exacerbates the degradation of the material.
  - **After 100 hours:** The alloy's condition has visibly deteriorated, displaying numerous oxide formation and severe internal oxide formation with a larger number of pores, with
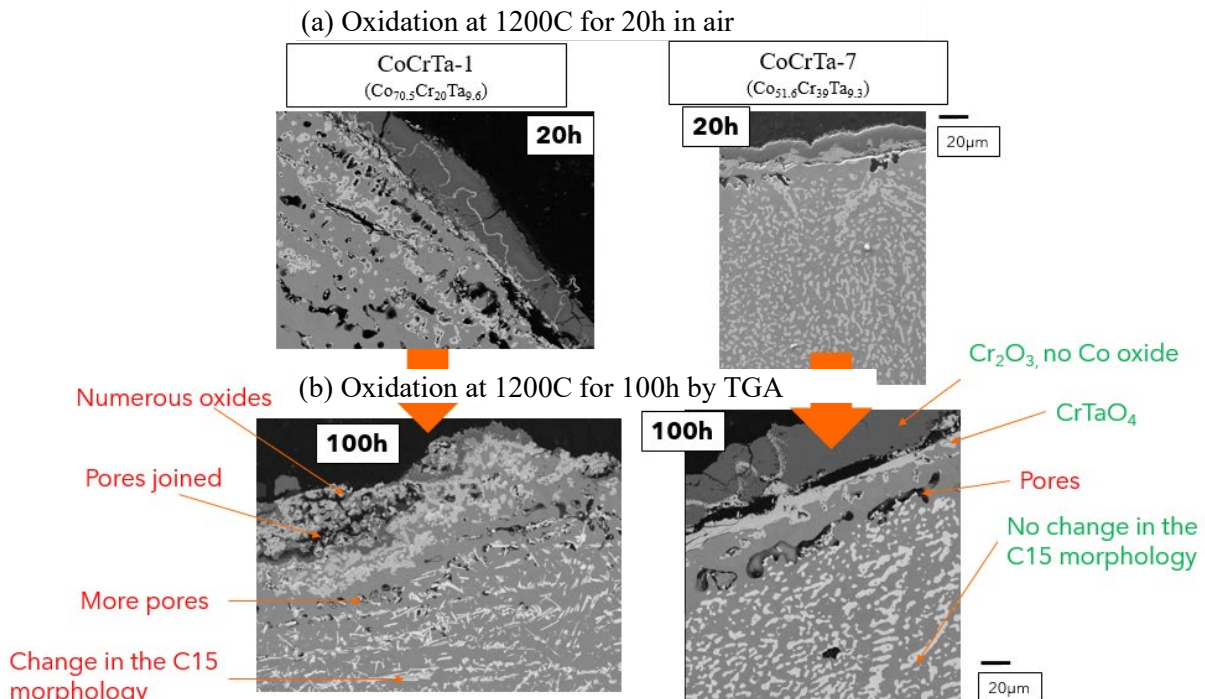

Figure 3.9. BSE image of CoCrTa-1 and 7 samples after oxidation for 20 h and 100 h at 1200 °C in air.

the porosity coalescing into larger voids. Additionally, a change in the C15 morphology signals further degradation of the material's microstructure.

- **CoCrTa-7:**
  - **After 20 hours:** The micrograph shows a more resilient microstructure with fewer pores, suggesting more stable oxide formation and better adherence to the substrate, and characteristics of a protective oxide scale. Moreover, this sample already shows the formation of $CrTaO_4$ after 20 h of oxidation at 1200 °C in air.
  - **After 100 hours:** The microstructure of CoCrTa-7 maintains a comparative integrity with no visible change in the C15 Laves phase morphology, reinforcing the notion of superior oxidation resistance. The presence of Cr_2O_3 and no visible Co oxide points towards the selective formation of a protective chromium oxide layer and a retarded outward diffusion of elements such as Co, as described earlier. This is further confirmed by reduced number of pores in the substrate compared to CoCrTa-1. Finally, the formation of $CrTaO_4$ is clearly visible and continuous, indicating a stable oxide that contributes to the alloy's defense against oxidative stress.

3.3. Cyclic oxidation at 1200 °C in air

3.3.1. Mass change and microstructure after oxidation

In order to further prove the beneficial effects of the formation of $CrTaO_4$ on the Co-Cr-Ta samples, a cyclic oxidation test was performed. Oxidation for 1 h at 1200 °C followed by air quenching was repeated 20 times and the mass change was measured for the 5 first cycles and 5 last cycles and presented in Fig. 3.10.

The graph provides a comparative analysis of the oxidation resistance of the Co-Cr-Ta alloys. Alloys that exhibit a less negative Δm over a greater number of cycles, such as CoCrTa-7, are interpreted to have better oxidation resistance. This resistance could be attributed to the
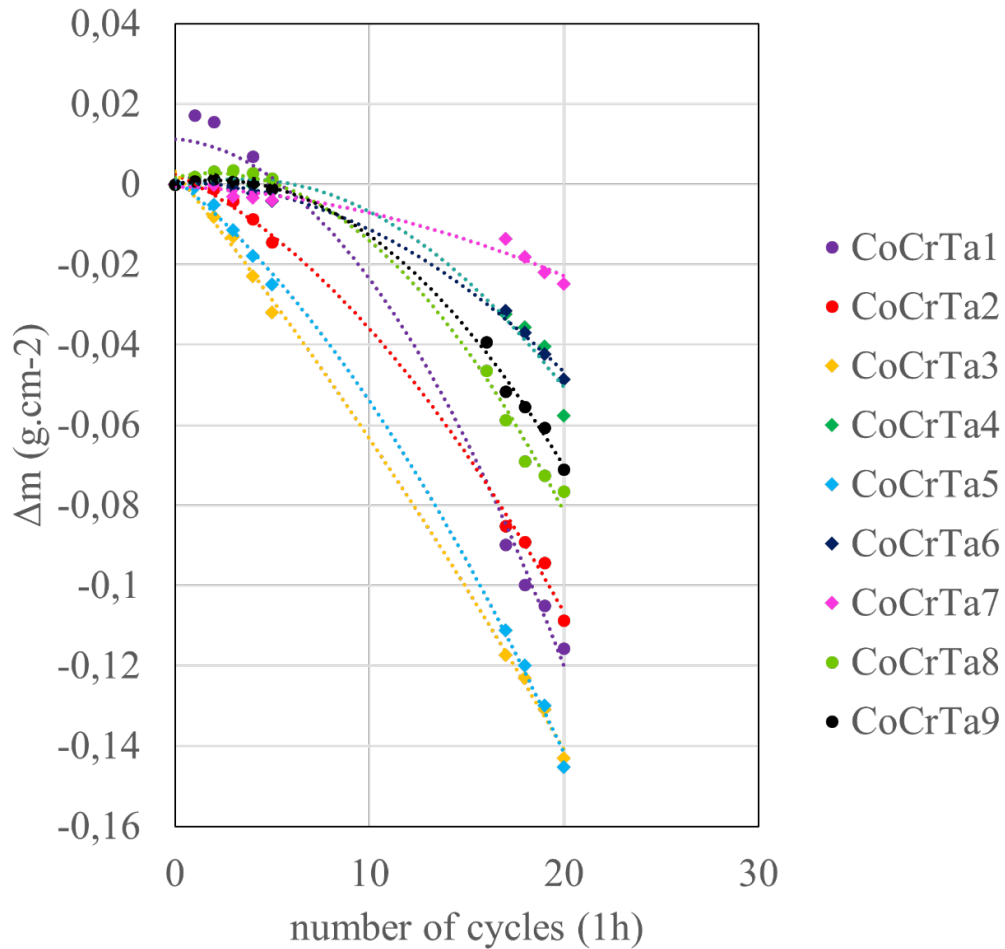
Figure 3.10. Mass gain during 20 one-hour cyclic oxidation at 1200 °C in air.

formation of a more robust oxide layer that adheres well to the alloy, thus offering sustained protection. In contrast, alloys like CoCrTa-3, which lose mass more quickly, may have a less effective oxide layer, which could compromise the material's structural integrity over time.

The downward trends observed over the time after repeated cycles suggest that spallation is a likely mechanism of degradation for these materials. Spallation occurs when the oxide layer formed during high-temperature exposure does not adhere well to the substrate and flakes off, resulting in a loss of mass. Alloys with a steeper mass loss trend, such as CoCrTa-3, may experience more frequent or more severe spallation events. This not only removes the protective oxide layer but also exposes fresh material underneath the oxide layer to the environment, which can perpetuate the cycle of spallation.

Figure 3.11. BSE image of Co-Cr-Ta samples after 20 one-hour cycles at 1200 °C in air.
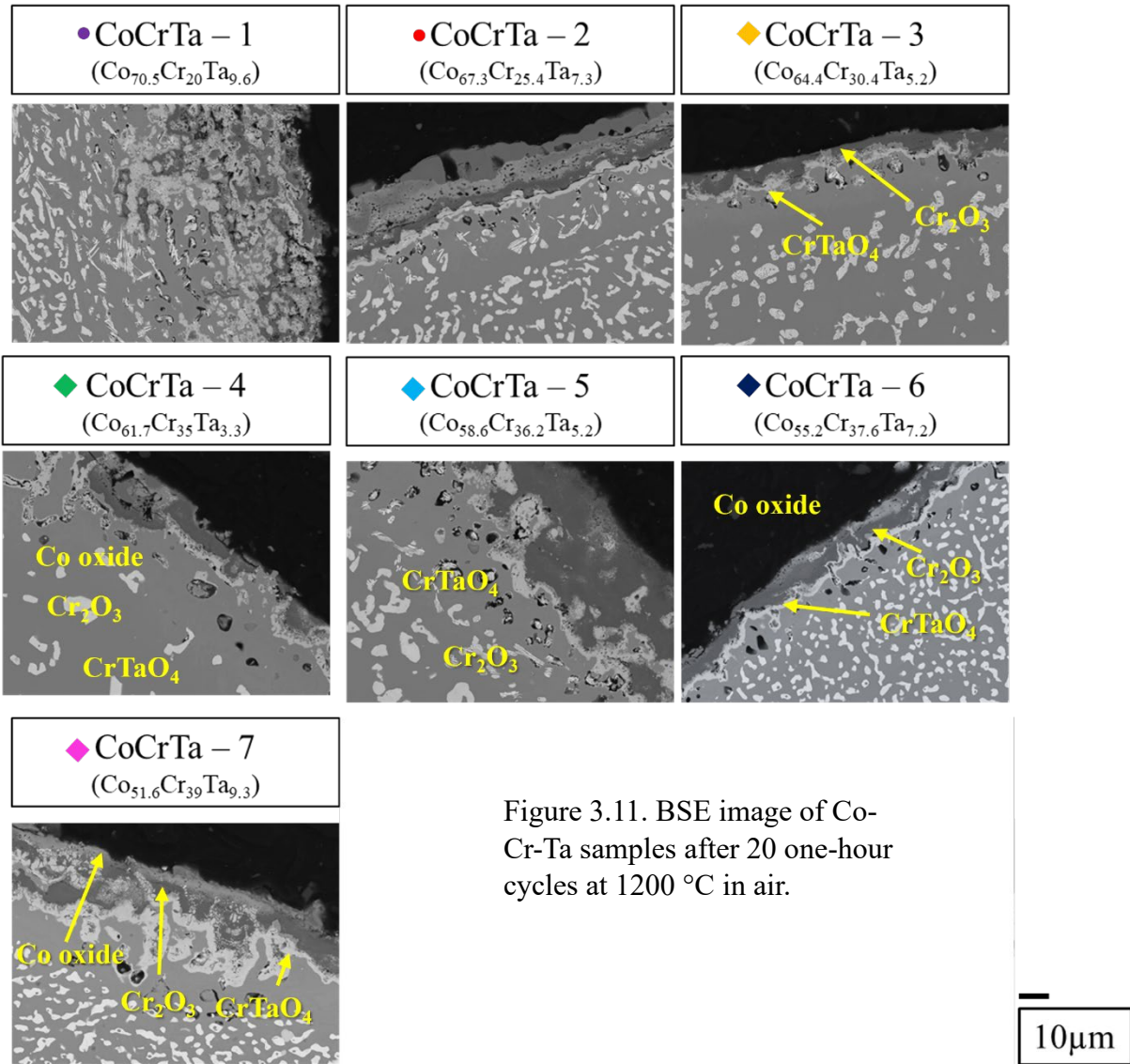
Figure 3.11 shows the cross section of the samples after 20 one-hour cycles. In this figure, CoCrTa-1 displays extensive oxidation with blurred phase boundaries, indicative of substantial alloy-environment interaction, possibly leading to a thickened oxide layer with potential spallation regions. On the other hand, CoCrTa-2 shows the formation of several porous oxide layers. In addition, the microstructure of this alloy, in particular, the C15 Laves phases seems to have reacted during the oxidation process. CoCrTa-3 features a thin but continuous layer of $CrTaO_4$, interspersed with Cr_2O_3. Referring to its rapid mass loss during cyclic oxidation in Fig. 3.10, this could indicate much spallation of the oxides formed on this alloy, showing an unprotected oxide layer. CoCrTa-4 exhibits heterogeneous oxide formation with

visible patches of Co oxide, Cr_2O_3, and localized $CrTaO_4$. The presence of diverse oxides may affect the protective efficacy of the oxide scale against further oxidation. This behavior is similar to the microstructure observed in CoCrTa-5. However, the rapid mass loss pictured in Fig. 3.10 is very surprising. This could indicate that this sample faced a large amount of oxide formation and spallation leading to a rapid loss of an element such as Cr, reducing the protective properties of this alloy. CoCrTa-6 portrays a combination of well-defined $CrTaO_4$ and stable and thin Cr_2O_3 phases, suggesting a robust and uniform oxidation process that may provide a stable protective barrier. However, the presence of Co oxide is concerned as this oxide is very volatile at this temperature, indicative of the outward diffusion of Co to the atmosphere. Finally, CoCrTa-7 have a similar microstructure than CoCrTa-6 with a thicker layer of $CrTaO_4$ but with the stable formation of both this oxide and Cr_2O_3. However, again, the presence of Co oxide could be concerned as this oxide is known to be volatile and unstable at this temperature.

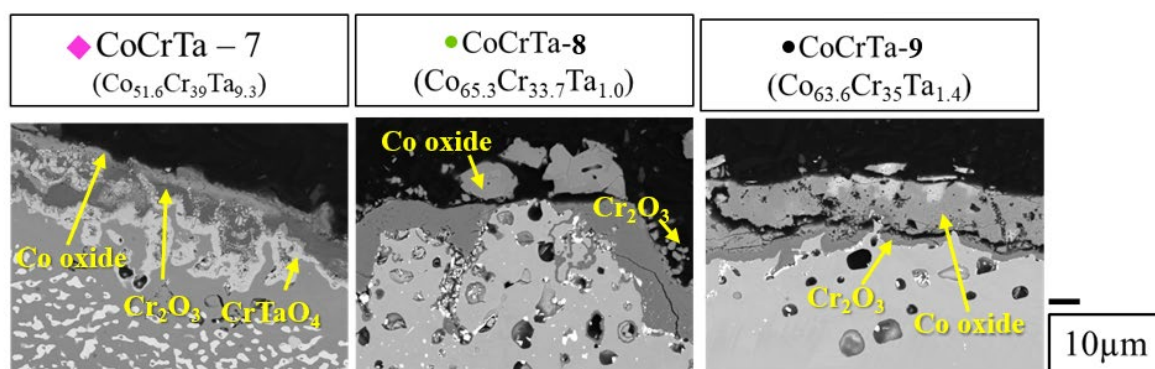### 3.3.2. Machine learning composition for cyclic oxidation

Figure 3.12. BSE image of CoCrTa-7. 8. and 9 samples after 20 one-hour cycles at 1200 °C in air.

In Section 3.1.3, CoCrTa-8 and -9 were predicted as Co-Cr-Ta alloys with good oxidation resistance by machine learning and examined by oxidation test for 20 h at 1200 °C in air. In this section, these alloys were tested for cyclic oxidation of 20 one-hour cycles at 1200°C in air. Figure. 3.12 shows the microstructures after the cyclic oxidation test. As shown in this figure, the machine learning compositions of CoCrTa-8 and CoCrTa-9 exhibited no formation
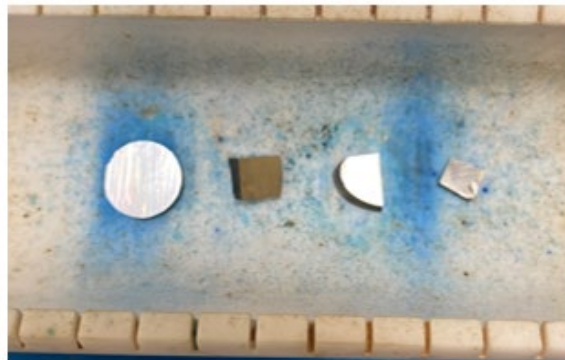
of CrTaO$_4$, leading to poor oxidation resistance and pore formation. From these results, the beneficial aspect of CrTaO$_4$ formation is again pointed out, as discussed in Section 3.2.2.

3.3.3. Outward diffusion of elements during oxidation

Figure 3.13 shows the appearance of the Co-Cr-Ta samples after the cyclic oxidation test. The top picture exhibits the appearance of four metal samples arranged on a refractory shelf before test. The samples display various geometries: one circular, one square, and two semicircular pieces, each exhibiting a clean and reflective surface indicative of an unoxidized state.

The bottom picture, labeled 'After 20 cycles of 1h oxidation at 1200 °C in air,' captures the aftermath of the oxidation test. Notable is the alteration on the sample surfaces; they were

Figure 3.13. Appearance of samples after 20 one-hour cycles at 1200 °C in air.

once lustrous, and now exhibit a matte finish with a conspicuous blue tint surrounding the specimens. This colouration is characteristic of cobalt oxide formation, implying the outward diffusion of cobalt elements from the samples.

Moreover, a dark powder is observed to be dispersed over the refractory shelf and on the samples. This detritus is consistent with the morphology of spalled oxides, potentially comprising chromium (III) oxide (Cr_2O_3) or cobalt oxides, a byproduct of the substantial spallation process. The spallation is indicative of the disintegration of the protective oxide layers that had formed on the samples' surfaces during the high-temperature exposure.

This comparative analysis elucidates the oxidative degradation mechanisms experienced by the metal alloys and underscores the spallation propensity under cyclic thermal stress. The visual evidence of degradation corroborates the thermogravimetric data shown in Fig. 3.10, providing a holistic understanding of the material's behavior in an oxidative environment.

In parallel to the microstructure observed in Figs. 3.11 and 3.12, the internal oxidation and spallation of oxides can be easily understood by looking at these two pictures in Fig. 3.13. However, the more protected microstructure of samples such as CoCrTa-6 and CoCrTa-7 are seen in Fig. 3.11, with the presence of Co Oxide still attached to the samples, which implies that those samples have a retarded outward diffusion of elements such as Co. This leads to the hypothesis that the formation of $CrTaO_4$ not only improves the protection of the samples against external oxidation but also slows down the outward diffusion of elements during oxidation.

3.4. Oxidation at 1300 °C in air

In the practical application of a spinner within the glass fiber manufacturing process at a temperature of 1200 °C, the thermal stability faces potential fluctuations of ±50 °C. To

proactively address issues arising from these temperature variations, an assessment of oxidation resistance was conducted under more extreme conditions at 1300 °C exceeding the initial target. This study was undertaken with the focus on two key aspects: firstly, understanding the substantial benefits of $CrTaO_4$ formation for oxidation resistance at 1200 °C, and secondly, verifying the persistence of this effect at 1300 °C. Within the context of glass fiber manufacturing, a temperature elevation presents ecological advantages by expediting the fusion of diverse materials constituting the fibers, consequently reducing processing time and associated energy consumption. Oxidation tests at 1300 °C were specifically directed at CoCrTa-1 to 4 compositions that revealed slightly lower oxidation resistance at 1200 °C compared to other compositions, along with CoCrTa-6 and CoCrTa-8 that were identified as alloys with good oxidation resistance by a machine learning approach. The SEM micrographs presented in Fig. 3.14 accentuated crucial trends, confirming the pivotal influence of Ta in the
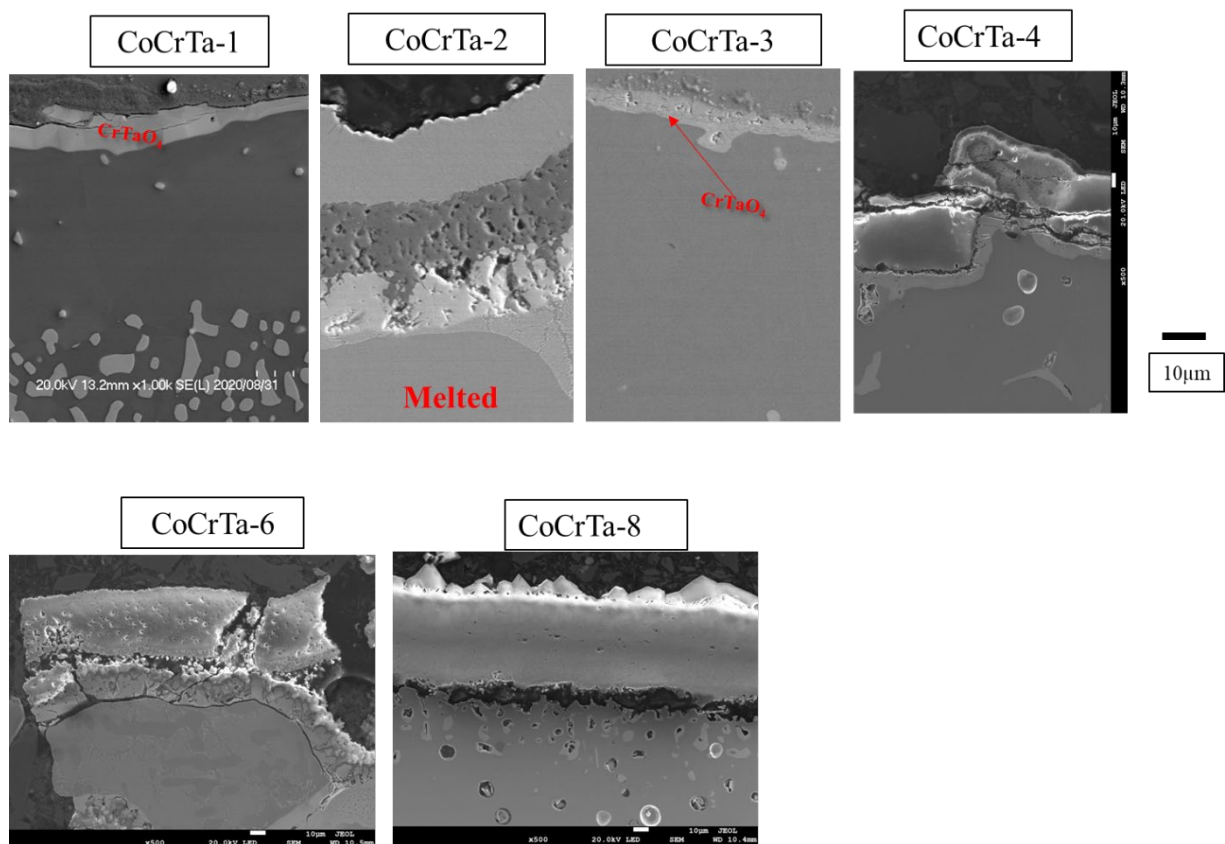

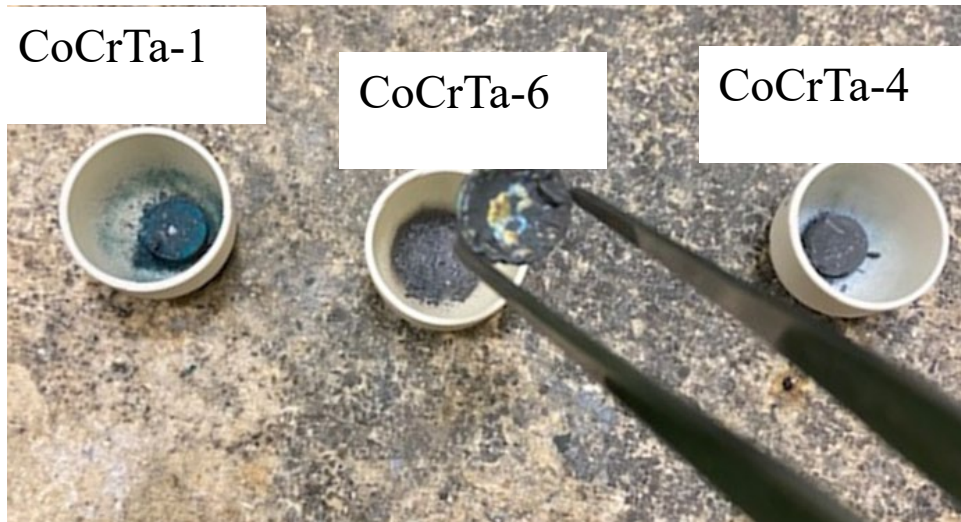Figure 3.14. Microstucture of CoCrTa alloys after oxidation test for 20 h at 1300 °C in air.

Figure 3.15. Appearance of CoCrTa samples after oxidation test for 20 h at 1300 °C in air.

alloy for $CrTaO_4$ protective oxide formation. Detailed observations indicated that certain alloys, despite of effective protection against oxidation at 1200 °C due to $CrTaO_4$, melted at 1300 °C, highlighting practical limitations associated with their proximity to the 1350 °C melting point. These findings, aligned with CALPHAD predictions made during the selection of the ternary alloy family (Fig. 3.3), are confirmed through the photographs showcased in Fig. 3.15.

In Fig. 3.16 (reproduced from Fig. 3.3), the influential role of chromium in elevating the melting temperature of CoCrTa compositions is conspicuous. Notably, a discernible trend emerges, revealing that beyond a molar fraction of 0.4 for chromium, there is a lack of substantial augmentation in the melting temperature, thereby stabilizing it at approximately 1320°C. Consequently, within the ambit of optimizing composition to enhance the melting temperature, there emerges limited practical utility in augmenting the chromium content. Furthermore, this empirical insight provides a plausible rationale for the observed melting phenomena in samples CoCrTa-2 and CoCrTa-6 during the 1300°C trial. Intriguingly, the resilience of CoCrTa-1 under the same conditions adds a nuanced layer of complexity to our understanding of the alloy's behavior under extreme thermal conditions.
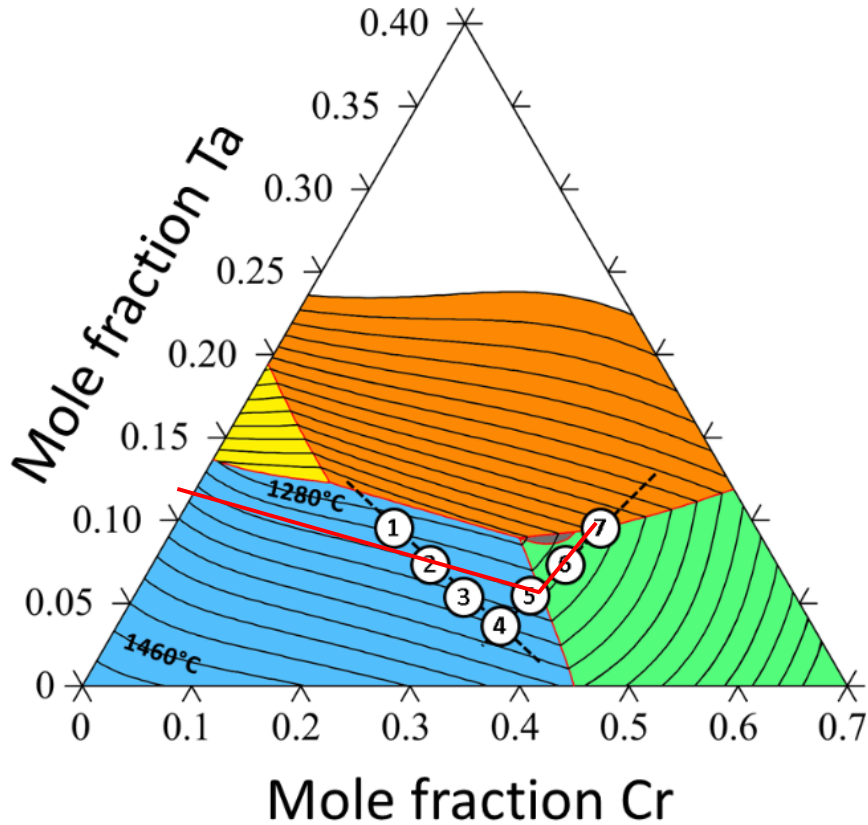
Figure 3.16. Calculated liquidus surface of the Co-Cr-Ta ternary system via CALPHAD, liquidus line every 20°C(reproduced from Fig. 3.3) [84]. Figure 3.16 is adapted from the figure in the journal of alloys and compounds, vol. 936, year 2023, 167968, by Moreau Louis Etienne, Gorsse Stéphane, Lambard Guillaume, Murakami Hideyuki.

3.5. Corrosion at 1200 °C in glass

In the introductory section, it was posited that the alloys under development primarily serve the optimisation of materials employed in the production of plates for glass fiber spinning. Despite the identification of alloys resistant to oxidation at elevated temperatures, primarily attributable to the formation of a protective $CrTaO_4$ oxide, it is imperative to explore additional facets of these alloys' resistance, particularly concerning direct contact with molten glass within the glass fiber manufacturing process.

Initiating with a static immersion test, where the alloy is immersed in non-agitated molten glass, this preliminary assessment provides insights into potential resistance to direct

molten glass exposure, albeit without perfect replication of real-world dynamic conditions. Promising outcomes may prompt the submission of samples to Saint-Gobain for dynamic testing in a molten glass bath, replicating operational realities.

To simulate a more realistic interaction, samples of glass fibers, derived from the sought-after manufacturing process, were acquired from Saint-Gobain. Deposition onto alloy specimens within an alumina crucible, as depicted in Fig. 3.17, served to emulate real-world conditions. Post-corrosion observations were intricate due to glass fragility, necessitating epoxy immersion, longitudinal sectioning, and subsequent epoxy immersion for meticulous polishing aimed at safeguarding the formed glass layer.
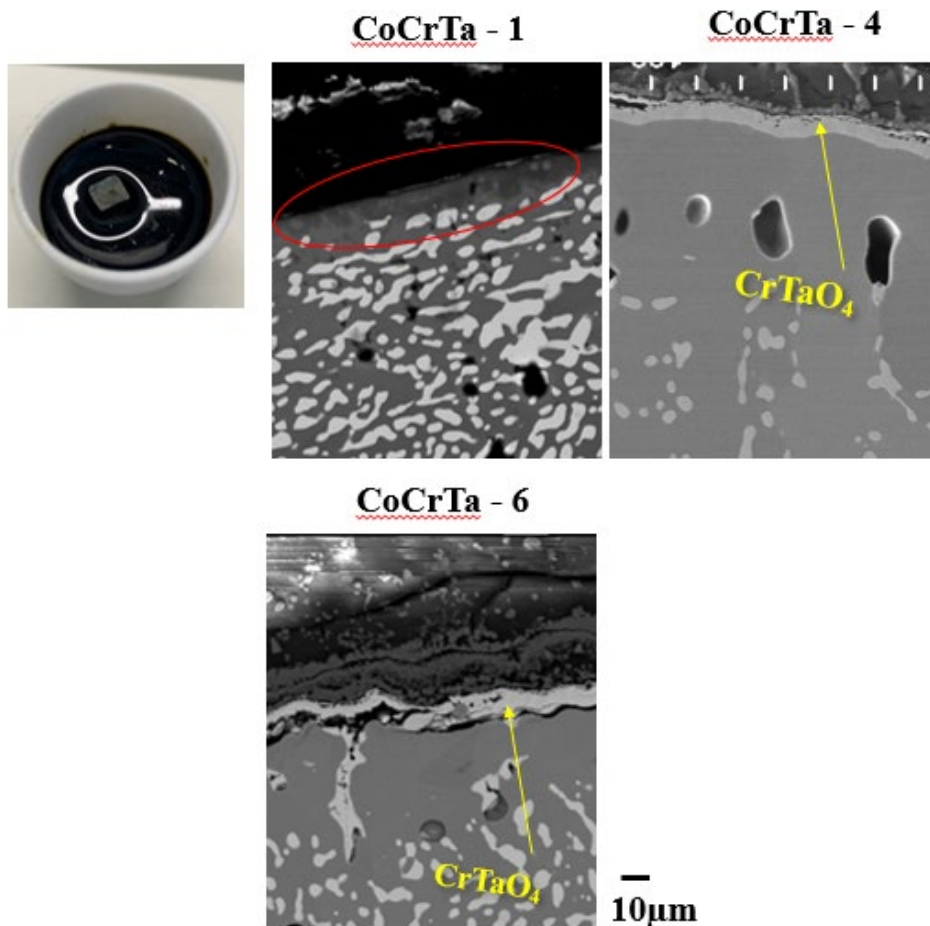

Figure 3.17. The cross-sectional microstructure of CoCrTa compositions after corrosion test in glass for 20 h at 1200 °C.

SEM micrographs after the corrosion in glass at 1200 °C, presented in Fig. 3.18, unveil that CoCrTa-1 composition failed to yield the protective oxide $CrTaO_4$, resulting in an undesirable reaction at the glass/metal interface. Conversely, CoCrTa-4 and CoCrTa-6 compositions exhibit a continuous and stable formation of $CrTaO_4$ oxide, devoid of substrate-glass reactivity. These outcomes are particularly encouraging for compositions yielding $CrTaO4$, indicating a beneficial effect even against molten glass-induced corrosion. In addition to the SEM observation, an EDX analysis of CoCrTa-4 alloy was performed to substantiate the absence of glass within the metallic matrix and presented in Fig. 3.18.
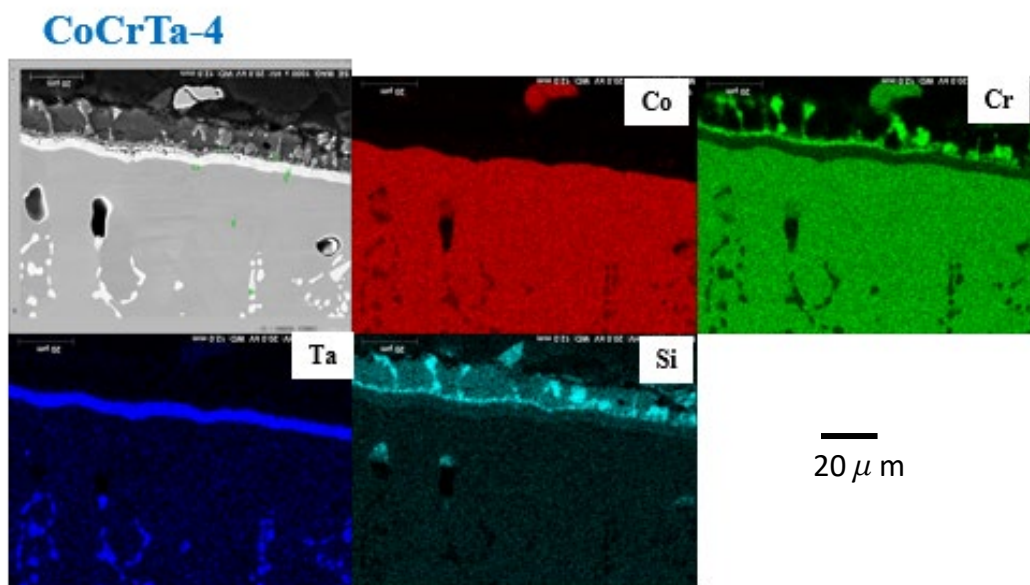

Figure 3.18. EDX analysis of CoCrTa-4 after corrosion test in molten glass for 20 h at 1200 °C.

This figure conclusively validates the presence of a stable and continuous $CrTaO_4$ layer after the corrosion at 1200 °C in molten glass. Equally noteworthy is the confirmed absence of silicon within the alloy matrix, substantiating the alloy's efficacy in preventing molten glass penetration. This observation underscores a significant benefit derived from the $CrTaO_4$ formation not only in its pronounced resistance to cyclic and monotonic oxidation at 1200 °C and 1300 °C but also in its resistance to corrosion when exposed to molten glass at 1300 °C.

The conspicuous lack of silicon within the alloy matrix, as depicted in this figure, emphasizes the alloy's robust defense against molten glass infiltration. This noteworthy discovery further underscores the substantial and positive impact resulting from the consistent presence of the $CrTaO_4$ oxide. This protective effect extends beyond withstanding cyclic and monotonic oxidation at temperatures of 1200 °C and 1300 °C, encompassing resilient resistance against corrosion during exposure to molten glass at 1300 °C. The comprehensive affirmation of these findings highlights the alloy's efficacy across diverse high-temperature environments, showcasing its potential applications in glass fiber manufacturing processes.

3.6. Summary

To summarize, this comprehensive exploration into Co-Cr-Ta alloys provides understanding of their performance in extreme environments, with a particular emphasis on their remarkable resistance to high-temperature oxidation, their behavior in the face of corrosion when exposed to molten glass, and their endurance under prolonged and severe conditions. The key outcome from this study is the undeniable efficiency of these alloys, attributed to the formation of a continuous and stable $CrTaO_4$ layer.

Figure 3.19 effectively illustrates the enhancement in oxidation resistance attributed to the formation of $CrTaO_4$. This visual representation underscores the oxide's critical role in
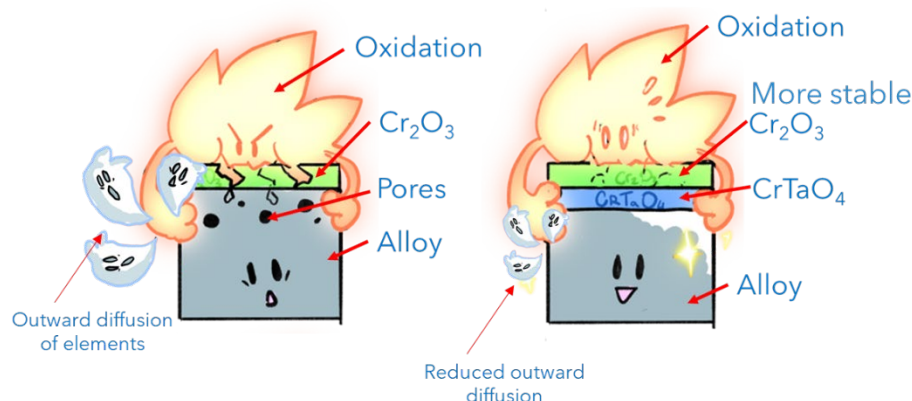

Figure 3.19. Schematization of the oxidation resistance of an Alloy improved by the formation of $CrTaO_4$.

improving the alloy's performance under oxidative conditions.

The formation of CrTaO$_4$ not only acts as a robust shield against oxidation but also proves effective in preventing corrosion, especially in demanding applications like the glass fiber manufacturing industry. Beyond the laboratory, the method employed in this study, involving meticulous analyses, detailed visualization, and innovative use of machine learning modeling, opens promising avenues for refining the composition of Co-Cr-Ta alloys, not solely for their resistance to oxidation and corrosion but also for their practical utility in real-world scenarios such as temperature fluctuations inherent in industrial manufacturing processes.

Chapter 4: Understanding the formation of CrTaO₄ for oxidation resistance of Co-Cr-Ta alloys

4.1. Theoretical framework of CrTaO₄ formation

The Co-Cr-Ta alloy system, central to this research, draws inspiration from the TATIC4 superalloy, known for its high chromium content. The primary objective of incorporating chromium is to foster the formation of Cr_2O_3, thus enhancing the alloy's oxidation resistance at elevated temperatures. Interestingly, our observations indicate that, in addition to Cr_2O_3, the ternary alloys also tend to form $CrTaO_4$. Literature [94]reported the reaction $Ta_2O_5 + Cr_2O_3 \rightarrow 2CrTaO_4$ as the source of $CrTaO_4$.
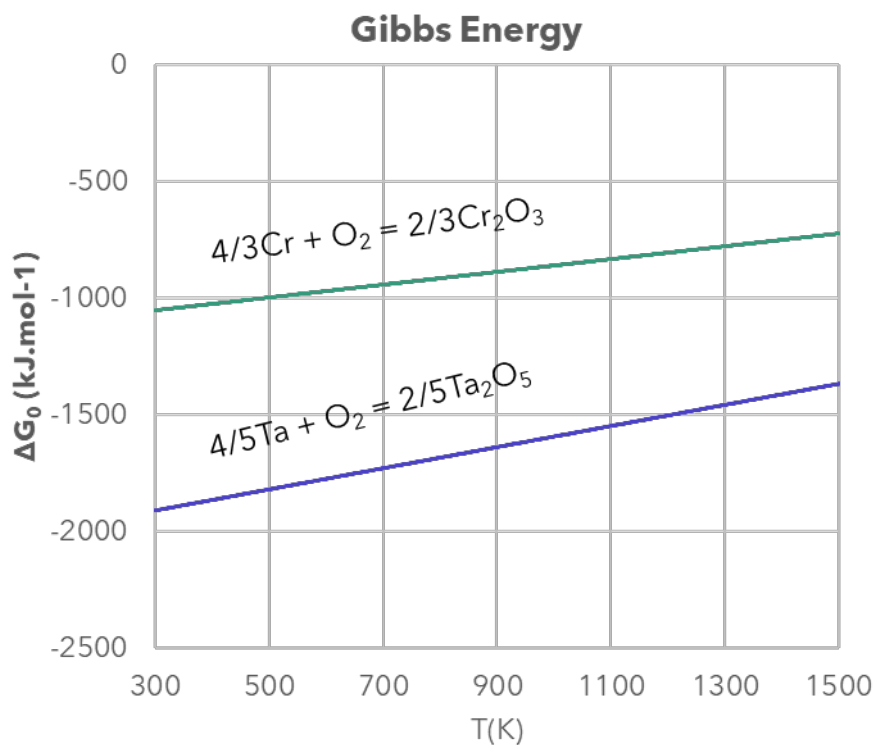

Figure 4.1. Ellingham diagram of the formation of Ta_2O_5 and Cr_2O_3.

According to the Ellingham diagram presented in Fig. 4.1 for the formation of Cr_2O_3 and Ta_2O_5, Ta_2O_5 can form at a lower oxygen pressure than Cr_2O_3. Leveraging this insight, a hypothesis for the formation of $CrTaO_4$ was formulated. The equilibrium formation energy of this oxide was calculated using the equation: $\Delta_{g0}(CrTaO_4) = 1/2\ \Delta_{g0}(Cr_2O_3) + 1/2\ \Delta_{g0}(Ta_2O_5)$, and the findings are displayed in Fig. 4.2. This calculation suggests an initial formation of Ta_2O_5, followed by the development of Cr_2O_3. The subsequent reaction of this latter oxide layer with the already existing Ta_2O_5 leads to the creation of $CrTaO_4$.
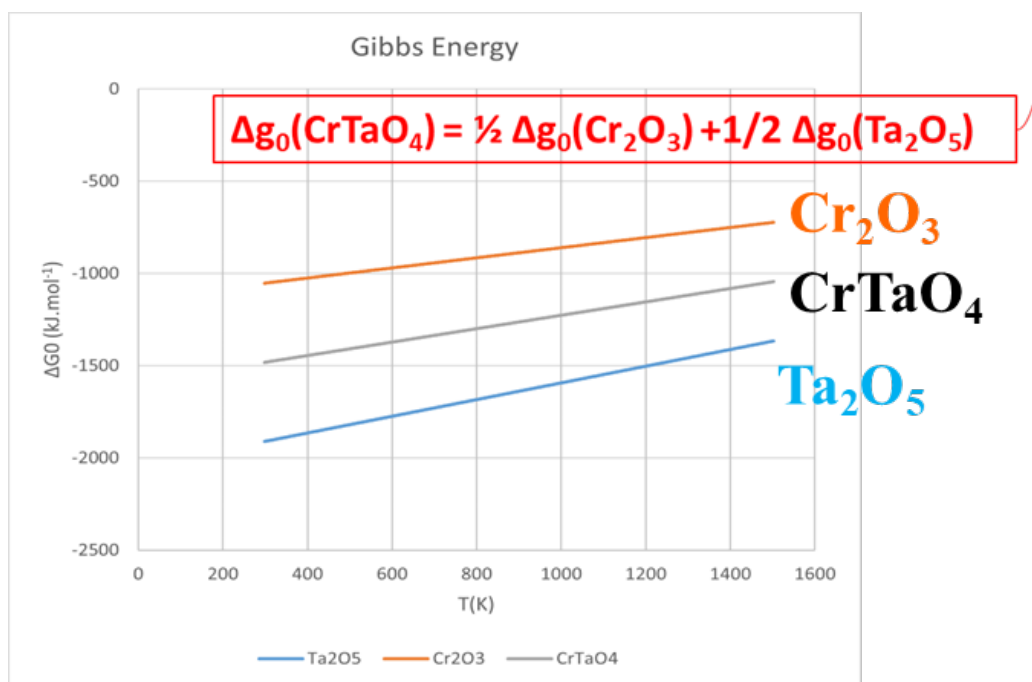

Figure 4.2. Calculation of CrTaO4 energy of formation as a funciton of temperature at equilibrium.

This theoretical formation process is systematically depicted in Fig. 4.3. The illustration methodically outlines the stages of oxide development, initially showing Ta_2O_5's formation due to its lower oxygen pressure requirement. This is followed by the emergence of Cr_2O_3. Crucially, the figure highlights the interaction between Cr_2O_3 and pre-existing Ta_2O_5, elucidating the formation pathway to $CrTaO_4$. Figure 4.3 serves not just as a visual guide to the sequence of oxide formation but also corroborates the theoretical calculations and hypotheses about the formation mechanisms under the given conditions.
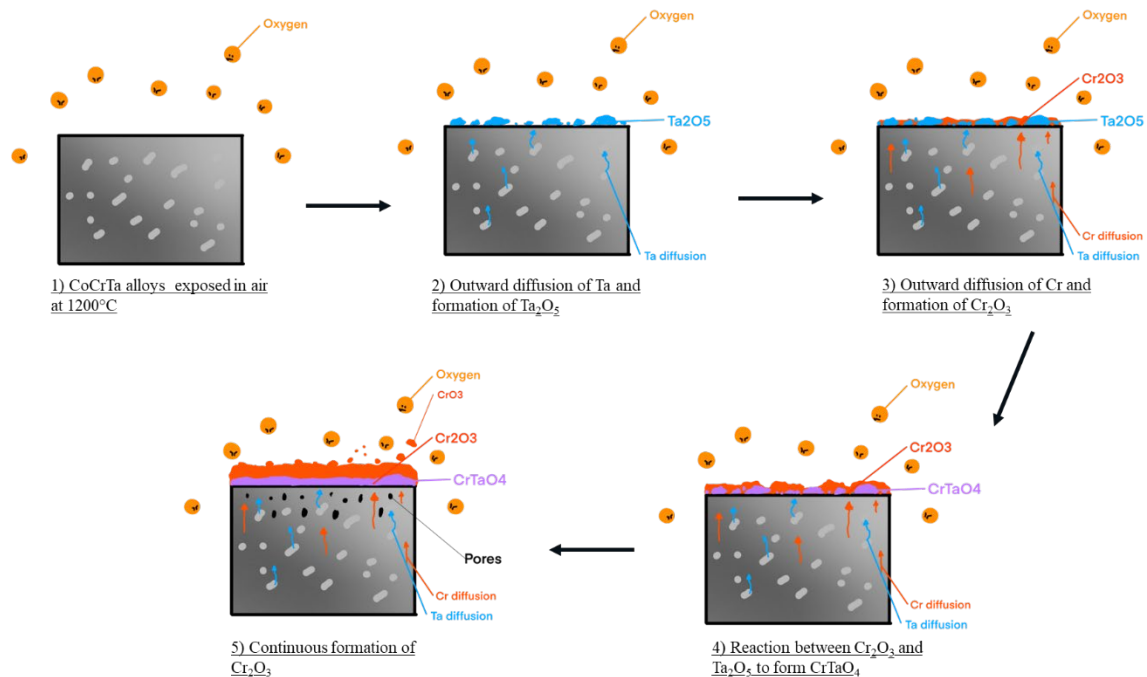
Figure 4.3. Schematisation of the formation of $CrTaO_4$ at 1200 °C in air.

However, our sample analysis did not detect Ta_2O_5, indicating that at 1200 °C, the reaction between Cr_2O_3 and Ta_2O_5 occurs so rapidly that only Cr_2O_3 and $CrTaO_4$ are observable. Yet, the pattern of oxide layer formation observed — with a $CrTaO_4$ layer consistently adjacent to the alloy substrate and a Cr_2O_3 layer outside the $CrTaO_4$ layer — seems to validate the hypothesized formation process.

Furthermore, our findings indicate that different alloy samples display varied oxidation behaviors. Initial results revealed that samples like CoCrTa-8 and CoCrTa-9, which were predicted by machine learning to contain only 1-1.4at% of Ta, did not lead to the formation of $CrTaO_4$. This suggests, in line with our hypothesis, that a certain minimum amount of Ta is necessary for the formation of Ta_2O_5, which in turn is crucial for the subsequent formation of $CrTaO_4$ through its reaction with Cr_2O_3. Additionally, the presence of Cr_2O_3 is not only vital for the formation of $CrTaO_4$ but also plays a key role in enhancing the oxidation resistance of CoCrTa alloys at 1200 °C due to its continuous formation. This implies that a minimum

percentage of Cr is likely essential as well. To further illustrate this, Fig. 4.4 presents the

parabolic rate constants, Kp, derived from the data of thermogravimetric analysis (TGA) curves

at 1200 °C for 100 h in air (as detailed in Section 3.2.1), plotted against the compositional ratio

of Cr to Ta (Cr/Ta atomic ratio).

As described in Section 3.1, CoCrTa-3 shows the formation of $CrTaO_4$ after oxidation

for 20 h at 1200 °C in air that is continuous but thin, accompanied by a small amount of Cr_2O_3.

On the other hand, samples such as CoCrTa-4 and CoCrTa-5 display either instability or

brittleness. In contrast, CoCrTa-6 and CoCrTa-7 present a continuous, thick $CrTaO_4$ oxide layer

with a stable and thick Cr_2O_3 even after 20 h of exposure to air at 1200 °C. This variance

highlights the significant impact of chromium and tantalum contents on the stability and

formation of $CrTaO_4$ during oxidation. According to Fig. 4.4, a compositional ratio Cr/Ta (in

atomic percent) in the range of 4 to 7 corresponds to samples suitable for the formation of
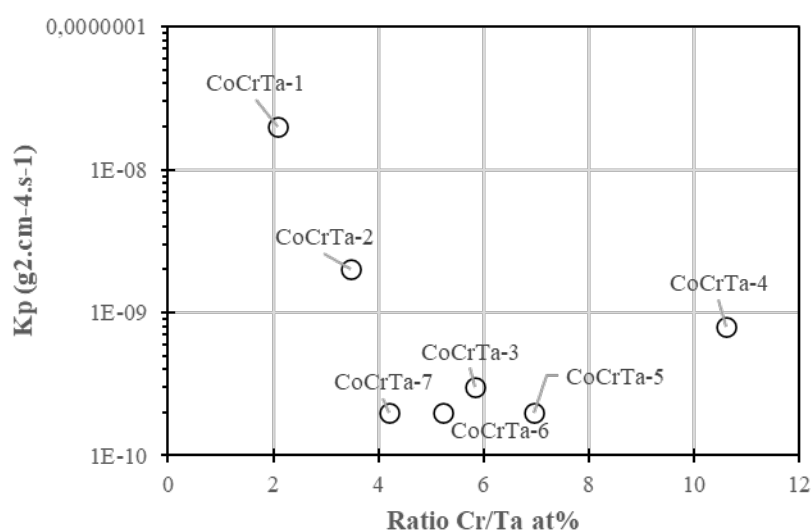
$CrTaO_4$.

Figure 4.4. Parabolic constant rate vs. Cr/Ta atomic ratio for oxidation at 1200 °C for 100 h in air.

To confirm this hypothesis, the mass change after oxidation for 50 h and 100 h as well

as 20 h are compared to the compositional ratio Cr/Ta in Fig. 4.5, because it has been already

noticed earlier that the mass change after 20 h of oxidation only was not sufficient to determine good oxidation resistance.

Looking at this figure, the same compositional ratio of 4 to 7 Cr/Ta (in at.%) shows the lowest mass change after oxidation for longer times and, more importantly, the smallest dispersion of the results. This is very interesting, because a small change throughout the oxidation time could indicate a good protection of the alloy against exposure at 1200 °C in air. These assumptions have already been confirmed by the microstructure of these samples after oxidation at 1200 °C for 100 h in Fig. 3.9.
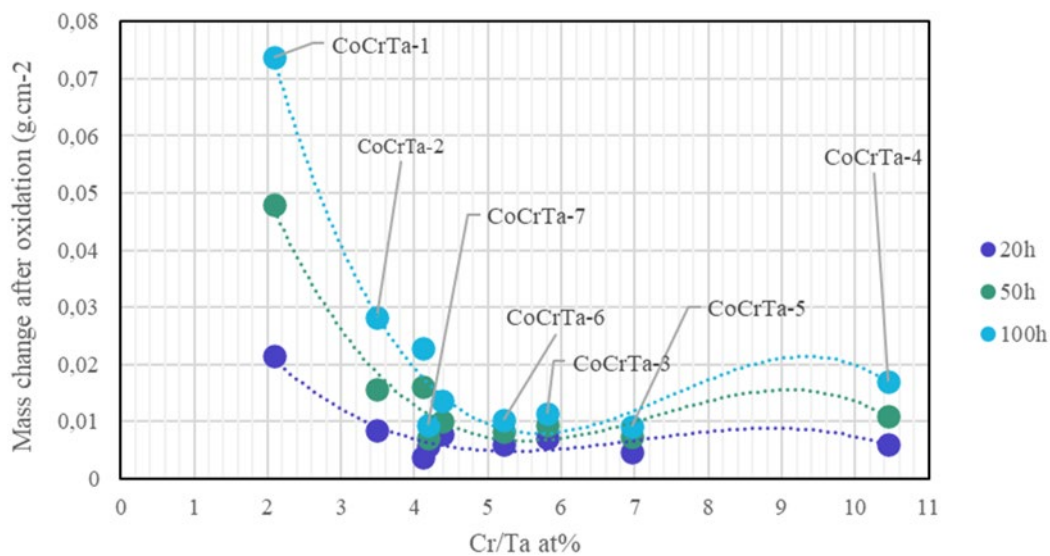

Figure 4.5. Mass change after oxidation as a function of Cr/Ta atomic ratio.

In summary, the formation of $CrTaO_4$ results from the reaction of Ta_2O_5 and Cr_2O_3. As evident from no Ta_2O_5 after oxidation for 20 h at 1200 °C, this reaction occurs very quickly during the oxidation. A Cr content of more than 30 at.% seems enough to form Cr_2O_3, but an insufficient Ta content does not allow the formation of $CrTaO_4$. Our results showed that a compositional ratio of Cr/Ta between 4 to 7 is suitable for the formation of $CrTaO_4$.

4.2. Refining the Co-Cr-Ta composition for enhanced $CrTaO_4$ formation

To substantiate this theory, two new alloy compositions were chosen so that they adhere to the established Cr/Ta ratio and contain minimum chromium and tantalum contents. Their

compositions are shown in Table 4.1 and added to the ternary phase diagram predictions in Fig. 4.6 that we already used in Section 2.3.

Table 4.1. Composition of new Co-Cr-Ta alloys tested.

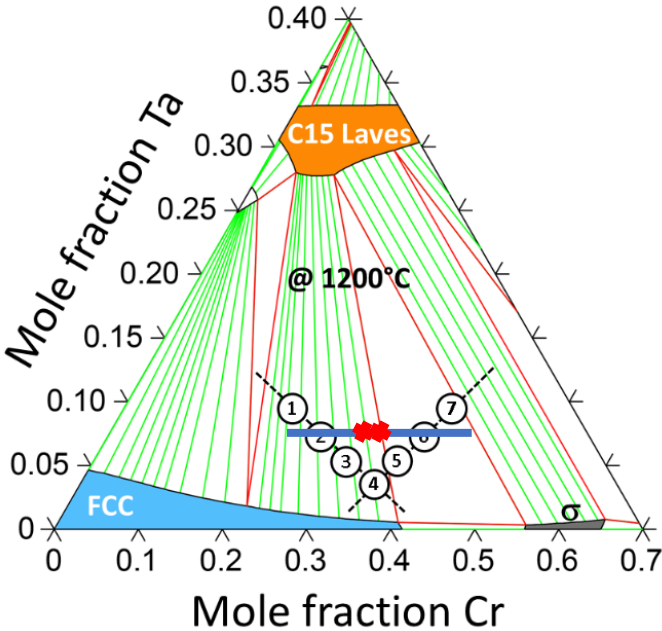| Alloy	Co (at%)	Cr (at%)	Ta (at%)
Co-Cr-Ta-11	62.7	30	7.3
Co-Cr-Ta-12	60.7	32	7.3

Figure 4.6. Updated predicted phase diagram for Co-Cr-Ta alloy system at 1200 °C by CALPHAD using TCHEA 4.

These compositions aimed to stay within the dual-phase region of the ternary phase diagram, thereby averting the formation of brittle sigma phase. Subsequent microstructural analyses after heat treatment at 1200 °C for 24 h affirmed the accuracy of the CALPHAD predictions. Only two phases were observed in the microstructures, corresponding to the Co (FCC) phase and the C15 Laves phases, as anticipated in the ternary phase diagram (Fig. 4.7).

The primary objective of testing these new samples was to validate whether these optimised compositions would indeed promote the formation of $CrTaO_4$ during oxidation.
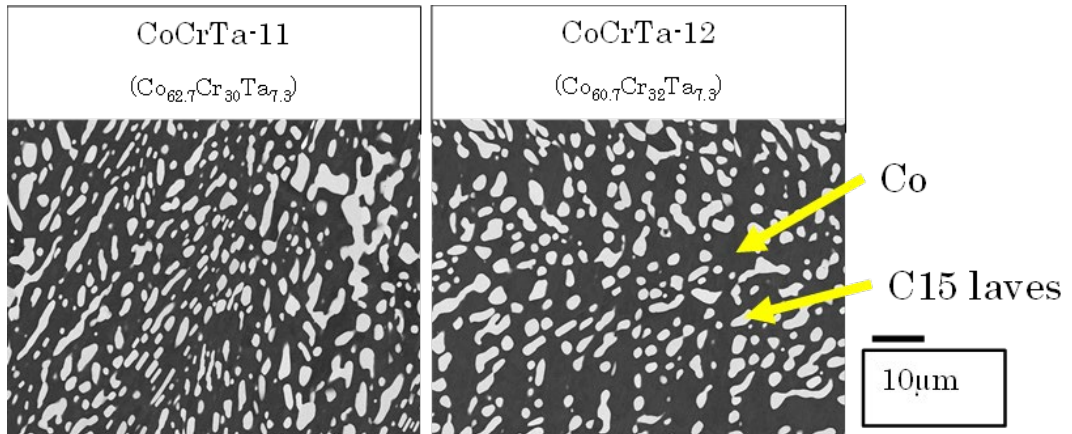
Figure 4.7. Microstructure of CoCrTa-11 and CoCrta-12 after heat treatment for 24 h at 1200 °C in Ar.

Figure 4.8 shows their microstructure after oxidation for 20 h at 1200 °C. A Cr_2O_3 oxide layer did form on these samples. However, it displayed a brittle nature and detachment from the sample during preparation for observation. Notwithstanding, the most crucial observation was the formation of a continuous and stable $CrTaO_4$ oxide layer. This finding confirms the optimisation of the Co-Cr-Ta composition and underscores the importance of a specific Cr/Ta ratio in this context. These results allow us to draft a first map of oxidation formation at 1200 °C, as presented in Fig. 4.9.
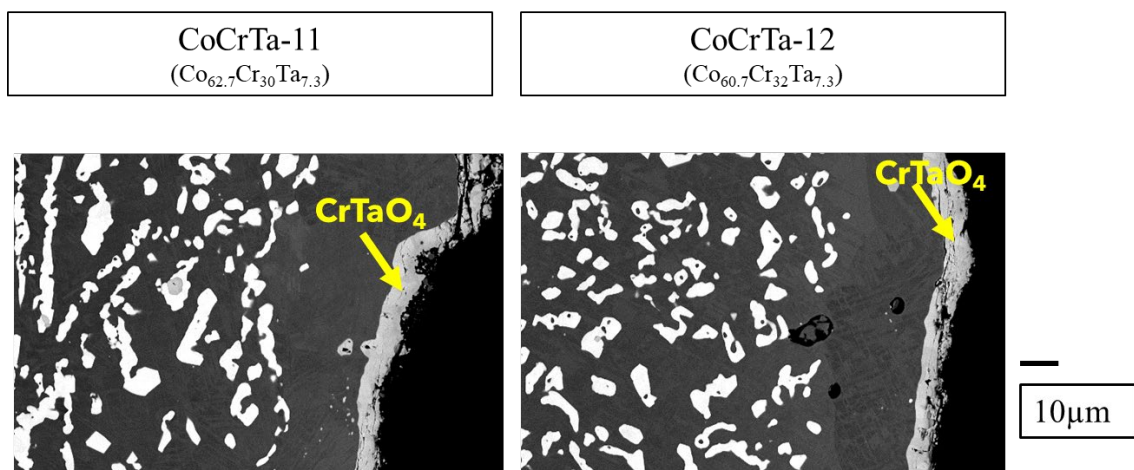

Figure 4.8. Microstructure of CoCrTa-11 and CoCrTa-12 after oxidation for 20 h at 1200 °C in air.
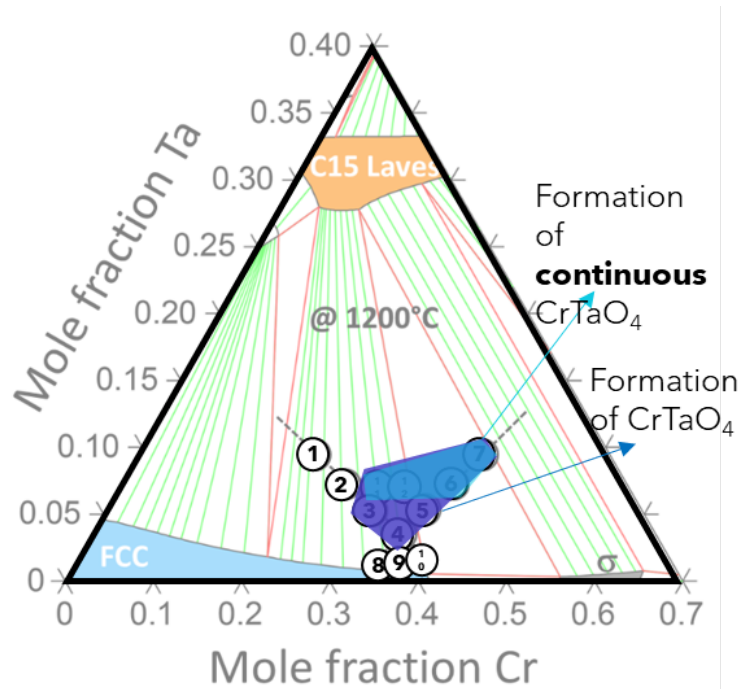
Figure 4.9. Draft of an oxide formation map of Co-Cr-Ta samples after exposure in air at 1200 °C.
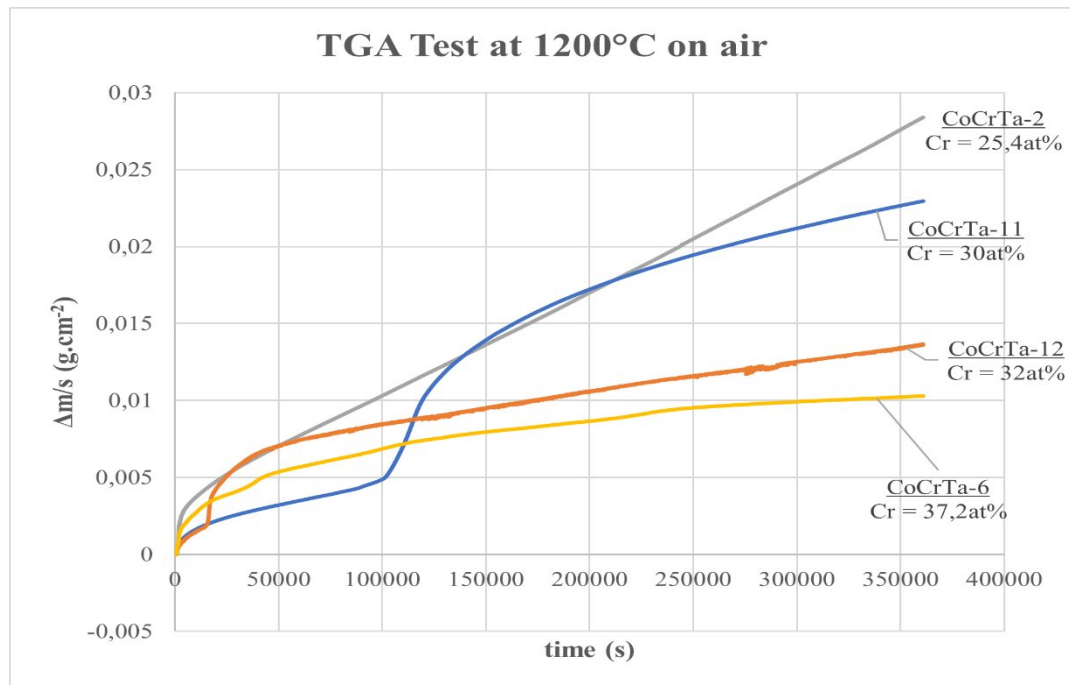

Figure 4.10. TGA curves of the CoCrTa samples after oxidation for 100 h at 1200 °C.

The oxidation behavior of these new alloys was further analyzed through thermal gravimetric analysis (TGA) over a duration of 100 h at 1200 °C and the results are presented in Fig. 4.10. The TGA results revealed different oxidation kinetics among these two samples. For instance, CoCrTa11 exhibits rapid oxidation kinetics after 27 h accompanied by a large amount of mass gain, despite the microstructural analysis after 20 h indicating the formation of $CrTaO_4$(Fig. 4.8), but CoCrTa-12 does not show such a rapid oxidation. Obviously, not only the formation of $CrTaO_4$ but also their stability should be investigated in association with the alloy composition.

4.3. Summary

This chapter has successfully demonstrated the role of composition for the formation of $CrTaO_4$ and confirmed its help in improving the oxidation resistance of Co-Cr-Ta alloys at high temperatures. The study has meticulously outlined the crucial role of each element to ensure the effective formation of $CrTaO_4$. Our research revealed that Co-Cr-Ta alloys require a minimum tantalum content of 5 at.%, a chromium content range of 32 at.% to 40 at.%, and a compositional ratio of 4<Cr/Ta<7 to form a $CrTaO_4$ oxide. However, while these results are promising for enhancing the oxidation resistance at 1200 °C, they alone do not satisfy the suitability of these alloys for use in glass fiber spinners. Further investigation into their mechanical properties is imperative.

The findings presented in chapter 3 and this chapter underscore the potential of machine learning, specifically Bayesian optimisation, in determining the optimal composition of CoCrTa alloys to ensure the formation of $CrTaO_4$. As presented earlier in section 3.1, this approach is adept at navigating the intricate parameters of alloy compositions, considering variables such as temperature, oxidation mass change, and elemental ratios. The new data, including for example thermal gravimetric analysis (TGA) results and the revised minimum requirements for

chromium and tantalum content, offer a fresh perspective for machine learning application. By analyzing this extensive dataset from previous experiments, these advanced algorithms can predict alloy performance more accurately and more precise targets. Iteratively testing new compositions through Bayesian optimisation, informed by this enriched data set, holds promise for identifying the ideal CoCrTa composition for maximum oxidation resistance.

Chapter 5: Mechanical properties of Co-Cr-Ta alloys

5.1. Preparation of Co-Cr-Ta tensile test samples

To assess the suitability of an alloy for use in a high-speed spinner, it's crucial to evaluate both its oxidation resistance and mechanical properties at 1200 °C. This is because the spinner operates at speeds exceeding 1200 revolutions per minute, and the alloy must withstand these conditions without deforming in a way that would render it unsuitable for fiber production.

To examine the mechanical properties, tensile samples of the alloys must be prepared. This requires producing 7 kg bulks of the alloys using an induction furnace. An important step in this process is to ensure that the alloys produced by different methods maintain consistent integrity and microstructure. Fig. 5.1 presents images of the two alloy production processes.
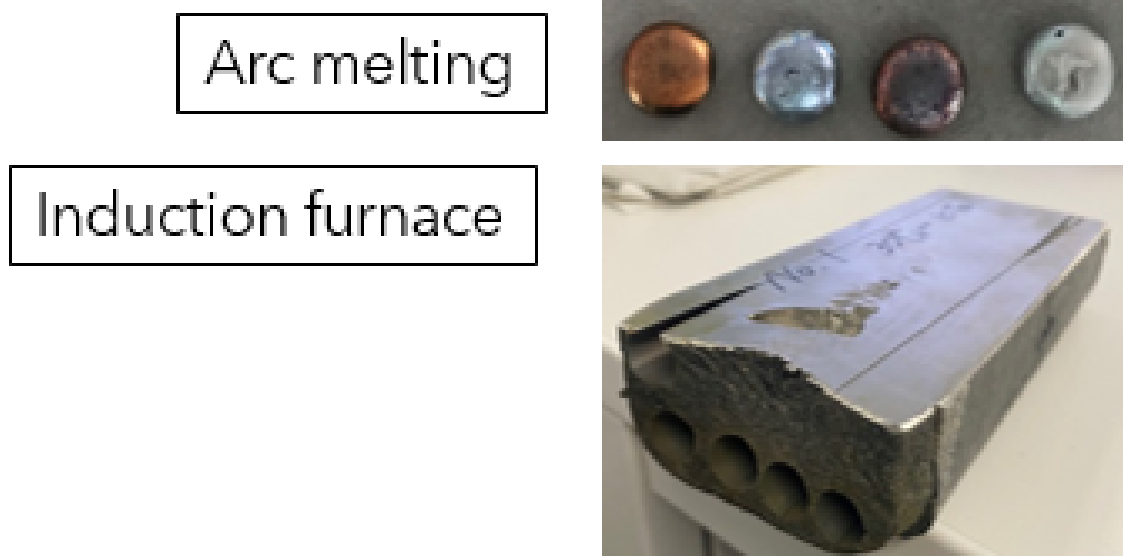

Figure 5.1. Difference of size between the two processes of making of alloys :
(a) arc melting and (b) induction furnace.

To ascertain the consistency of results across different processing methods, microstructural analyses of CoCrTa alloys were conducted following a 20-hour oxidation period at 1200 °C. The corresponding images are displayed in Fig. 5.2.
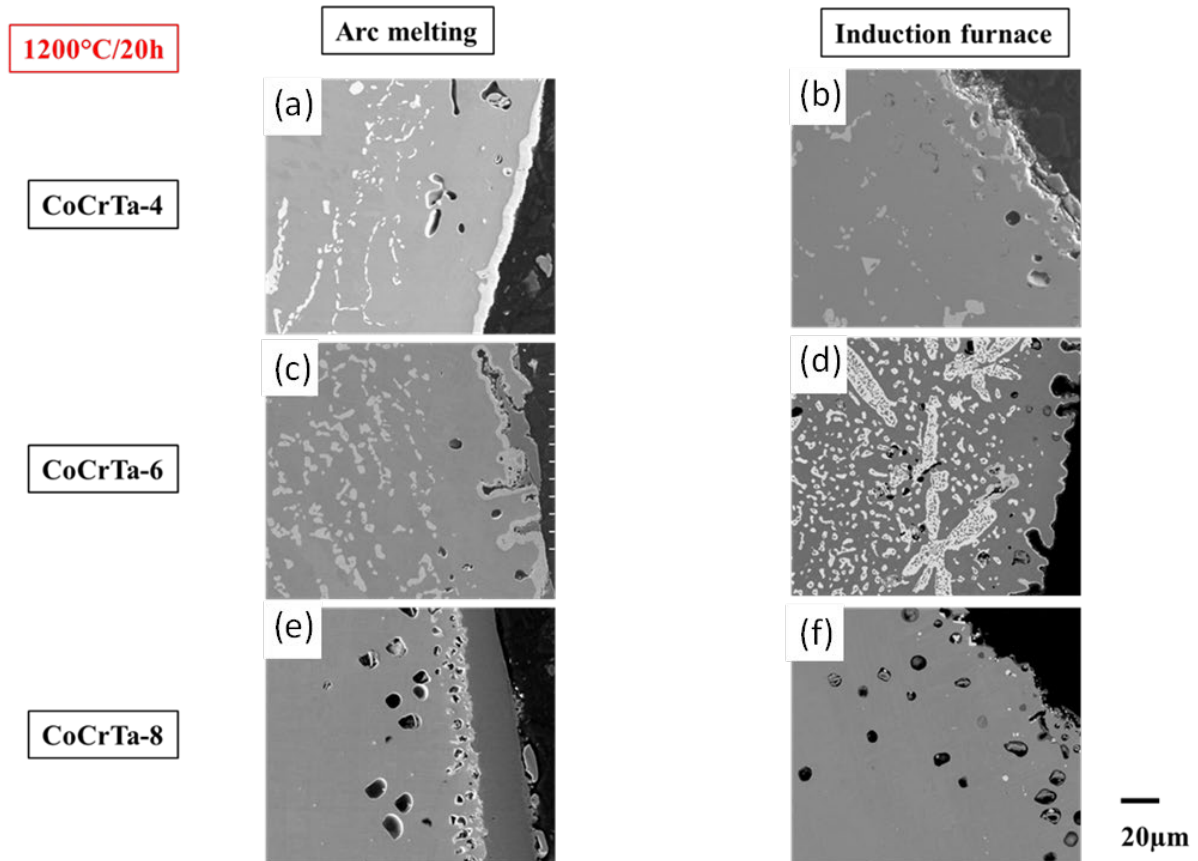
Figure 5.2. Microstructure of CoCrTa alloys after oxidation at 1200 °C for 20 h depending on process: (a), (c), and (e) arc melting in Ar gas, and (b), (d), and (f)induction furnace.

The analysis revealed a high degree of similarity in the microstructure of the alloys, as evidenced by the presence of the same Co FCC phase and C15 Laves phase. Additionally, comparable oxidation resistance profiles were confirmed by the identical number of pores and the formation of Cr_2O_3 or $CrTaO_4$. A notable deviation was observed in the CoCrTa-6 composition prepared by induction furnace, where segregation of the C15 Laves phase was detected. Furthermore, the 7 kg bulk samples exhibited increased brittleness at room temperature compared to those prepared via arc melting. This brittleness could be attributed to

the heavy elements such as tantalum in the alloy, which are prone to gravitational segregation during the cooling of bulk samples. Another hypothesis is that this difference is attributed to the residual stress caused by casting.

Despite this difference, the other samples showed very close behaviors. Thus, these bulks were used to make tensile test samples and determine the mechanical properties of the compositions.

5.2. Tensile tests at room temperature and 1200 °C

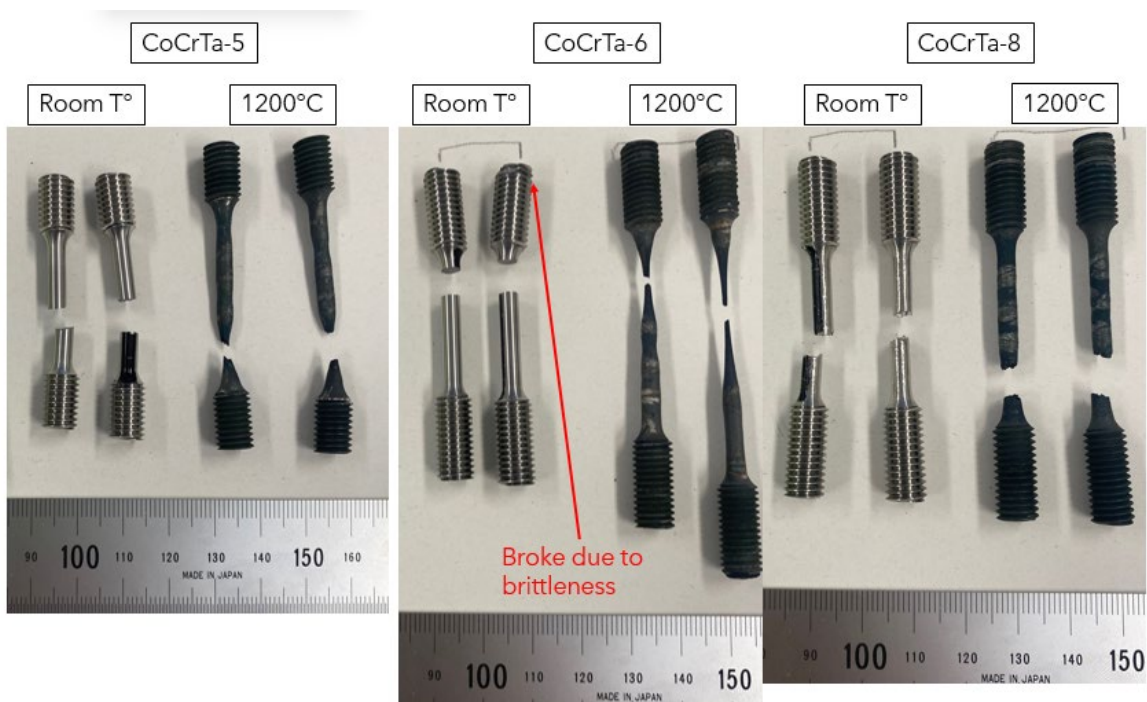## 5.2.1. Tensile tests at room temperature and 1200 °C for CoCrTa alloys

Figure 5.3. Tensile samples after tensile tests at room temperature and at 1200 °C.

Figure 5.3 depicts the tensile specimens deformed by the tensile tests at room temperature and at 1200 °C. In this figure, the brittleness of the CoCrTa-6 bulk previously observed after casting is evident. Indeed, the tensile specimens exhibited brittleness even before

testing, during their installation on the machine, as illustrated by the specimen in Fig. 5.3 and the fractures observed at the threading. Additionally, a conspicuous observation can be made regarding the tensile specimens after the 1200 °C test. A significant elongation is observed in all specimens, particularly in CoCrTa-6, which appears to have elongated considerably, with a noticeable reduction in diameter at the rupture point. Furthermore, unlike room temperature tensile tests, fractures occur near the threading of the specimens. These profiles do not seem consistent with a material suitable for glass fiber spinner plates. If such deformation is observed during spinner usage, it could lead to rapid obsolescence of the component, necessitating replacement despite its good oxidation resistance due to the high rotation speeds endured by the spinners.
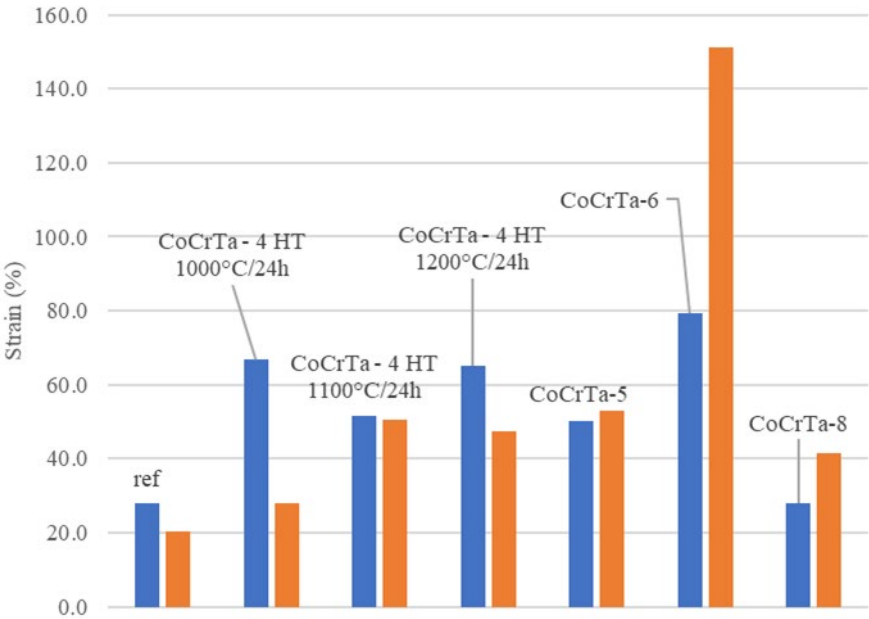
Figure 5.4. Elongation after tensile test at room temperature (blue bar) and 1200 °C (red bar); CoCrTa-4 alloys were subjected to three different heat treatments before the test, as specified, while the others were heat treated at 1200 °C for 24 h.

The substantiation of these assumptions is further reinforced by the detailed insights presented in Fig. 5.4, illustrating elongation percentages during tensile tests conducted at both 1200 °C and room temperature. For comparative purposes, identical tensile tests were applied to the reference material, TaTiC4, which exhibited a strain of nearly 30% at room temperature.

This value was only achieved by CoCrTa-8. However, as previously observed, the deficiency in oxidation resistance of CoCrTa-8, attributed to inadequate $CrTaO_4$ formation, renders the combination of these properties unsuitable for spinner use. Notably, a substantial discrepancy emerges after tensile test at 1200 °C, with the reference material displaying a strain of 20%, in stark contrast to the 41% observed for CoCrTa-8.

Other compositions of CoCrTa showcase significantly higher elongations. CoCrTa-4, at room temperature, demonstrates an average elongation of 60%. To investigate the potential influence of heat treatment on mechanical properties, this composition underwent three distinct heat treatments. Results revealed that the strains at room temperature are 64%, 52%, and 63% for 1000, 1100, 1200 °C heat treatments, respectively, slightly depending on the heat treatment temperature. On the other hand, tensile test at 1200 °C for CoCrTa-4 subjected to a 1000 °C/ 24 h heat treatment exhibited a reduced strain of 28% in contrast to the 57% for 1100 °C/24 h and 56% for 1200 °C/24 h. This implies that the heat treatment at the lowest temperature resulted in a decreased elongation at 1200 °C (Fig. 5.4).

In Fig. 5.4, CoCrTa-5 demonstrates results akin to CoCrTa-4 for the same heat treatment. While the strain at room temperature of the CoCrTa-5 is slightly lower than that of CoCrTa-4, the result after testing at 1200 °C is 55%, being slightly higher than that of CoCrTa-4. Lastly, CoCrTa-6 displays the most remarkable results, with an 80% strain after a room temperature test and an escalated strain of 146% after testing at 1200 °C. This outcome is particularly surprising given the promising oxidation resistance of the CoCrTa-6 composition at 1200 °C. Although the Cr content is crucial for oxidation resistance, as discussed in Section 4.1, comparative results suggested significant influence of chromium addition on the fragility of samples at room temperature and their strain at 1200 °C, as discussed below.

The comprehensive analysis of tensile properties and microstructural observations provides essential insight into the mechanical behavior of various CoCrTa compositions. While

certain compositions exhibit promising characteristics at elevated temperatures, careful consideration must be given to their brittleness at room temperature. The correlation between alloy composition, heat treatment, and mechanical performance furnishes valuable information for selecting materials suitable for high-speed spinner applications.

Figure 5.5 illustrates tensile test results at 1200 °C as a function of composition. Firstly, the reference material exhibits a deformation profile markedly different from the other compositions, with a force of 50 MPa before reaching plastic deformation and 57 MPa before rupture occurring after a mere elongation of 5.6 mm. Interestingly, the curves naturally arrange themselves based on the chrome content of the compositions: 33.7, 35, 36.2, and 37 at.% for CoCrTa-8, -4, -5, and -6, respectively. Numerous differences between the profiles are noteworthy. Initially, a significantly lower applied force causes plastic deformation (CoCrTa-8: 51 MPa; CoCrTa-6: 40 MPa). Additionally, the elongations before rupture are vastly different (CoCrTa-8: 8 mm; CoCrTa-6: 17 mm). This underscores that, despite its promising behavior
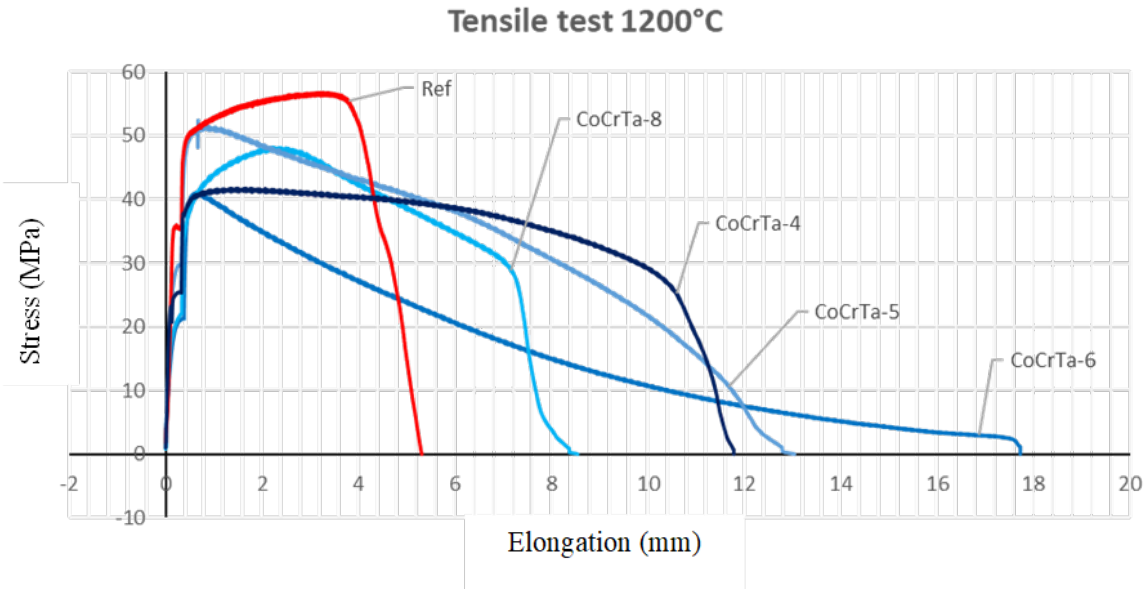

Figure 5.5. Stress-elongation curves at 1200 °C as a function of Cr content in the CoCrTa samples in comparison with the reference material: 33.7, 35, 36.2, and 37 at.% Cr for CoCrTa-8, 4, 5, and 6, respectively.

against oxidation at 1200 °C, a chromium content as high as 37 at.% in CoCrTa-6 makes it unsuitable for spinner applications.

To confirm that this effect is indeed linked to the chromium content and not other elements, tensile tests at 1200 °C were conducted for compositions CoCrTa-6, CoCrTa-11, and CoCrTa-12, all having 7.2 at.% of Ta but with 37, 30, and 32 at.% of Cr, respectively. These results are depicted in Fig. 5.6. The figure substantiates the chromium's effect on the tensile profiles. Particularly noteworthy is the similarity in the deformation profile between CoCrTa-12 and CoCrTa-6; elongation before rupture significantly increases with chromium content (CoCrTa-11: 40%; CoCrTa-12: 120%; CoCrTa-6: 160%).
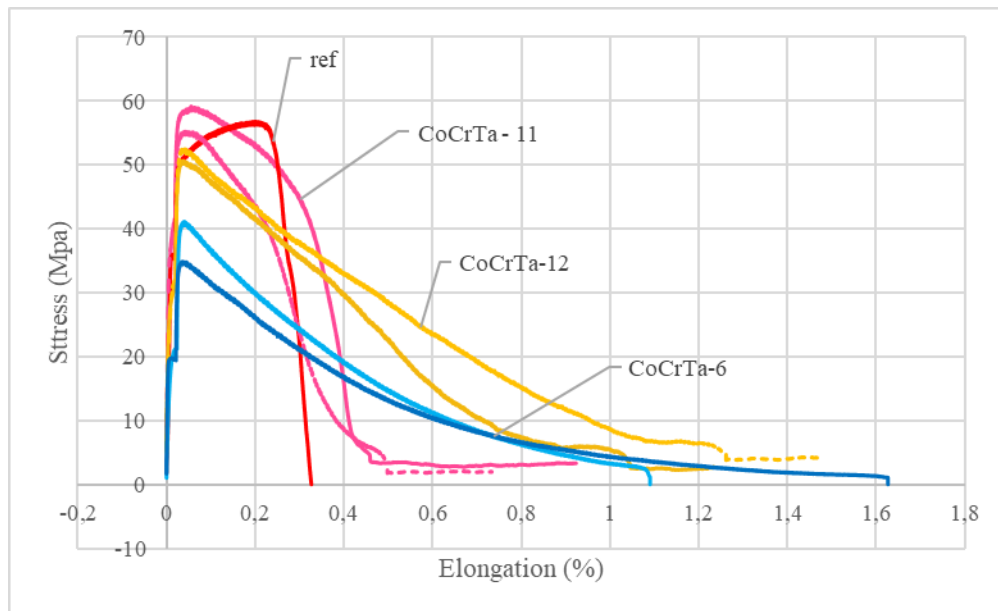
Figure 5.6. Stress-strain curves at 1200 °C for samples with 7 at.% of Ta but different amount of Cr: CoCrTa-11 (30 at.%), CoCrTa-12(32 at.%) and CoCrTa-6(37 at.%). Two samples were tested for each composition.

To summarize, the comprehensive analysis of the mechanical properties of Co-Cr-Ta ternary alloy systems provides valuable insights into their performance, particularly under high-temperature conditions relevant to applications like high-speed spinners. The observed brittleness at room temperature, notably in CoCrTa-6, highlights a crucial consideration for their application in spinner components. The correlation between alloy composition, heat treatment,

and mechanical behavior underscores the intricate balance required for optimal performance in demanding environments.

5.2.2. Tensile tests at room temperature and 1200 °C for CoCrTa alloys with carbon addition

Exploring avenues for further enhancement, the introduction of carbides emerges as a promising strategy to augment the mechanical properties of the CoCrTa alloys. The incorporation of carbides into the alloy matrix holds the potential to for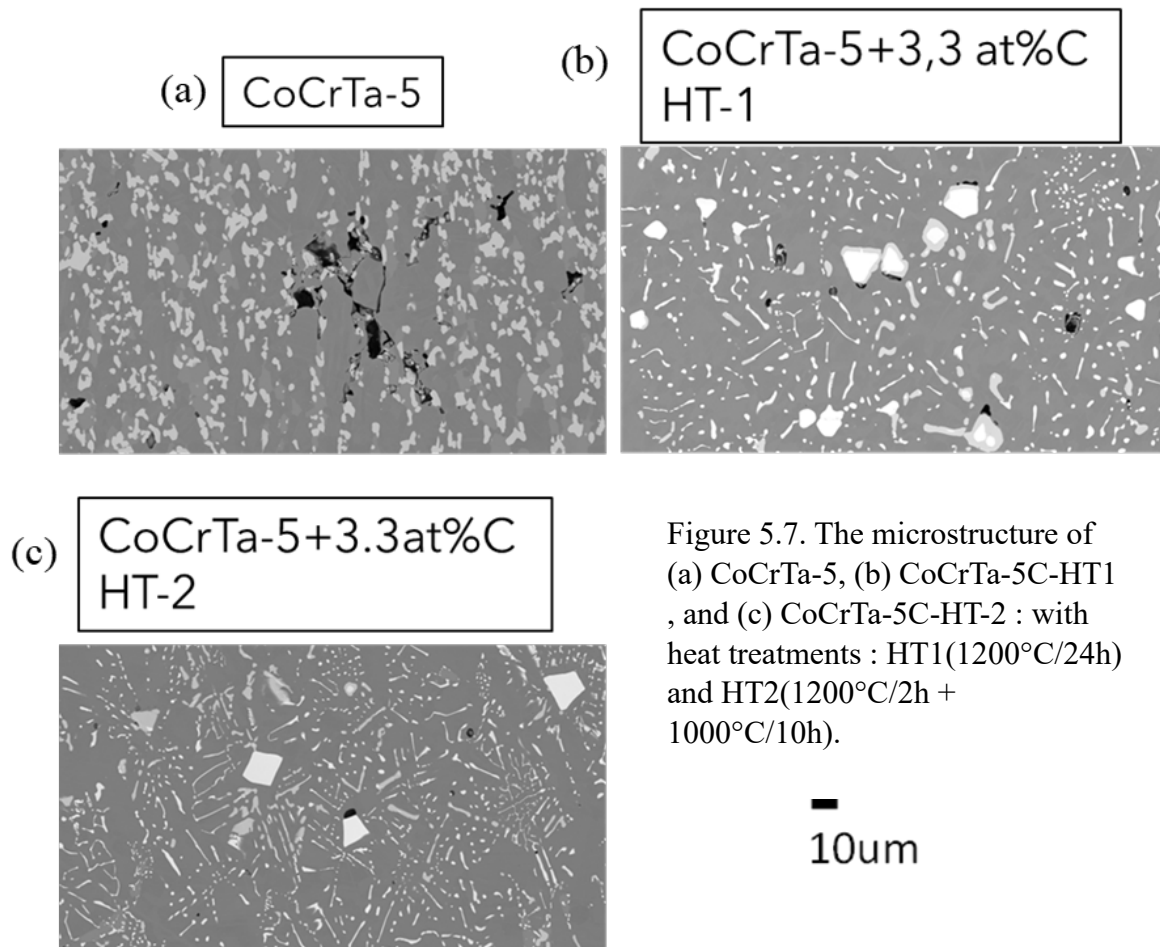tify structural integrity, mitigate brittleness, and enhance overall mechanical durability. This avenue presents an exciting opportunity to fine-tune the alloy's composition, opening new possibilities for achieving an optimal balance between high-temperature stability and mechanical resilience in high-speed spinning applications.

As we delve into the realm of alloy development, the prospect of incorporating carbides into Co-Cr-Ta ternary systems beckons further exploration. This endeavor not only expands the scope of alloy design but also positions these materials for broader applications, pushing the boundaries of their mechanical performance in extreme operating conditions.

As the composition CoCrTa-6 turned out to be brittle while casting a bulk of 7 kg, an experiment was conducted using the composition CoCrTa-5. To try to improve the poor mechanical properties observed, 3.3 at.% C was added to the CoCrTa-5 in exchange of the same percent of Co. As the addition of carbide was the target of this study, two heat treatments were tested. One is a 1200 °C/24 h heat treatment (named HT1), which was chosen to compare with previous results of the CoCrTa-5, and the other the heat treatment of 1200 °C/2 h followed by 10 h at 1000 °C (named HT2), which was developed by Saint-Gobain. The microstructure of these two new samples is presented in Fig. 5.7 in comparison with a carbon-free sample.

Figure 5.7. The microstructure of (a) CoCrTa-5, (b) CoCrTa-5C-HT1 , and (c) CoCrTa-5C-HT-2 : with heat treatments : HT1(1200°C/24h) and HT2(1200°C/2h + 1000°C/10h).

10um

This figure clearly presents the presence of carbides. As a matter of fact, no real difference in microstructure could be observed between the two heat-treatments. As a first step, to make sure that the addition of carbide does not affect the oxidation resistance of the CoCrTa compositions, an oxidation test at 1200 °C for 20 h was conducted for both CoCrTa-5 with carbon and presented in Fig. 5.8. This figure shows that no real difference is observed between the CoCrTa-5 and the CoCrTa-5C-HT1 and the CoCrTa-5C-HT2 after oxidation. Moreover, the carbides are still observable and stable after oxidation. In addition, the formation of the protective $CrTaO_4$ was observed, making this study promising to reach the goal of having both good oxidation resistance and mechanical properties at 1200 °C.
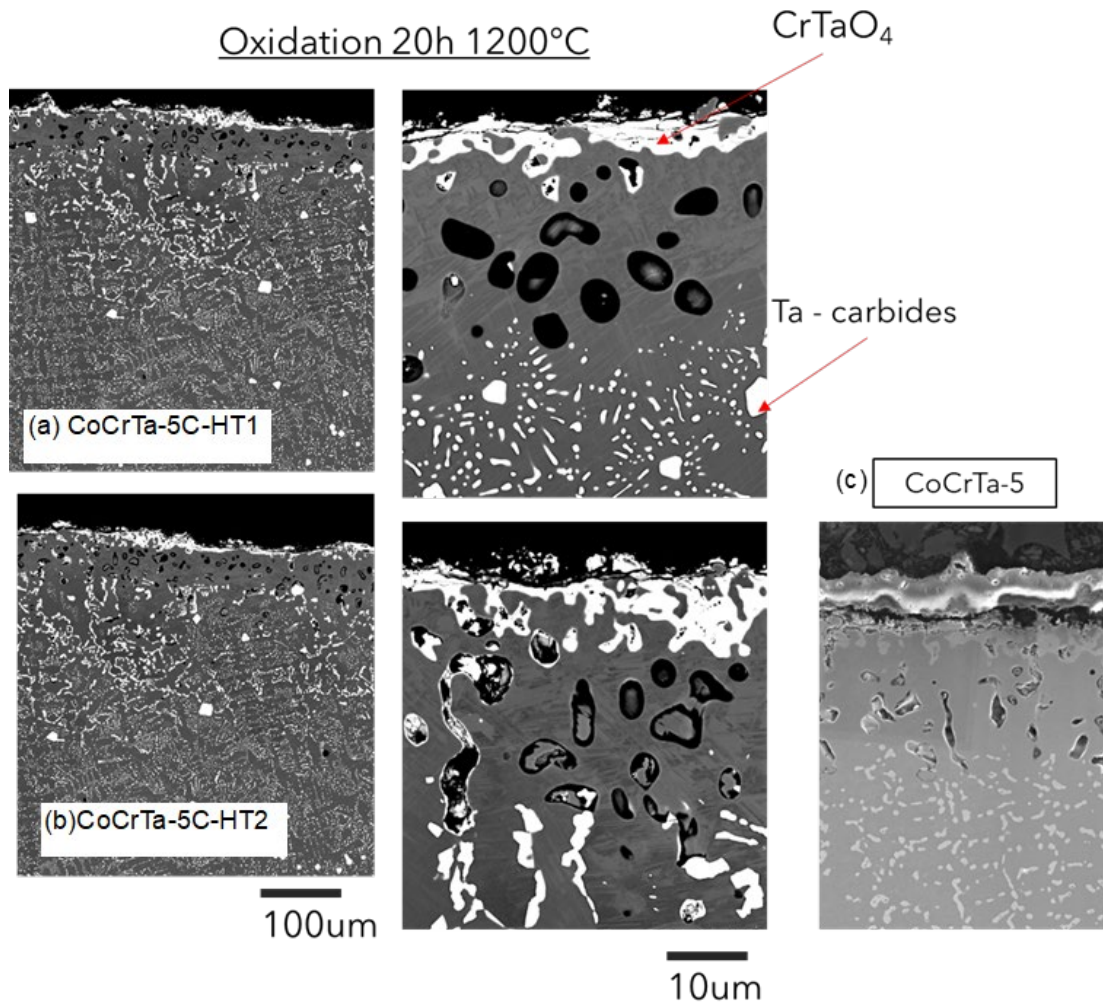
Figure 5.8. Comparison between (a) CoCrTa-5C-HT, (b) CoCrTa-5C-HT2 and (c) CoCrTa-5 after 20 h oxidation at 1200 °C.

With the reassurance that the addition of carbides does not affect the oxidation resistance of the CoCrTa sample, tensile tests were conducted at 1200 °C and the results are presented in Fig. 5.9. This figure provides the results of the 0.2% proof stress for a tensile test at 1200 °C. This analysis significantly reveals the impact of carbide incorporation into the composition. Specifically, the 0.2% stress of the CoCrTa-5 alloy undergoes a noteworthy evolution, transition from 20 MPa in the absence of carbides to 30 MPa with the addition of carbides.

This observed variation distinctly highlights the beneficial influence of carbide addition on the mechanical properties of the alloy. These findings suggest that the presence of carbides significantly contributes to enhancing the material's resistance, particularly in terms of plastic

Figure 5.9. 0.2% proof stress for tensile test at 1200 °C.

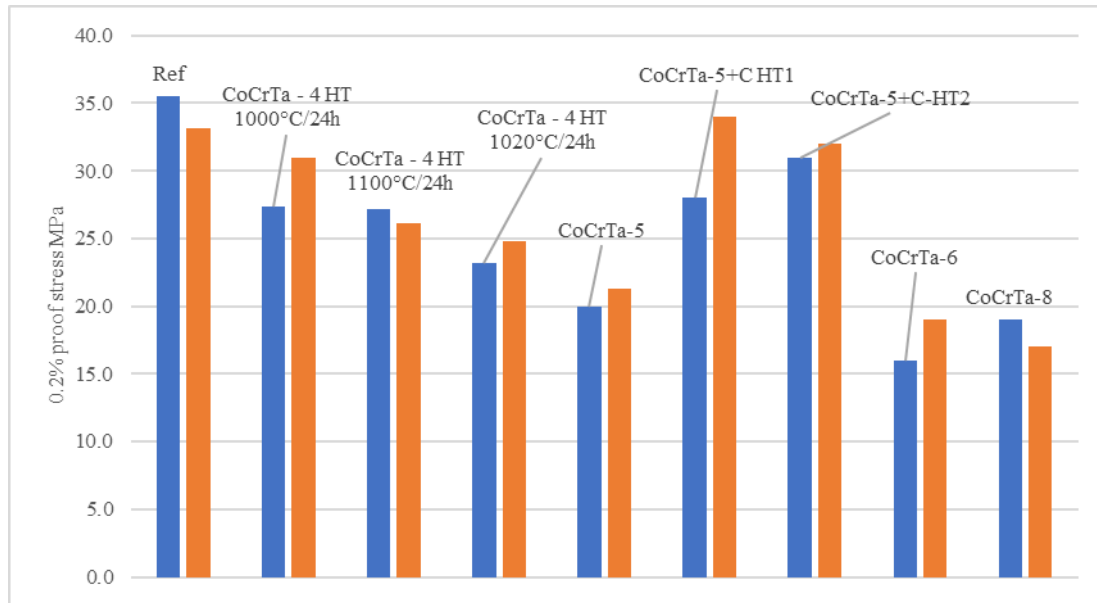deformation. However, those results did not indicate the influence of heat treatment on the improvement of the mechanical properties of CoCrTa-5 + carbides.

Importantly, these new 0.2% stress values closely align with those obtained with the reference alloy (Ref). This convergence indicates that the incorporation of carbides not only promotes increased resistance to deformation but also yields an overall mechanical performance similar to that of the reference alloy.

To further substantiate the positive effect of carbide addition, a comprehensive analysis of the complete tensile test curves at 1200 °C for the compositions CoCrTa-5, CoCrTa-5+C-HT1, CoCrTa-5+C-HT2 was conducted and compared to the properties of the reference material (Ref), as detailed in Fig. 5.10. Initially, the pronounced influence of carbide addition on the curve profiles is apparent. While the CoCrTa-5 composition exhibits plastic deformation profiles with an elongation of approximately 80%, the CoCrTa-5+C compositions display significantly reduced plastic deformation before rupture, requiring substantially higher stress (greater than 50 MPa, compared to approximately 40 MPa for CoCrTa-5). These results
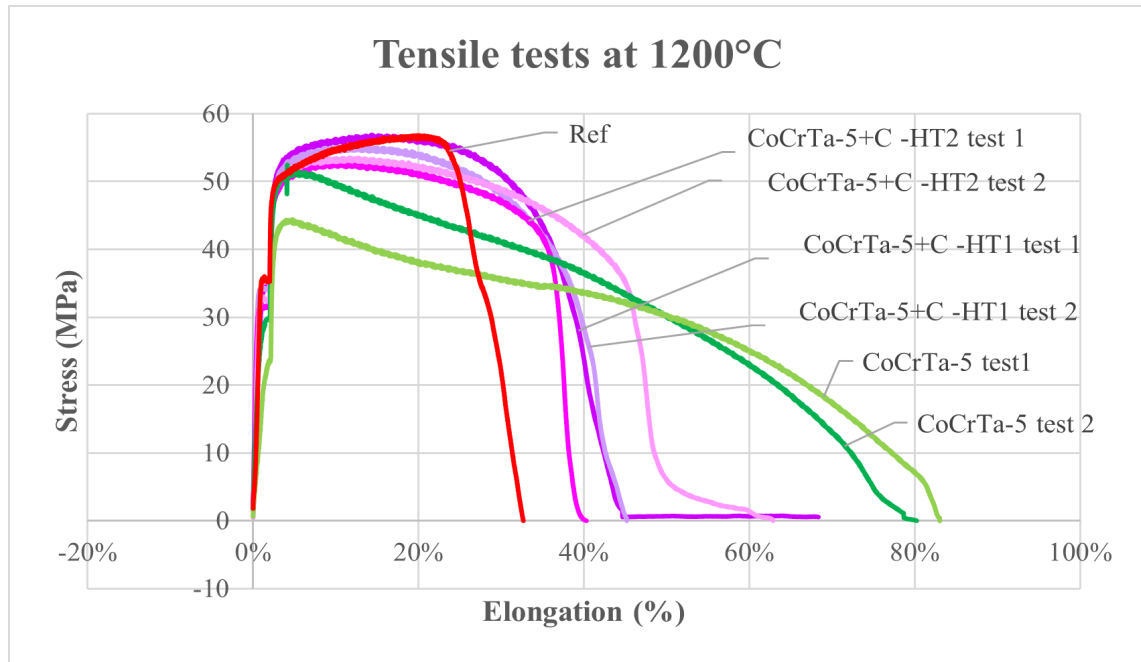
Figure 5.10. Stress-strain curves at 1200 °C of reference material (Ref) compared to compositions CoCrTa-5 and CoCrTa-5+C with heat treatment: 1200°C/24h (HT1) or 1000 °C/2 h + 1200 °C/24 h (HT2).

converge towards those of the reference material (Ref), robustly reinforcing the relevance of carbide integration for enhancing the mechanical properties of CoCrTa compositions.

Moreover, elongation experiences a notable reduction, ranging between 40% and 50% before rupture, which are much closer to those of the reference material (28%). These findings robustly confirm the beneficial effect of carbide addition in improving the mechanical performance of CoCrTa compositions. However, again, those results didn't show any explicit effect of the heat treatment on the mechanical properties of CoCrTa-5+C.

These results suggest that carbide incorporation not only alters plastic deformation profiles but also contributes to mechanical properties more closely aligned with those of the reference material. These observations offer promising prospects for targeted optimisation of CoCrTa alloys for applications requiring increased mechanical strength.

In summarizing this chapter, the outcomes of mechanical tests conducted at 1200 °C

have been compiled in Table 5.1, shedding light on the distinct challenges inherent in ternary CoCrTa alloys, particularly when juxtaposed with the reference material. These observations are crucial in the context of evaluating their suitability for application in spinner development within the realm of fiberglass manufacturing.

Table 5.1. Mechanical properties of CoCrTa compositions vs reference materials at 1200 °C.

Sample name	Heat treatment	0,2% Proof Load (kN)	0,2% Proof Stress (MPa)	Maximum Load before rupture (kN)	Tensile stress before rupture (MPa)	elongation (%)	reduced area (%)	remarks
Ref	1200°C/2h + 1000°C/10h	0,462	35,5	0,739	56,8	27,9	36,2	Reference material
	1200°C/2h + 1000°C/10h	0,43	33,1	0,628	48,3	20,2	27,8	
CoCrTa-4	1000°C/24h	0,357	27,4	0,582	44,8	66,8	44,9	
	1000°C/24h	0,403	31	0,658	50,7	28	48,8	
	1100°C/24h	0,353	27,2	0,623	48,1	51,7	54,2	
	1100°C/24h	0,338	26,1	0,582	44,9	50,7	48,7	
	1200°C/24h	0,3	23,2	0,54	41,8	65	56,7	
	1200°C/24h	0,321	24,8	0,588	45,4	47,4	45,8	
CoCrTa-5	1200°C/24h	0,261	20	0,684	52	50,1	77,6	
	1200°C/24h	0,277	21	0,579	44	52,9	81,7	
CoCrTa-5+C	1200°C/2h + 1000°C/10h	0,37	28	0,751	57	36,5	49,6	CoCrTa-5 with carbides addition (best results)
	1200°C/2h + 1000°C/10h	0,445	34	0,728	55	36,1	48,5	
	1200°C/24h	0,401	31	0,692	53	34,3	48,9	
	1200°C/24h	0,417	32	0,702	54	39,9	45,8	
CoCrTa-6	1200°C/24h	0,214	16	0,539	41	79,4	91,1	large elongation, reduced mechanical properties compared to ref
	1200°C/24h	0,249	19	0,457	35	151,1	93,4	
CoCrTa-8	1200°C/24h	0,245	19	0,632	48	28,1	46,5	
	1200°C/24h	0,228	17	0,628	48	41,5	41,7	

The investigation into the 0.2% proof stress, symbolizing yield strength, in other words, the stress at which plastic deformation initiates, reveals significant discrepancies, offering pivotal insights into the materials' behavior. Noteworthy distinctions also emerge concerning the maximum load before rupture (i.e., ultimate load) and, alternatively, the tensile stress before rupture (i.e., ultimate stress). More importantly, the reference material exhibits markedly

superior values for elongation. Conversely, CoCrTa materials showcase significantly heightened elongation values, particularly exemplified by CoCrTa-6 reaching up to 151%, in contrast to the reference material's 27.9%. This comprehensive analysis contributes valuable insights into the mechanical characteristics of the materials under investigation.

Furthermore, these tests have highlighted that samples with excessively high Cr concentrations become brittle at room temperature and easily deform at 1200 °C. Thus, it is evident that the Cr content of 37.6 at.% in the CoCrTa-6 composition is already too high for spinner development, despite the crucial importance of this element for high-temperature oxidation resistance.

However, as discussed in this section, the addition of carbides has a beneficial effect. The maximum load is much closer to those of the reference material, ranging between 0.692 and 0.751 kN for CoCrTa-5+C, compared to the values between 0.628 and 0.739 kN for the reference material. Moreover, the CoCrTa+C alloys exhibit reduced elongations, averaging 36%, much closer to the reference material, which has an average of 24%. On the other hand, the tests conducted here did not reveal any significant influence on the mechanical properties.

With the confirmation that the addition of carbide does not negatively impact oxidation resistance at 1200 °C for CoCrTa alloys, this addition appears extremely promising for identifying an optimal composition for fiberglass spinning development. Therefore, building upon the previously obtained results and incorporating this new information, it can be noted that the ideal composition of CoCrTa for achieving a balanced combination of mechanical properties and high-temperature oxidation resistance should include:

- Chromium content between 32 at% and 37 at%

- Tantalum at a minimum of 7 at%

- Addition of a minimum of 3.3 at% carbon.

5.3. Vickers hardness as a function of temperature of CoCrTa alloys with and without carbon

Finally, to delve deeper into the behavior of CoCrTa and CoCrTa+C samples under varying temperatures and compare them to the reference material, additional Vickers hardness measurements were meticulously conducted in-situ at different temperatures, spanning up to 1200 °C, as illustrated in Fig. 5.11.

Upon scrutiny of this figure, it becomes apparent that the Vickers hardness values for all tested samples exhibit a similar trend and fall within the same range. At room temperature, the Vickers hardness initially ranges between 300 and 350 Hv. A linear decrease is then observed, reaching approximately 200 to 250 Hv at 650 °C, before experiencing a sharp decline at temperatures exceeding 650 °C.

In the specific context of a cobalt-based superalloy, such as the reference material, this critical temperature typically corresponds to the stability limit of the gamma prime phase that constitutes the material. For CoCrTa alloys, it is plausible to assume that this abrupt decrease may be linked to the onset of the melting of one of the constituent phases.
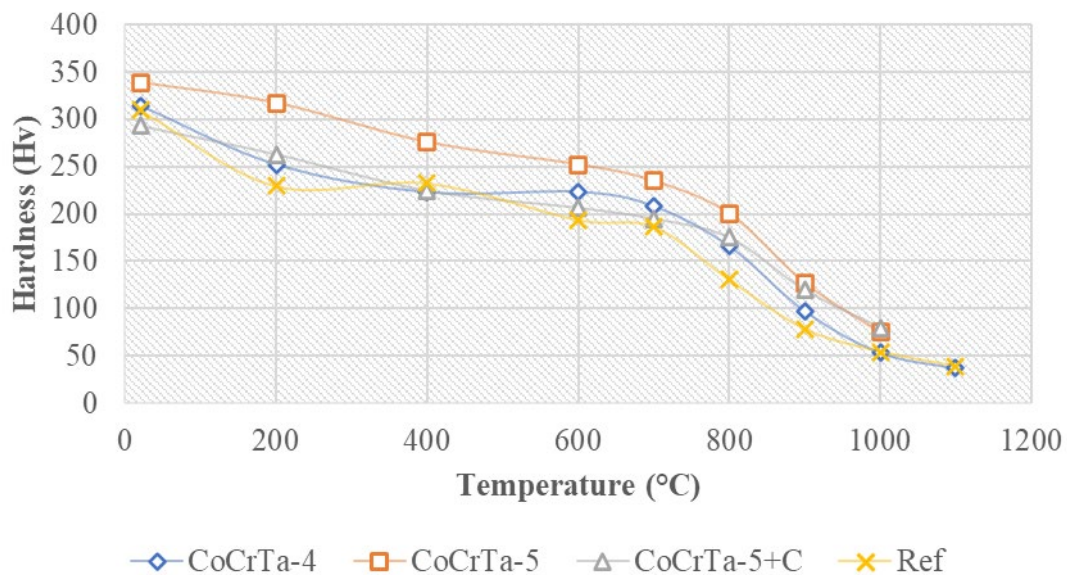

Figure 5.11. Vickers hardness as a function of temperature of samples CoCrTa, CoCrTa+C and reference material.

These observations underscore the sensitivity of hardness properties to temperature and provide meaningful insights into microstructural changes and phase transitions occurring in CoCrTa alloys at elevated temperatures. These findings enhance our overall understanding of the mechanical behavior of these materials, offering valuable perspectives for targeted adjustments and optimisations tailored to specific applications requiring mechanical performance under extreme temperature conditions.

5.4. Summary

The thorough investigation into the mechanical properties of Co-Cr-Ta ternary alloy systems at elevated temperatures has provided valuable insights into their applicability for high-speed spinner applications, particularly in the realm of fiberglass manufacturing. The study, spanning from alloy production to microstructural analyses and tensile testing, has elucidated crucial aspects of the alloys' behavior, emphasizing both promising oxidation resistance and challenges related to brittleness at room temperature, as observed in compositions such as CoCrTa-6.

The incorporation of carbides into CoCrTa-5 has surfaced as a promising strategy, demonstrating stable presence of carbide after oxidation and notable improvements in mechanical properties at 1200 °C. This addition not only transformed plastic deformation profiles but also brought the overall mechanical performance closer to that of the reference material.

Looking forward to avenues for further refinement and optimisation are worth exploring. One intriguing prospect involves the addition of other elements, specifically rhenium, to enhance high-temperature mechanical properties. Rhenium has exhibited promising attributes in similar alloy systems, contributing to improved strength and stability at elevated temperatures. The synergistic effects of incorporating rhenium, possibly in combination with

carbides, present a compelling direction for research, aiming to achieve an optimal balance between high-temperature stability and mechanical resilience in the demanding context of high-speed spinning applications. This challenge is investigated in the next chapter.

Chapter 6: Effect of Re addition on high temperature performance of Co-Cr-Ta-Ti-C-Re alloys . [95]

6.1. Preparation of Co-Cr-Ta-Ti-C-Re alloys

Table 6.1 lists the alloys in this study. As the main element for high temperature application, Co was selected. To improve the oxidation resistance, Cr was added, as discussed in Chapter 4. Then for the formation of carbides, Ti and Ta were added to strengthen the alloys, as described in Section 5.2.2. The composition of Re-0 was determined from the literature [96, 97]. Rhenium was added up to 15 at.% in exchange of cobalt to examine its effect on microstructure and oxidation behavior. The alloys were produced using the arc melting method in the way that was explained in Section 1.3.2. The alloy buttons were heat-treated at at 1200 °C for 2 h in a sealed in quartz ampoules under argon to dissolve carbide. Subsequently, they were then annealed at 1000 °C for 10 h to achieve a uniform microstructure.

Table 6.1. Composition of the alloys investigated in this study [95]. Table 6.1 is adapted from the table in Coatings 14 (2024) 26, by Moreau Louis Etienne, Banoth Santhosh, Akira Ishida, Murakami Hideyuki.

Alloys	Co (at.%)	Cr (at.%)	Re (at.%)	Ta (at. %)	Ti (at.%)	C (at.%)
Re-0	58.8	27		1.7	6.4	6.1
Re-5	53.8	27	5	1.7	6.4	6.1
Re-10	48.8	27	10	1.7	6.4	6.1
Re-15	43.8	27	15	1.7	6.4	6.1

6.2. Results and discussion
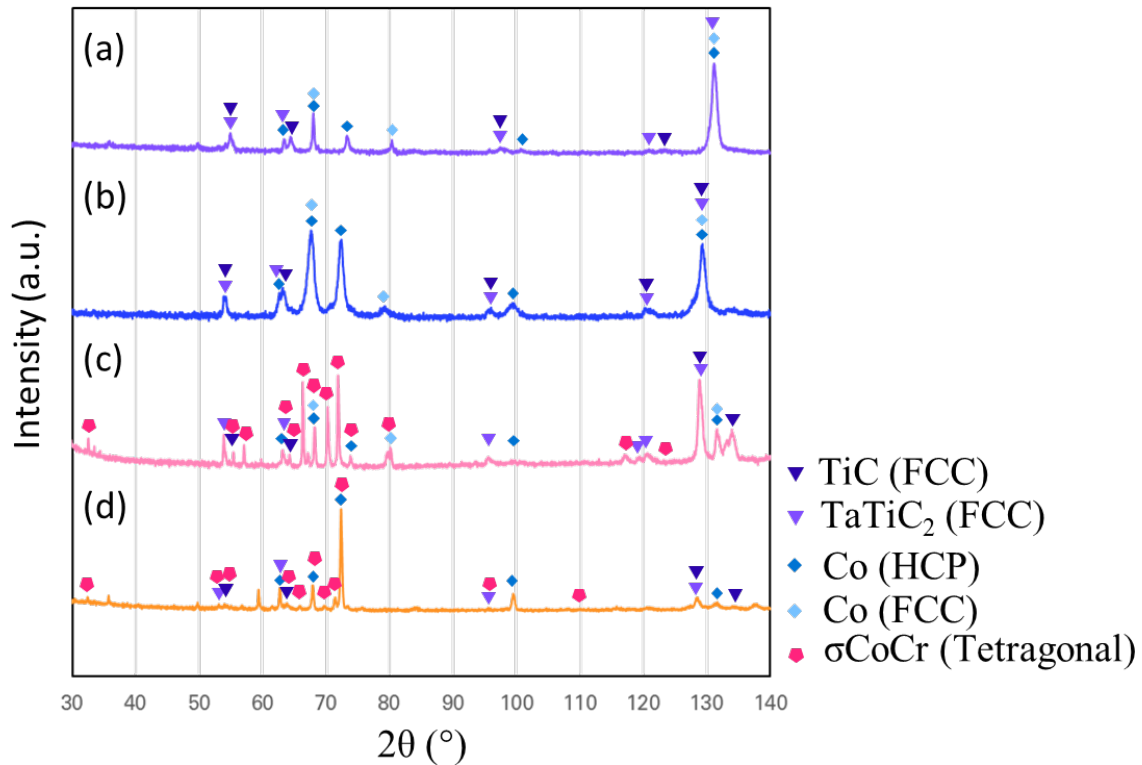
6.2.1. Microstructure

Figure 6.1. X-ray diffraction patterns of (a) Re-0, (b)Re-5, (c)Re-10, and (d)RE-15 prepared by casting followed by annealing at 1200 °C for 24 h [95]. Figure 6.1 is adapted from the figure in Coatings 14 (2024) 26, by Moreau Louis Etienne, Banoth Santhosh, Akira Ishida, Murakami Hideyuki.

The X-ray diffraction patterns of the cast Co-Cr-Re-Ta-Ti-C alloys after the heat treatment are displayed in Fig. 6.1. All the alloys have basically three FCC phases and one HCP phase, which are attributable to TiC, $TaTiC_2$, α-Co, and ε-Co phases, respectively. In addition, peaks from σ-CoCr tetragonal phase are discerned in alloys Re-10 and Re-15.

Figure 6.2 presents the microstructures (BSE images) of the cast alloys annealed at 1200 °C for 24 h, and Table 6.2 summarizes the corresponding EDS analysis for each phase present in Fig. 6.2. All cast alloys exhibit dendritic microstructures after annealing at 1200 °C. The microstructure of Re-0and Re-5 (Fig. 6.2(a), (b), (e), (f)) consists of two Co-rich phases (darker region) as the matrix phase, and a star-like (Ta, Ti)-rich carbides observed as a grey region, and

Ti-rich carbides in black colour. The morphological features of the (Ta, Ti)-rich carbides seems to be formed by the agglomeration of some carbides, and the carbide size decreases as Re content increases. The isolated carbides are further discernable in Re-5. In Re-10 and Re-15, the carbides are arranged in a row. An increase of the Re content from Re-5 to Re-15 (Fig.
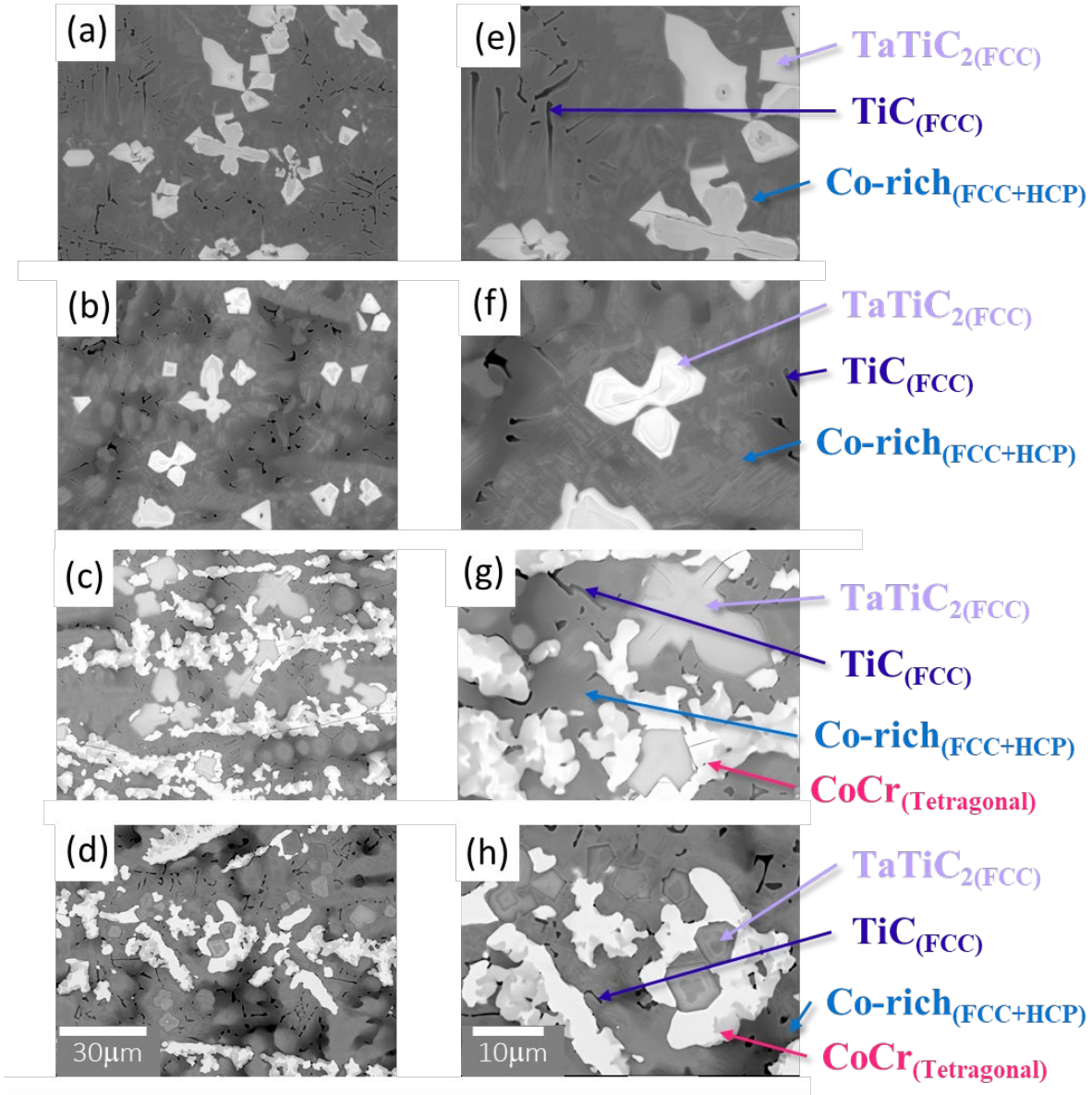

Figure 6.2. BSE images of studied alloys prepared by casting followed by annealing at 1200 °C for 24 h: (a), (b), (c), and (d) low magnification images of Re-0. Re-5. Re-10, and Re-15, respectively, and (e), (f), (g), and (h) high magnification images of precipitates. In Re-0, Re-5, Re-10, and Re-15, respectively [95]. Figure 6.2 is adapted from the figure in Coatings 14 (2024) 26, by Moreau Louis Etienne, Banoth Santhosh, Akira Ishida, Murakami Hideyuki.

Table 6.2. Composition of the phases observed in the Co-Cr-Re-Ta-Ti-C alloys prepared by casting followed by annealing at 1200 °C for 24 h (see Fig. 7.2) [95]. Table 6.2 is adapted from the table in Coatings 14 (2024) 26, by Moreau Louis Etienne, Banoth Santhosh, Akira Ishida, Murakami Hideyuki.

Phases	Co	Cr	Re	Ta	Ti	C
Re-0	**58.8**	**27**	**0**	**1.7**	**6.4**	**6.1**
Dark grey region (HCP+FCC)	64.1	26.6	/	0.04	1.9	4.6
Black region (FCC)	28.7	15.7	/	4.5	29.3	21.9
Light grey region (FCC)	2.1	4.0	/	19.6	47.1	27.1
Re-5	**53.8**	**27**	**5**	**1.7**	**6.4**	**6.1**
Dark grey region (HCP+FCC)	60.1	27.8	2.8	0.3	3.2	5.7
Black region (FCC)	18.5	10.9	0.4	9.7	38.9	21.9
Light grey region (FCC)	2.5	1.6	/	27.7	41.1	27.1
Re-10	**48.8**	**27**	**10**	**1.7**	**6.4**	**6.1**
Dark grey region (HCP+FCC)	61.8	24.3	4.4	0.3	2.6	6.6
Black region (FCC)	23.8	13.9	2.4	8.4	29.2	22.4
Light grey region (FCC)	3.9	2.5	/	22.3	44.2	27.0
White region (tetragonal)	42.4	31.7	10.6	1.4	6.2	7.6
Re-15	**43.8**	**27**	**15**	**1.7**	**6.4**	**6.1**
Dark grey region (HCP+FCC)	62.4	21.1	8.7	0.3	1.4	6.0
Black region (FCC)	19.1	9.5	2.8	8.3	35.8	24.5
Light grey region (FCC)	1.8	1.5	/	24.8	44.7	27.1
White region (tetragonal)	39.2	29.5	20.8	0.8	2.4	7.2

6.2(b)-(d), (f)-(h)) results in a reduced volume fraction of the Co (FCC and HCP) phase and instead the formation of an additional CoCr tetragonal phase. The matrix phase of the alloys was considered to be a mixture of Co HCP (ε phase) and Co FCC (α phase) phases through XRD, EDS, and BSE characterization. TaTiC$_2$ (FCC, a=4.387Å) and TiC (FCC, 4.328 Å) were identified as (Ta, Ti)-rich carbides. The presence of a CoCr σ phase was confirmed as a tetragonal phase in the Re-10 and Re-15 alloys.

The predicted phase constitutions of the Co-Cr-Re-Ta-Ti-C alloy system at1200 °C, obtained using Pandat 2020 software with the PanNi2020 database, were compared with experimental results for microstructure and phase composition, as shown in Fig. 6.3. While there were some differences, the predicted phase compositions are consistent with the
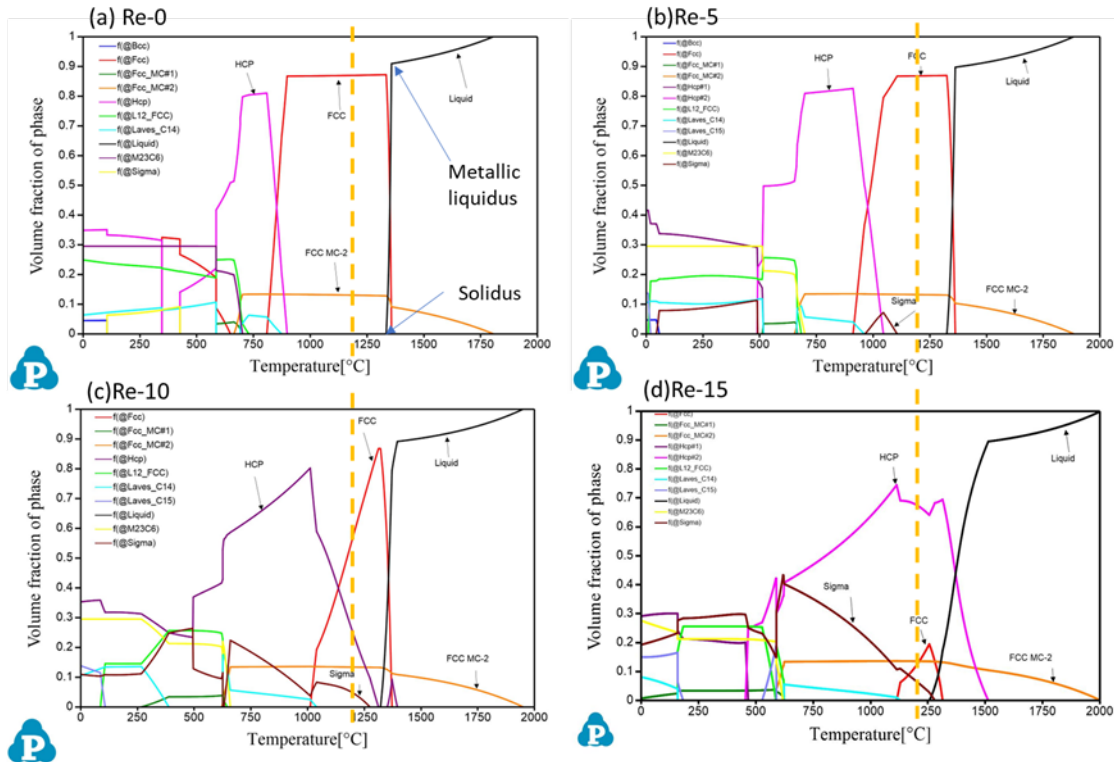
Figure 6.3. Predicted phase diagrams of (a) Re-0, (b) Re-5, (c) Re-10, and (d) Re-15 derived from Pandat 2020 software with Pan-Ni 2020database. Dashed lines indicate the phases at 1200 °C [95]. Figure 6.3 is adapted from the figure in Coatings 14 (2024) 26, by Moreau Louis Etienne, Banoth Santhosh, Akira Ishida, Murakami Hideyuki.

experimental results in principle. The alloys consisted of a Co FCC phase and TaTiC$_2$ (FCC) and TiC (FCC) carbide phases.

Additionally, an HCP phase was detected in all of the alloys, as depicted in Fig. 6.2 and Table 6.2, despite its absence in the anticipated phase diagrams for Re-0 and Re-5 at 1200 °C. Simulations suggest that this phase forms at 900 °C for Re-0 and at 1040 °C for Re-5. Therefore, it is likely that the HCP phase in Re-0 and Re-5 was formed during the air-cooling process following the heat treatment, This explains the presence of the HCP phase, which was not predicted to exist at 1200 °C in Re-0 and Re-5 in the equilibrium state.

This study also predicts the presence of the σ phase in Re-10 and Re-15 alloys, which corresponds to the CoCr tetragonal phase observed in Fig. 6.2. It is expected that the volume fraction of the sigma phase will significantly increase by adding rhenium up to 10% for Re-15,

which is consistent with the BSE results (Fig. 6.2(c), (d), (g), and (h)). Based on the phase predictions, the amount of TaTiC$_2$ carbides remains almost constant over the range of alloy composition from Re-0 to Re-15, which is in good agreement with the observations in Fig. 6.2.

However, increasing the Re content of the alloys resulted in a higher temperature at which the Co-rich FCC phase forms and thereby a lower volume fraction of the Co-rich FCC phase in favor of the HCP phase. Further observations are required to validate this trend of phase formation with temperature. It is important to note that the thermodynamic database (PanNi-2020) used in this study is optimized for Ni-based alloys. Despite this limitation of the database, the present predictions are likely to be able to predict the phase constitution of the samples after heat treatment at 1200 °C. Predictive tools like Pandat demonstrate promise in optimizing the composition and microstructure of complex alloys in the future.

6.2.2. Melting temperature

The diagrams in Fig. 6.3 not only provide equilibrium phase constitution based on temperature but also predict the temperature at which a certain phase transformation takes place. Therefore, prediction of the melting temperatures of the Co-Cr-Ta-Ti-C alloys can be performed by the CALPHAD method. As shown in Fig. 6.3, the solidus temperature gradually decreases with increasing Re addition from 0 to 10 at.%. The solidus temperatures for Re-0, Re-5, and Re-10 were found to be 1334.1 °C, 1324.8 °C, and 1321.2 °C, respectively. The addition of 15 at.% Re is predicted to significantly decrease the solidus temperature to 1255.9 °C.

Differential thermal analysis (DTA) was used to measure the liquidus and solidus temperatures for each alloy composition [98]. The DTA samples were cylindrical with a diameter of approximately 3 mm. The sample was heated from room temperature to 1550 °C and then cooled at a heating/cooling rate of 10 °C/min in a flowing Ar atmosphere.
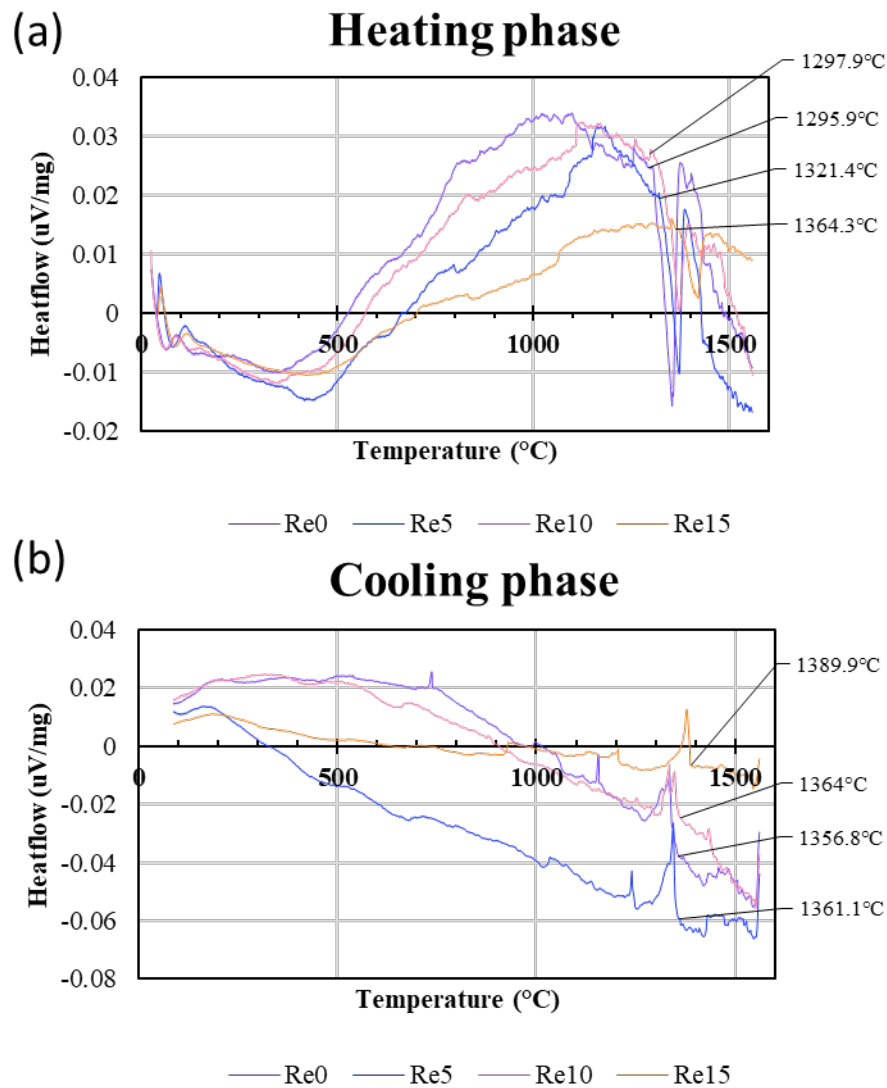
Figure 6.4. DTA heat flow curves of Co-Cr-Re-Ta-Ti-C alloys: (a) from room temperature to 1550 °C and (b) from 1550 °C to room temperature[95]. Figure 6.4 is adapted from the figure Coatings 14 (2024) 26, by Moreau Louis Etienne, Banoth Santhosh, Akira Ishida, Murakami Hideyuki.

Figure 6.4 displays the heat flow curves of the Co-Cr-Re-Ta-Ti-C alloy system obtained by the DTA meassurement, during (a) heating from room temperature to 1550 °C, and (b) cooling from 1550 °C to room temperature. The heat flow, which was measured by the temperature difference between the sample and the reference, increases as the sample temperature rises and melting begins. Therefore, an endothermic reaction such as melting is indicated as a negative drop in the heat flow curve. After the melting process is completed, the heat flow curve rapidly returns to the baseline.

However, the exothermic reaction in the samle is represented by a positive change in the heat flow from the sample to the reference , which is displayed as a positive peak in the heat flow curve [38]. These alterrations in the heat flow curves can be utilized to ascertain the phase transformation and reaction temperatures.

The temperature at which melting begins in the Co-Cr-Re-Ta-Ti-C samples, known as the 'solidus temperature', can be estimated by observing the onset point of the endothermic peak during the heating phase. The results indicate that the solidus points of Re-0, Re-5 and Re-10 are 1295.9 °C, 1321.4 °C, and 1297.9 °C, respectively. This suggests that the addition of up to 10 at.% Re does not significantly alter the solidus temperature of the alloys, which is in agreement with the Pandat predictions. However, the solidus temperature is significantly increased (to 1364.3°C) with the addition of 15 at.% Re.

In turn, the temperature at which the sample begins to solidify can be determined by observing the onset of positive change in the heat flow curve during the cooling stage. This point corresponds to the point in the calculated phase diagrams in Fig. 6.3 where the volume fraction of the liquid phase abruptly stops increasing, as indicated by the arrows in Fig. 6.3(a). Above this point, all the metallic phases completely melt, and therefore it is termed as a "metallic liquidus point" in this study. The metallic liquidus points assigned in the DTA analysis were 1356.8, 1361.1, and 1364 °C for Re-0, Re-5, and Re-10, respectively. There was no significant difference between 0 and 10 at.% of Re. The liquidus temperature increased to 1389.9°C with further addition of Re (15 at.%).

Figure 6.5(a) shows the comparison of the solidus temperatures measured using DTA (Fig. 6.4) and the predicted values shown in Fig. 6.3 in order to assess the reliability of the prediction software and the database. The experimental and predicted values show reasonable agreement from Re-0 to Re-10, as indicated by a small difference of 38.2 °C, 3.4 °C and 23.3
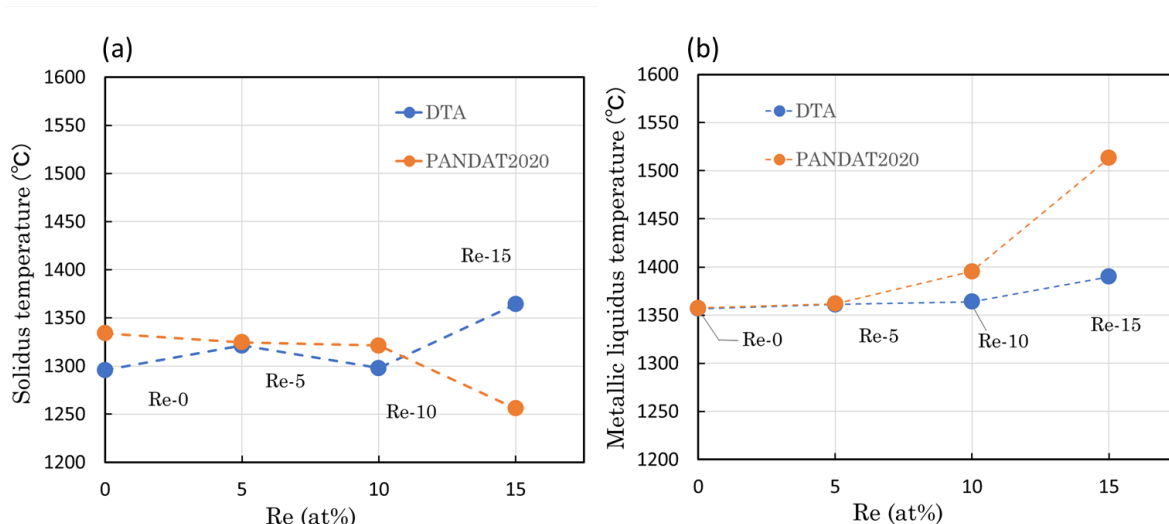
Figure 6.5. Comparison of melting temperatures experimentally determined by DTA and predicted by Pandat software: (a) solidus temperature and (b) metallic liquidus temperature [95]. Figure 6.5 is adapted from the figure Coatings 14 (2024) 26, by Moreau Louis Etienne, Banoth Santhosh, Akira Ishida, Murakami Hideyuki.

°C for Re-0, Re-5, and Re-10, respectively. However, the Re-15 with the highest Re content of 15 at.% exhibited a significant discrepancy of 108.4 °C between the measured and predicted temperatures. The predicted temperature of this sample is lower than any of the other samples. Both the metallic liquidus temperatures obtained from the experiment and simulation show similar trends with Re content, i.e., they increase with the amount of Re addition. It is noteworthy that there is an excellent agreement for Re-0 and Re-5 within 1 °C of deviations. However, the difference significantly increases with the Re content; Re-15 exhibits an experimental temperature lower than the predicted one by 123.4 °C, whereas the difference of Re-10 is 31.5 °C.

For both the solidus and metallic liquidus temperatures, the experimental and predicted temperatures show a good agreement up to 10 at. % Re addition, but exhibit a significant discrepancy above 10 at.% Re. The metallic liquidus temperature was predicted to be higher, while the solidus temperature was predicted to be lower. The calculation predicts that the initial solidification of the metallic phase in Re-15 will occur in the Re-rich HCP phase. The lower solidus point in Re-15 can be explained by the eutectic reactions at low temperature. However,

when the Re content exceeds 10 at. %, the eutectic reaction was not observed through microstructural analysis or DTA measurement. This suggests a discrepancy between the experimental results and Pandat predictions.

However, there was excellent agreement between the predicted values from the Pandat calculations and the experimental results for Re-0 and Re-5, which suggests the applicability of the simulation tool for phase prediction. To enhance the accuracy of the predictions, further experiments in the Co-Cr-Ta-Ti-Re-C alloy system could be conducted, particularly for alloys with a higher amount of alloying elements such as Ta, Ti, and Re.

6.2.3. Oxidation resistance at 1200 °C

To characterise the microstructural changes of the alloys after oxidation, small samples were oxidised at 1200°C in air for 20 hours. The samples were placed on an Al2O3 plate and then put into the furnace until the target temperature was reached. After 20 hours of oxidation, the samples were taken out of the muffle furnace and air cooled to room temperature. The mass of the samples, excluding the spalled oxides, was measured using an electric balance, and mass changes were evaluated.

Figure 6.6(a) displays the morphological appearances of the samples after 20 hours of oxidation at 1200°C, along with the spalled oxides that remained on the Al_2O_3 plate (Fig. 6.6(b)). The photographs indicate a blue-colored halo on the alumina plate, suggesting the formation, evaporation, and deposition of a large amount of the blue-ish oxide, mainly a Co-rich oxide. The alloys Re-0, -5, and -10 exhibit similar amounts of spalled oxide in the form of a powder that has spalled from the samples. In contrast, the Re-15 alloy exhibits a greater amount of spalled oxide in both powder and solid forms. To compare the oxidation behavior of the samples semi-quantitatively, the mass change per surface area ($\Delta m/S$) was estimated, where the surface area "S" is defined as $S = S_{Top\ Suraface} + S_{Side\ Surface}$. The results are summarized in Fig.
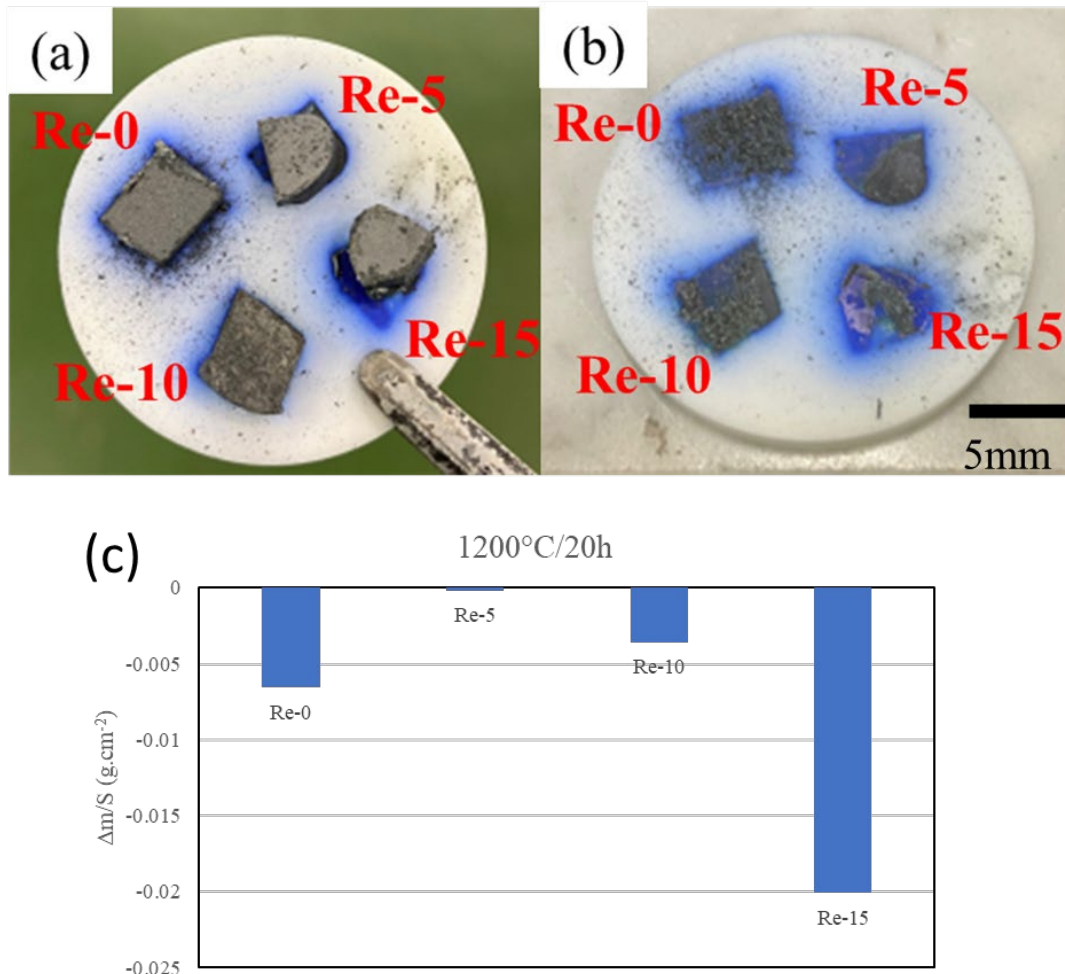
Figure 6.6. (a) Appearance of the alloys oxidized at 1200 °C for 20 h followed by air cooling, (b) oxides spalled and deposited on the alumina plate, and (c) mass changes of the alloys per exposed surface area [95]. Figure 6.6 is adapted from the figure Coatings 14 (2024) 26, by Moreau Louis Etienne, Banoth Santhosh, Akira Ishida, Murakami Hideyuki.

6.6(c). It is important to notice that in this test, the sample mass does not include the spalled oxides left on the Al_2O_3 plate. Figure 6.6(c) illustrates that Re-15 experienced a considerable reduction in surface oxide (-0.02 g/cm^2) in comparison to the other alloys. This suggests the poor oxidation resistance, possibly due to evaporation or spallation.

Figure 6.7 displays XRD profiles of the alloys' top surface after 20 h of oxidation at 1200°C. All the alloys exhibit two FCC oxide phases, an HCP oxide phase, and a tetragonal oxide phase. Two additional oxide phases: a Cr and Re-rich tetragonal and a Re-rich cubic-
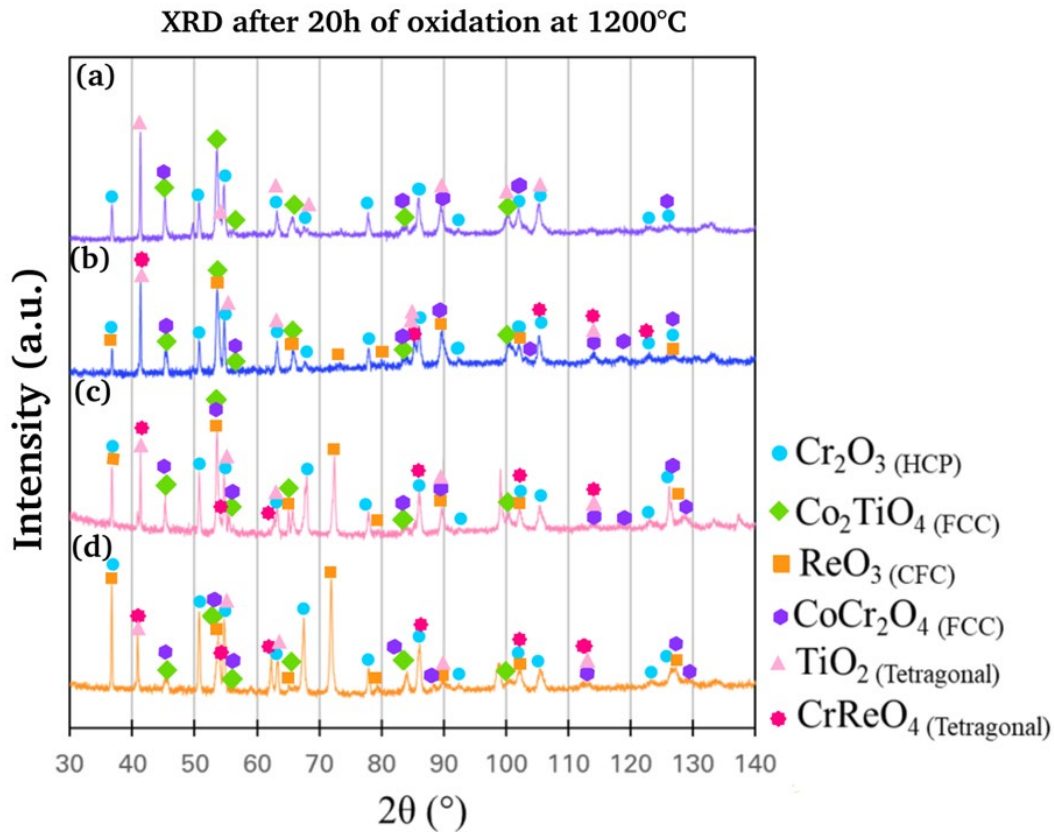
Figure 6.7. XRD profiles of the top surfaces of samples after oxidation for 20 h at 1200 °C: (a) Re-0, (b) Re-5, (c) Re-10, and (d) Re-15 [95]. Figure 6.7 is adapted from the figure in Coatings 14 (2024) 26, by Moreau Louis Etienne, Banoth Santhosh, Akira Ishida, Murakami Hideyuki.

centered oxide phase were formed by the addition of 5 at.% of Re. The peaks from the diffraction of the Re-rich oxide at 37.05° (corresponding to the 200 diffraction), 72.93° (corresponding to the 321 diffraction), and 127.94° (corresponding to the 440 diffraction) all increases in intensity.

Cross-sectional analyses using BSE and EDS were carried out to identify the formed oxides, as summarized in Fig. 6.8. In all the alloys, the presence of Cr_2O_3 (shown as the green-colored region in the elemental mapping in Fig. 6.8) is observed, but its volume fraction drastically decreases in Re-15. Moreover, increasing Re-content seems to promote internal oxidation, indicating reduced protection against oxidation at 1200 °C. Considerable CoO (shown in orange in Fig. 6.8) is observed in Re-5, Re-10, and Re-15. Above the Cr_2O_3 layer,
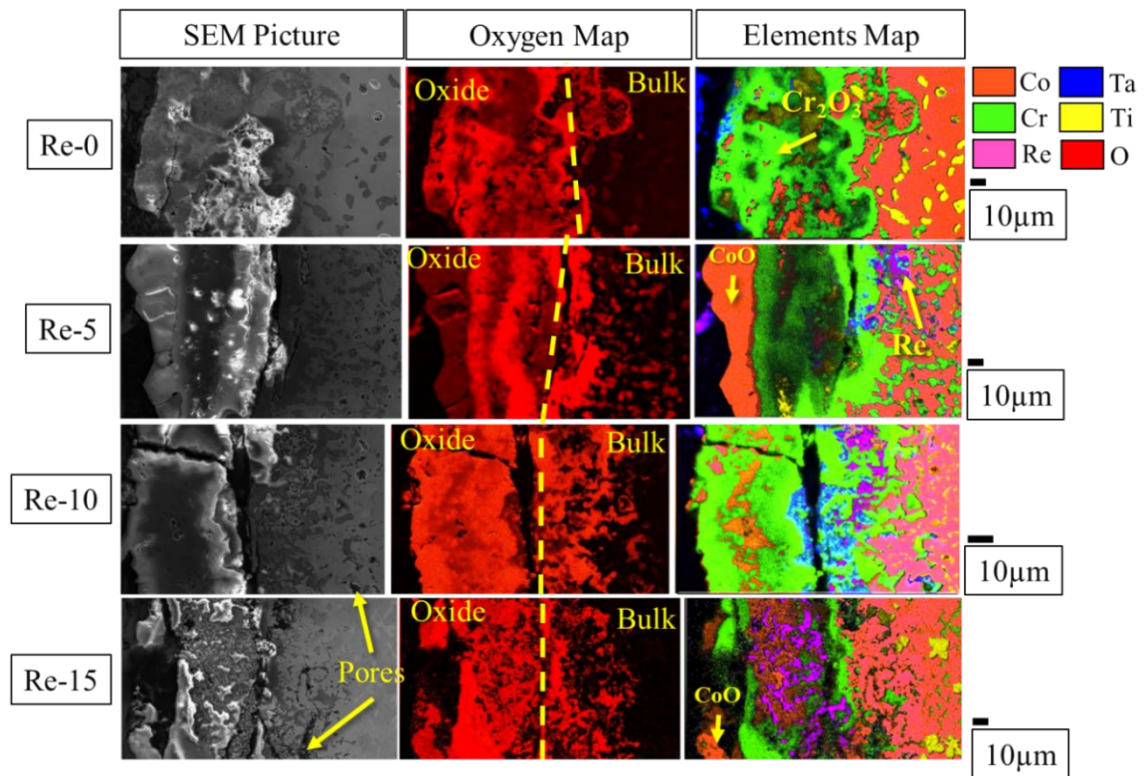
Figure 6.8. Cross sectional micrographs of alloys after oxidation for 20 h at 1200 °C and corresponding oxygen and elements mapping by EDS [95]. Figure 6.8 is adapted from the figure in Coatings 14 (2024) 26, by Moreau Louis Etienne, Banoth Santhosh, Akira Ishida, Murakami Hideyuki.

the oxide is present in Re-5, but it is mixed with Cr_2O_3 in Re-10. In Re-15, the Co oxide is present on both the top surface and in the mixed oxide layer of Cr, Re, and Co. It should be noted that the Co oxide is not protective, as it usually forms with the porous layer, which cannot retard the oxidation. The formation of porous oxides does not effectively prevent the ingress of oxygen, which in turn hinders the formation of a continuous protective Cr_2O_3 layer.

The Re oxide is volatile [99, 100], therefore Re can be preferentially evaporated when Re-containing alloys are exposed in air at high temperature. This is supported by the absence of Re oxides in Fig. 6.8. The continuous evaporation of Re oxide promotes the formation of pores, which in turn hinders the formation of dense and continuous protective oxides. surface oxide layers. As a result, the oxidation of other elements continuously promotes. The thinner Cr_2O_3 layer observed in Re-15 may be due to the formation of porous Cr_2O_3[101], and its

evaporation continues together with Re, owing to the high vapor pressure of their oxides. Furthermore, the oxidation of other elements such as Co, Ti, and Ta also promotes the spallation of their oxides, as shown in Fig. 6.6. The oxidation test confirmed that Re-10 and Re-15 experienced significant mass loss due to the rapid formation and subsequent evaporation of volatile oxides, as well as the formation and spallation of other oxides. In contrast, Re-5 exhibited the smallest mass change among all the investigated alloys. However, the comparison in the cross-sectional microstructure between Re-0 and Re-5 confirmed that the oxidized region is thicker in Re-5, where internal oxidation is also observed. The results indicate that Re-0 and Re-5 experienced almost identical mass loss due to the evaporation and spallation of oxides. However, the remaining oxidized region is larger in Re-5. Therefore, it can be concluded that the addition of 5 at.% Re does not necessarily enhance the oxidation resistance in this alloy system.

6.3. Summary

This chapter analyses four samples with different Re content. Microstructural analysis confirmed that all samples have Co-rich matrices (HCP and FCC phases) and $TaTiC_2$ carbide precipitates. The addition of Re above 10 at.% has a significant impact on the microstructure, resulting in the formation of the σ phase. These findings were compared to predictions made using the Pandat software. The observations aligned with the predictions, except for alloys with high levels of Re. This discrepancy is likely due to the limited data available in the PanNi2020 database for alloys with such a high amount of alloying addition. The calculated results were also used to predict melting temperatures of alloy compositions and compared to DTA results for the Co-Cr-Re-Ta-Ti-C samples. The experimental results show that the melting temperature is significantly altered with the addition of 15 at.% Re, while the addition of up to 10 at.% Re has no effect on the melting temperature. Pandat's predictions agree well with the experimental results for up to 10 at.% Re addition, but there is a significant discrepancy for Re-15.

Finally, the alloys' oxidation resistance was tested at 1200°C. The study found that an increase in the amount of Re had a negative impact on the protection against oxidation. This resulted in the formation of a large amount of porous CoO and volatile ReO_3, which caused the evaporation of protective Cr_2O_3.

Although the addition of Re does not significantly increase the melting temperature, adding more than 15 at.% does lead to a significant increase in the melting temperature. This increase is beneficial for improving high-temperature strength. However, this comes at the expense of reduced oxidation resistance because of the formation of harmful oxides and the evaporation of protective Cr_2O_3.

Conclusion

This thesis embarked on a mission to explore and enhance the properties of Co-Cr-Ta alloys, driven by the critical demand for materials capable of withstanding extreme conditions in industrial applications such as glass fiber production. Through rigorous experimental analysis and innovative material design, we have not only addressed specific needs within the glass industry but also made a broader contribution to the field of high-temperature material science.

In this research, we successfully developed a series of Co-Cr-Ta alloys, demonstrating their enhanced oxidation resistance and mechanical properties at high temperatures. The inclusion of varying amounts of rhenium in these alloys was also a significant aspect of the present research, providing insights into its effects on the microstructure and oxidation kinetics of the alloys.

The important findings obtained in this study are as follows.

• **Microstructure and Oxidation Behavior of Co-Cr-Ta alloy system:** The microstructure of Co-Cr-Ta alloys was characterized by a Co-rich phase (a mixture of FCC and HCP phases) and a Co_2Ta-based C15 Laves phase. As the Cr content increases above 36 at.%, a tetragonal σ-phase precipitates. When the Cr/Ta atomic ratio is within the range of 4 to 7, the formation of a stable and continuous $CrTaO_4$ oxide layer emerged as a pivotal factor in enhancing the oxidation resistance of these alloys at temperatures up to 1200 °C.

• **Addition of carbides to Co-Cr-Ta alloys:** Incorporation of carbides into the Co-Cr-Ta alloy improved the mechanical properties, showing a high ultimate stress and a small elongation at 1200 °C, without deficiency in oxidation resistance.

• **Re addition to the Co-Cr-Ta-Ti-C-Re alloys:** Co-Cr-Ta-Ti-C-Re alloys were composed of a Co-rich matrix (HCP and FCC phases) with $TaTiC_2$ carbides in it, basically, in agreement with

the predictions by a Pandat software with PanNi2020 database. Addition of 15 at.% Re significantly increased the melting point of the alloy, indicative of a potential effect in increasing high temperature strength, but this excessive addition deteriorated their oxidation resistance due to the formation of volatile ReO_3. Optimizing the composition of multielement alloys with the help of thermodynamic calculation software could be helpful to explore new alloys with this delicate combination of mechanical properties and oxidation resistance,

• **Machine Learning Insights:** The use of Machine learning methods in predicting alloy compositions conducive to better oxidation resistance at 1200 °C was found to be an effective approach to explore new alloys. This data-driven design not only streamlined the material development process but also highlighted the potential of predictive modeling in material science.

• **Challenges and Limitations:** Despite significant advancements, challenges such as the formation of brittle sigma phases in certain compositions and the need for a delicate balance in alloying elements to prevent detrimental oxide formation were encountered. These findings underscore the complexity of designing alloys for specific high-temperature applications.

Our research offers promising avenues for the glass fiber industry, particularly in enhancing the durability and performance of spinner tools used in fiber production. The improved high-temperature mechanical strength and oxidation resistance of the developed Co-Cr-Ta alloys present opportunities for more efficient and sustainable industrial processes.

Future directions to put the experimental alloys in practice are considered to involve the following approaches.

(1) Exploring additional alloying elements: Future research could explore the inclusion of other elements to further enhance the properties of these alloys. The potential for

developing high entropy alloys as a new alloy type presents an exciting avenue for surpassing the current limitations of Co-based alloys.

(2) In-depth mechanical characterization: Further mechanical testing, particularly at elevated temperatures, is crucial to fully ascertain the suitability of these alloys for industrial applications.

(3) Scaling and industrial Testing: Scaling the production of these optimised alloys and conducting real-world industrial testing will be vital in transitioning from laboratory research to practical applications.

Finally, this thesis has successfully bridged the gap between the existing limitations of high-temperature materials and the demanding requirements of industrial applications. The innovative approaches and findings presented here not only contribute to the advancement of material science but also pave the way for future research in this critical field.

References

[1] C. Baley, A. Bourmaud, P Davies, Eighty years of composites reinforced by flax fibres: A historical review, Composites Part A: Applied Science and Manufacturing 144 (2021) 106333. https://doi.org/10.1016/j.compositesa.2021.106333.

[2] A. Diniță, R.G. Ripeanu, C.N. Ilincă, D. Cursaru, D. Matei, R.I. Naim, M. Tănase, A.I. Portoacă, Advancements in fiber-reinforced polymer composites: A comprehensive analysis, Polymers 16(2024) 2. https://doi.org/10.3390/polym16010002.

[3] H. Sharma, A. Kumar, S. Rana, N.G. Sahoo, M. Jamil, R. Kumar, S. Sharma, C. Li, A. Kumar, S.M. Eldin, M. Abbas, Critical review on advancements on the fiber-reinforced composites: Role of fiber/matrix modification on the performance of the fibrous composites, Journal of Materials Research and Technology 26 (2023) 2975-3002. https://doi.org/10.1016/j.jmrt.2023.08.036.

[4] J. Singh, M. Kumar, S. Kumar, S.K. Mohapatra, Properties of Glass-Fiber Hybrid Composites:A Review, Polymer-Plastics Technology and Engineering 56(2017) 455-469. DOI: 10.1080/03602559.2016.1233271.

[5] T. Deák, T. Czigány, Chemical Composition and Mechanical Properties of Basalt and Glass Fibers: A Comparison, Textile Research Journal 79(2009) 645-651. https://doi.org/10.1177/0040517508095597.

[6] S.-Y. Fu, B. Lauke, E. Mäder, C.-Y. Yue, X. Hu, Tensile properties of short-glass-fiber- and short-carbon-fiber-reinforced polypropylene, Composites 31(2000) 1117-1125. https://doi.org/10.1016/S1359-835X(00)00068-3.

[7]   A. Cevahir, Glass fibers, In M. Özgür Seydibeyoğlu, A. K. Mohanty, M. Misra (Eds.), Fiber Technology for Fiber-Reinforced Composites, Woodhead Publishing, 2017, pp. 99-121. https://doi.org/10.1016/B978-0-08-101871-2.00005-9.

[8]   F.R. Jones, N.T. Huff, The structure and properties of glass fibers, in A. R. Bunsell (Ed.), Handbook of Properties of Textile and Technical Fibres (Second Edition), Woodhead Publishing, 2018, pp. 757-803. https://doi.org/10.1016/B978-0-08-101272-7.00019-5.

[9]   P.K. Gupta, STRENGTH OF GLASS FIBERS, in M. Elices, J. Llorca (Eds.), Fiber Fracture, Elsevier Science Ltd., 2002, pp. 127-153. https://doi.org/10.1016/B978-008044104-7/50008-3.

[10] Q. Zu, M. Solvang, H. Li, Commercial Glass Fibers, in H. Li (Ed.), Fiberglass Science and Technology, Springer, 2021. https://doi.org/10.1007/978-3-030-72200-5_1.

[11] W. Zhang, X. Zhang, Z. Qin, Z, Y. Wu, W. Zhang, R. Yang, High-transparency polysilsesquioxane/glycidyl-azide-polymer resin and its fiberglass-reinforced composites with excellent fire resistance, mechanical properties, and water resistance, Composites Part B: Engineering 219(2021), 108913. https://doi.org/10.1016/j.compositesb.2021.108913.

[12] D. Christie, C. Reid, D. McLaren, Applications of fiberglass reinforced plastics in the pulp & paper industry, Proceedings of CORROSION 98, San Diego, California,1998.

[13] C. Barile, C. Casavola, F. De Cillis, Mechanical comparison of new composite materials for aerospace applications, Composites Part B: Engineering 162(2019) 122-128. https://doi.org/10.1016/j.compositesb.2018.10.101.

[14] K. Liao, C.R. Schultesiz, D.L. Hunston, L.C. Brinson, Long-term durability of fiber-reinforced polymer-matrix composite materials for infrastructure applications: A review, Journal of Advanced Materials 3(1998) 3-40.

[15] R.R. Boyer, J.D. Cotton, M. Mohaghegh, R.E. Schafrik, Materials considerations for aerospace applications, MRS Bulletin 40(2015) 1055-1066. https://doi.org/10.1557/mrs.2015.278.

[16] W.L. Kelly, High modulus, structural fiberglass reinforced RIM for automotive components, SAE Transactions 94 (1985) 992-995. http://www.jstor.org/stable/44724099.

[17] V. Gheorghe, M.L. Scutaru, V.B. Ungureanu, E. Chircan, M. Ulea, New design of composite structures used in automotive engineering, Symmetry 13(2021) 383. https://doi.org/10.3390/sym13030383.

[18] K.A. Al-Sallal, Comparison between polystyrene and fiberglass roof insulation in warm and cold climates, Renewable Energy 28(2003) 603-611. https://doi.org/10.1016/S0960-1481(02)00065-4.

[19] D.K. Rajak, P.H. Wagh, E. Linul, Manufacturing Technologies of Carbon/Glass Fiber-Reinforced Polymer Composites and Their Properties: A review, Polymers 13 (2021) 3721. https://doi.org/10.3390/polym13213721.

[20] Y. Yang, Z. Chen, T. Xu, C. Wu, D.E. Awuye, Z. Chen, Comparing the uniformity of light glass fiber felt based on process improvement, microstructural forming mechanism and physical properties, Textile Research Journal 89(2019) 3447-3456. https://doi.org/10.1177/0040517518813714.

[21] A. De Meringo, Glass fibers industry: evolutions of glass composition, in Advances in Glass and Optical Materials, Proceedings of the 107th Annual Meeting of The American Ceramic Society, Baltimore, Maryland, USA, 2005, pp. 95-97.

[22] K. Katayama, M. Tsuji, Fundamentals of spinning, in T. Nakajima, K. Kajiwara, J.E. McIntyre (Eds.), Advanced Fiber Spinning Technology, Woodhead Publishing, 1994, pp. 1-24. https://doi.org/10.1533/9781845693213.1.

[23] Y. Murase, A. Nagai, Melt spinning, in T. Nakajima, K. Kajiwara, J.E. McIntyre (Eds.), Advanced Fiber Spinning Technology, Woodhead Publishing, 1994, pp. 25-64. https://doi.org/10.1533/9781845693213.25.

[24] H. Yasuda, K. Ban, Y. Ohta, Gel spinning processes, in T. Nakajima, K. Kajiwara, J.E. McIntyre (Eds.), Advanced Fiber Spinning Technology, Woodhead Publishing, 1994, pp. 172-186. https://doi.org/10.1533/9781845693213.172.

[25] J. Daviet, The Saint-Gobain Company and the Americanization of French Business. Entreprises et Histoire, 32(2003) 87-93. https://doi.org/10.3917/eh.032.0087.

[26] P. Berthod, Looking for New Polycrystalline MC-Reinforced Cobalt-Based Superalloys Candidate to Applications at 1200 °C, Advances in Materials Science and Engineering 2017(2017) 1. https://doi.org/10.1155/2017/4145369.

[27] C. Rapin, M. Vilasi, R. Podor, A. Carton, B. Gaillard-Allemand, P. Berthod, P. Steinmetz, Three Examples of High-Temperature Corrosion of Metals by Molten Glasses, Materials Science Forum 461–464(2004) 1125–1132. https://doi.org/10.4028/www.scientific.net/msf.461-464.1125.

[28] G.H. Meier, A review of advances in high-temperature corrosion, Materials Science and Engineering A 120–121(1989)(Part 1) 1-11. https://doi.org/10.1016/0921-5093(89)90712-0.

[29] G.C. Wood, High-temperature oxidation of alloys, Oxidation of Metals 2(1970) 11–57. https://doi.org/10.1007/BF00603581.

[30] G.Y. Lai, (n.d.). High temperature corrosion of engineering alloys. United States. osti: 5465166.

[31] D.L. Klarstrom, S.K. Srivastava, Selection of High Performance Alloys for High Temperature Corrosion Environments, CORROSION 2005, NACE-05421, 2005.

[32] M.H. Chopinet, The history of glass, in J. D. Musgraves, J. Hu, L. Calvez (Eds.), Springer Handbook of Glass. Springer Handbooks. Springer, Cham, 2019. https://doi.org/10.1007/978-3-319-93728-1_1.

[33] C. Sims, W. Hagel, The Superalloys. John Wiley & Sons, New York, NY, USA, 1972.

[34] E. Bradley, Superalloys: A Technical Guide, ASM International, Metals Park, Ohio, USA, 1988.

[35] M.J. Donachie, S.J. Donachie, Superalloys: A Technical Guide (2nd ed.). ASM International, Materials Park, Ohio, USA, 2002.

[36] P. Berthod, High temperature properties of several chromium-containing Co-based alloys reinforced by different types of MC carbides (M = Ta, Nb, Hf and/or Zr), Journal of Alloys and Compounds 481(2009) 746–754.

[37] G. Gudivada, A.K. Pandey, Recent developments in nickel-based superalloys for gas turbine applications. Review, Journal of Alloys and Compounds, 963(2023) 171128. https://doi.org/10.1016/j.jallcom.2023.171128.

[38] P. Král, M. Kvapilová, V. Sklenička, J. Zýka, J. Čmakal, K. Hrbáček, Microstructure and damage processes in a nickel-based alloy exposed to molten glass, Procedia Structural Integrity 23(2019) 287-292. https://doi.org/10.1016/j.prostr.2020.01.101.

[39] A. Behera, Superalloys, in Advanced Materials. Springer, Cham, 2022. https://doi.org/10.1007/978-3-030-80359-9_7.

[40] J. Cormier, Ni- and Co-Based Superalloys and their Coatings, Metals 8(2018) 1055. https://doi.org/10.3390/met8121055

[41] I.G. Akande, O.O. Oluwole, O.S.I. Fayomi, O.A. Odunlami, Overview of mechanical, microstructural, oxidation properties and high-temperature applications of superalloys, Materials Today Proceedings 43 (2021) (Part 2) 2222-2231. https://doi.org/10.1016/j.matpr.2020.12.523.

[42] J. Stokes, Platinum in the Glass Industry, Platinum Metals Review 31(1987) 54.

[43] S. Michon, Optimisation métallurgique et mécanique de superalliages base cobalt pour usage verrier à 1200 °C, Thèse de l'Université Henri Poincaré (Nancy I), 2004.

[44] K. Chandramouli, P. Srinivasa Rao, N. Pannirselvam, T. Seshadri Sekhar, P. Sravana, STRENGTH PROPERTIES OF GLASS FIBRE CONCRETE. ARPN Journal of Engineering and Applied Sciences 5(2010).

[45] P. Srinivasa Rao, T. Seshadri Sekhar, Strength and Durability Properties of Glass Fibre Reinforced Concrete, Proceedings of the International Conference on Recent Advances in Concrete and Construction Technology. SRMIST, Chennai, India, 2005, pp. 43-50.

[46] S.P. Singh, Y. Mohammadi, S.K. Kaushik, Flexural Fatigue Analysis of Steel Fibrous Concrete Containing Mixed Fibres, ACI Materials Journal 102(2005) 438-444.

[47] S. Feih, K. Manatpon, Z. Mathys et al., Strength degradation of glass fibers at high temperatures, Journal of Materials Science 44(2009) 392–400. https://doi.org/10.1007/s10853-008-3140-x.

[48] SAINT-GOBAIN et la laine de verre: Histoire d'une réussite internationale, retrieved from https://studylib.net/doc/25301277/saint-gobain-et-la-laine-de-verre-recardre.

[49] A.T. Steegmann Jr., Human cold adaptation: An unfinished agenda, American Journal of Human Biology 19(2007) 218-227. https://doi.org/10.1002/ajhb.20614.

[50] D. Bozsaky, The historical development of thermal insulation materials, Periodica Polytechnica Architecture 41(2010) 49–56. https://doi.org/10.3311/pp.ar.2010-2.02.

[51] J.C. McMullen, REFRACTORY GLASS WOOL, United States Patent Office, 2,557,834, 1949.

[52] A. Berge, P.Ä.R. Johansson, Literature review of high performance thermal insulation, 2012.

[53] A.M. Papadopoulos, State of the art in thermal insulation materials and aims for future developments, Energy and Buildings 37(2005) 77-86.

[54] M. Chouteau, J. Forest, C. Nguyen. Histoire de la genèse du procédé de fibrage du verre TEL. Technologie et Innovation, Biographies d'innovation 5(2020). DOI: 10.21494/ISTE.OP.2020.0481.

[55] Royer, L, Élaboration et caractérisation d'alliages base chrome pour applications à très haute température. Université Henri Poincaré, Nancy I, 2009.

[56] S. Diliberto, Elaboration et caractérisation d'alliages réfractaires pour la fusion du verre: alliages MoWCr, alliages base Ni "bi-ODS", [Doctoral dissertation, Université Henri Poincaré (Nancy I), 2000].

[57] T.M. Pollock, J. Dibbern, M. Tsunekane et al., New Co-based γ-γ' high-temperature alloys, JOM 62(2010) 58–63. https://doi.org/10.1007/s11837-010-0013-y.

[58] J.-L. Bernard, S. Michon, C. Liebaut, P. Berthod, Alliage refractaire et procede de fabrication de laine minerale. Patent WO2005052208A, 2004.

[59] N.B. Pilling, R.E. Bedworth,. Oxidation of metals at high temperatures, Journal of the Institute of Metals (1923)529.

[60] A.M. Huntz, Stresses in NiO, Cr2O3 and Al2O3 oxide scales, Materials Science and Engineering A 201(1995) 211-228.

[61] H. Buscail, Y.P. Jacob, M.F. Stroosnijder, E. Caudron, R. Cueff, F. Rabaste, S. Perrier, X-ray diffraction to study the oxidation mechanism of chromium at elevated temperatures, Materials Science Forum, Les Embiez, 2004.

[62] Y.W. Kim, G.R. Belton, The Thermodynamics of Volatilization of Chromic Oxide: Part I. The Species CrO_3 and CrO_2OH, Metallurgical Transactions 5 (1974) 1811-1816.

[63] R. Durham, B. Gleeson, D.J. Young, Silicon contamination effects in the oxidation of carbide-containing cobalt-chromium alloys, Materials and Corrosion - Werkstoffe und Korrosion 49(1998) 855-863.

[64] B. Li, B. Gleeson, Effects of silicon on the oxidation behavior of Ni-base chromiaforming alloys, Oxidation of Metals 65(2006) 101-122.

[65] D. Monceau, M. Vilasi, High Temperature Oxidation of Additively Manufactured Structural Alloys, JOM Journal of the Minerals, Metals and Materials Society 74(2022) 1659-1667. https://doi.org/10.1007/s11837-022-05198-z.

[66] G. Kaptay, Nano-Calphad: extension of the Calphad method to systems with nano-phases and complexions, Journal of Materials Science 47 (2012) 8320–8335. https://doi.org/10.1007/s10853-012-6772-9.

[67] N. Saunders, A.P. Miodownik, CALPHAD—A Comprehensive Guide, Oxford, Pergamon Press, 1998.

[68] L. Kaufman, J. Agren, CALPHAD, first and second generation—Birth of the materials genome, Scripta Materialia 70 (2014) 3.

[69] S. Gorsse, O.N. Senkov, About the Reliability of CALPHAD Predictions in Multicomponent Systems, Entropy 20(2018) 899. https://doi.org/10.3390/e20120899.

[70] S. Gorsse, F. Tancret, Current and Emerging Practices of CALPHAD toward the Development of High Entropy Alloys and Complex Concentrated Alloys, Journal of Materials Research 33(2018) 2899–2923. https://doi.org/10.1557/jmr.2018.152.

[71] G.L.W. Hart, T. Mueller, C. Toher et al., Machine learning for alloys, Nature Reviews Materials 6(2021) 730–755. https://doi.org/10.1038/s41578-021-00340-w.

[72] X. Liu, P. Xu, J. Zhao, W. Lu, M. Li, G. Wang, Material machine learning for alloys: Applications, challenges and perspectives, Journal of Alloys and Compounds 921 (2022) 165984. https://doi.org/10.1016/j.jallcom.2022.165984.

[73] C. Yang, C. Ren, Y. Jia, G. Wang, M. Li, W. Lu, A machine learning-based alloy design system to facilitate the rational design of high entropy alloys with enhanced hardness, Acta Materialia 222 (2022) 117431. https://doi.org/10.1016/j.actamat.2021.117431.

[74] K.R. Peters, D.P. Whittle, J. Stringer, Oxidation and hot corrosion of nickel-based alloys containing molybdenum, Corrosion Science 16(1976) 791-804. https://doi.org/10.1016/0010-938X(76)90010-X.

[75] D.B. Lee, G. Simkovich, Oxidation behavior of molybdenum and chromium alloys, Journal of the Less-Common Metals 147(1989).

[76] D.B. Lee, G. Simkovich, Oxidation of molybdenum-tungsten-chromium-silicon alloys, Oxidation of Metals 31(1989) 265-274.

[77] V.B. Voitovich, V.A. Lavrenko, V.M. Adejev et al., High-temperature oxidation of tantalum of different purity, Oxidation of Metals 43 (1995) 509–526. https://doi.org/10.1007/BF01046896.

[78] P. Aimone, K. Moser, Working with Tantalum and Tantalum Alloys, Proceedings of CORROSION 2003, San Diego, California, 2003.

[79] R. Podor, C. Rapin, N. David, S. Mathieu, Kinetics and mechanisms of Tantalum corrosion in glass melts, Journal of the Electrochemical Society 151(2004).

[80] R. Liu, X.J. Wu, S. Kapoor et al., Effects of Temperature on the Hardness and Wear Resistance of High-Tungsten Stellite Alloys, Metallurgical and Materials Transactions A 46 (2015) 587–599. https://doi.org/10.1007/s11661-014-2664-8.

[81] A. Calvo, C. García-Rosales, F. Koch, N. Ordás, I. Iturriza, H. Greuner, G. Pintsuk, C. Sarbu, Manufacturing and testing of self-passivating tungsten alloys of different composition, Nuclear Materials and Energy 9 (2016) 422-429. https://doi.org/10.1016/j.nme.2016.06.002.

[82] J. Dai, J. Zhu, C. Chen, F. Weng, High temperature oxidation behavior and research status of modifications on improving high temperature oxidation resistance of titanium alloys and titanium aluminides: A review, Journal of Alloys and Compounds 685 (2016) 784-798. https://doi.org/10.1016/j.jallcom.2016.06.212.

[83] C. Rapin, R. Podor, S. Michon, P. Berthod, S. Mathieu, Titanium corrosion in molten glasses Part 2. Electrochemical study and corrosion mechanisms, Glass Science and Technology 77(2004) 88-94.

[84] L.E. Moreau, S. Gorsse, G. Lambard, Microstructure and oxidation behavior of Co-Cr-Ta alloys, Journal of alloys and compounds 936 (2023) 167968. https://doi.org/10.1016//j.jallcom.2022.167968.

[85] H.M. Tawancy, V.R. Ishwar, B.E. Lewis, On the fcc/hcp transformation in a cobaltbase superalloy (Haynes alloy No. 25), Journal of Materials Science Letters 5(1986) 337–341.

[86] K.C. Lo, H. Murakami, J.W. Yeh, A.C. Yeh, Oxidation behaviour of a novel refractory high entropy alloy at elevated temperatures, Intermetallics 119(2020) 106711. https://doi.org/10.1016/j.intermet.2020.106711.

[87] B. Gorr, F. Müller, S. Schellert, H.-J. Christ, S. Chen, A. Kauffmann, M. Heilmaier, A new strategy to intrinsically protect refractory metal-based alloys at ultra-high temperatures, Corrosion Science 166 (2020) 108475. https://doi.org/10.1016/j.corsci.2020.108475.

[88] B. Gorr, F. Müller, M. Azim et al., High-temperature oxidation behavior of refractory high-entropy alloys: effect of alloy composition, Oxidation of Metals 88 (2017) 339-349. https://doi.org/10.1007/s11085-016-9696-y.

[89] L. Breiman, Random forests, Machine Learning 45(2001) 5-32. https ;//doi.org/10.1023/A :1010933404324.

[90] B. Efron, The Jackknife, the Bootstrap and Other Resampling Plans, CBMS-NSF Regional Conference Series in Applied Mathematics, Monograph, SIAM, 1982, p.38. Philadelphia. https://doi.org/10.1137/1.9781611970319.

[91] D.R. Jones, M. Schonlau, W.J. Welch, Efficient global optimization of expensive black-box functions, Journal of Global Optimization 13(1998), 455–492.

[92] F. Pedregosa, G. Varoquaux, A. Gramfort, V. Michel, B. Thirion et al., Scikit-learn: Machine Learning in Python, Journal of Machine Learning Research 12(2011) 2825-2830.

[93] SheffieldML/GPyOpt (n.d.), Gaussian Process Optimization using GPy, retrieved from https://github.com/SheffieldML/GPyOpt.

[94] S. Schellert, B. Gorr, H.J. Christ et al., The Effect of Al on the Formation of a $CrTaO_4$ Layer in Refractory High Entropy Alloys Ta-Mo-Cr-Ti-xAl, Oxidation of Metals 96 (2021) 333–345. https://doi.org/10.1007/s11085-021-10046-7.

[95] L.E. Moreau, B. Banoth, A. Ishida, H. Murakami, Effect of Re addition on microstructure and oxidation resistance of Co-Cr-Ta-Ti-C alloys, in Coatings 14 (2024) 26; https://doi.org/10.3390/coatings14010026

[96] P. Berthod, Z. Himeur, P.J. Panteix, Influences of the Co content and of the level of high temperature on the microstructure and oxidation of cast {Ni, Co}-based Cr-rich TaC-containing cast alloys, Journal of Alloys and Compounds 739(2018) 447-456. https://doi.org/10.1016/j.jallcom.2017.12.254

[97] P. Berthod et al., REFRACTORY ALLOY, FIBRE-FORMING PLATE AND METHOD FOR PRODUCING MINERAL WOOL, US Patent No. US 8,262,964B2, 2012.

[98] L.E. Moreau, B. Banoth, A. Ishida, H. Murakami, Effect of Re addition on microstructure and oxidation resistance of Co-Cr-Ta-Ti-C alloys, in Coatings 14 (2024) 26; https://doi.org/10.3390/coatings14010026

[99] Principle of Differential Thermal Analysis (DTA), retrieved from https://www.hitachi-hightech.com/global/products/science/tech/ana/thermal/descriptions/dta.html.

[100] L. Karge, R. Gilles, D. Mukherji, P. Beran, P. Strunz, M. Hoelzel, J. Rosler, Beyond Ni-base Superalloys: Influence of Cr Addition on Co-Re base alloys strengthened by nano-sized TaC particles, Physica B: Physics of Condensed Matter 551(2018) 1–5. https://doi.org/10.1016/j.physb.2017.11.059.

[101] B. Gorr, V. Trindade, S. Burk, H.J. Christ, M. Klauke, D. Mukherji, J. Rosler, Oxidation Behaviour of Model Cobalt-Rhenium Alloys During Short-Term Exposure to Laboratory Air at Elevated Temperature, Oxidation of Metals 71(2009) 157-172. https://doi.org/10.1007/s11085-008-9133-y.

[102] C.S. Tedmon Jr., Effect of oxide volatilization on the oxidation kinetics of Cr and Fe-Cr alloys, Journal of the Electrochemical Society 113(1966) 766-768.

Acknowledgement

List of research achievements for application of Doctor of Engineering, Waseda University

Full Name : MOREAU　Louis Etienne Victor　　　　　seal or signature

_____

Date Submitted(yyyy/mm/dd):　| 2024/2/7 |

種類別 (By Type)	題名、　発表・発行掲載誌名、　　発表・発行年月、　　連名者（申請者含む） (theme, journal name, date & year of publication, name of authors inc. yourself)
Academic publication	O 1. MOREAU Louis Etienne, Gorsse Stéphane, Lambard Guillaume, Murakami Hideyuki, Microstructure and oxidation behavior of Co – Cr – Ta ternary alloys, Journal of Alloys and Compounds 936 (2023) 167968 O 2. MOREAU Louis Etienne, ISHIDA Akira, BANOTH Santosh, MURAKAMI Hideyuki Effect of Re addition on microstructure and oxidation resistance of Co-Cr-Ta-Ti-C alloys, Coatings, 14(,2024), 26. https://doi.org/10.3390/coatings14010026
Lectures	1. MOREAU Louis Etienne, GORSSE Stephane, LAMBARD Guillaume, MURAKAMI Hideyuki, Study of oxidation resistance of Co-Cr-Ta ternary alloy system for ultra-high temperature applications, Japan Institute of Metals and Materials, online, 2021/09 (Poster presentation) 2. MOREAU Louis Etienne, GORSSE Stephane, LAMBARD Guillaume, MURAKAMI Hideyuki, Study of oxidation resistance of Co-Cr-Ta ternary alloy system for ultra-high temperature applications, International Conference on Solid Compounds of Transition Elements in Bordeaux, France, 2022/06 (Poster Presentation) 3. MOREAU Louis Etienne, GORSSE Stephane, LAMBARD Guillaume, MURAKAMI Hideyuki, Study of oxidation resistance of Co-Cr-Ta ternary alloy system for ultra-high temperature applications, International Symposium on High-temperature Oxidation and Corrosion 2022 in Takamatsu, Japan, 2022/10 (Oral Presentation)
Others	Best poster presentation award Japan Institute of Metals and Materials, online in 2021/09 Best poster presentation award of International Conference on Solid Compounds of Transition Elements in Bordeaux, France, 2022/06